2018

Pressure Image Based Attitude Controller for Small Unmanned Aerial Vehicles

Kenneth Thompson
University of Central Florida

PRESSURE IMAGE BASED ATTITUDE CONTROLLER FOR SMALL UNMANNED AERIAL VEHICLES

by

KENNETH THOMPSON
B.S. Arkansas State University, 2012
M.S. University of Central Florida, 2015

A dissertation submitted in partial fulfillment of the requirements
for the degree of Doctor of Philosophy
in the Department of Mechanical and Aerospace Engineering
in the College of Engineering and Computer Sciences
at the University of Central Florida
Orlando, Florida

Spring Term
2018

Major Professor:
Yunjun Xu

ABSTRACT

As technology improves, small unmanned aerial vehicles (SUAV) have been identified for their utility in a variety of applications in which larger unmanned craft may be incapable of accomplishing mission objectives. These aircraft with their small size and long flight durations are ideal for hazardous inspection and long duration surveillance missions. One challenge preventing the widespread adoption of these systems is their instability to abrupt changes in the flow field around them due to wind gusts or flow separation. Currently, traditional rigid body based sensors are implemented in their flight control systems, which are sufficient in higher inertia aircraft for accurate control. However, in low inertia SUAV applications during a flow event, often, the inertial sensors are incapable of detecting the event before catastrophic failure. A method of directly measuring the flow information around the SUAV in order to generate control commands will improve the stability of these systems by allowing these systems to directly react to flow events. In contrast, established inertial based control systems can only react to changes in vehicle dynamics caused by flow events. Such a method is developed utilizing a network of pressure and shear sensors embedded in the wing and used to create flow images which can be easily manipulated to generate control commands. A method of accurately calculating the aerodynamic moment

acting on the aircraft based on the flow image is also developed for implementation of flow image-based control in real world systems.

TABLE OF CONTENTS

LIST OF FIGURES

LIST OF TABLES

INTRODUCTION

This dissertation covers the development of a pressure image based robust controller for small unmanned aerial vehicles (SUAV). The aircraft of interest in this dissertation are fixed wing aircraft which are less than 2 meters in size in any dimension and have a maximum rated altitude of less than 1200 feet [1]. These aircraft currently experience significant instabilities due to their low inertia. These instabilities have prevented widespread adoption of these vehicles in a wide variety of applications as currently quadrotor technology is more stable in short duration low altitude applications. However, if the stability of the SUAV could be increased it is expected that their adoption for long distance or duration missions would greatly increase as it is not currently feasible to utilize other small aircraft systems for these types of missions [1].

The pressure image based control utilizes real-time pressure or shear measurements on the wing surface to estimate the current aerodynamic forces experienced by the aircraft. The pressure image based control uses the pressure or shear measurements on the surface of the wings to directly generate control commands for the attitude of the SUAV. It is expected that the ability to directly measure disturbances affecting the aerodynamic forces of the aircraft will provide an opportunity to increase the stability of SUAV flight with control algorithms when compared to traditional rigid body sensor based control algorithms. This dissertation

discusses the tools and methods necessary for the development of a pressure image based attitude controller which is robust to gust disturbances while having similar performance to rigid body sensor based controllers.

In **Chapter 1**, the motivation and contributions are outlined for the work summarized in this dissertation. A literature review is also presented which establishes the importance of this work as well as discussing previous foundational work. In **Chapter 2**, a new method is introduced to increase the accuracy of aerodynamic moment estimation techniques in sparse distributed sensor arrays. In **Chapter 3**, the development of two pitch controllers is discussed. The first, is a flow field based pitch controller in which the pressure over the surface is assumed to be uniform in the span-wise direction. The second controller is a pressure image based controller in which the pressure measurements over the entire wing surface are used to generate control commands. In **Chapter 4**, the three axis pressure image based controller is developed with its stability proven and performance is validated through simulation. In **Chapter 5**, conclusions and discussions of the overall work is presented with some possible ways to expand the research for future work.

CHAPTER 1

BACKGROUND

1.1 Motivation

1.1.1 Aerodynamic Moment Mapping Function

The aerodynamic mapping function proposed by Shen [2] is a method to estimate the aerodynamic moment during SUAV flight using pressure and shear measurements. This method has many benefits including that the mapping function is easy to implement in real systems as it is dependent only on the geometry of the SUAV. It follows, that the mapping function is an invariant method for estimating the aerodynamic moment. However, the mapping function does have several sources of potential error.

1. Each sensor reading is required for accurate moment calculation, thus a sensor that is malfunctioning will propagate the error into the mapping function calculation.

2. Accuracy of the method depends on sensor density, thus error can be large since only a finite number of sensors can be installed on an aircraft due to power, weight, and geometry limitations.

3. Currently there are no sensors which can simultaneously measure pressure and shear information which could greatly increase the accuracy of the estimate of the aerodynamic moment.

4. Certain sensors influence the aerodynamic moment more than others, that is, near the leading edge, higher forces are experienced resulting in more contribution to the overall moment.

5. One of the terms used to calculate the moment estimate can be difficult to calculate and leads to significant errors in the moment estimate. This term is the area over which each sensor acts which is difficult to measure. This source of error is particularly prevalent for sparse sensor configurations.

1.1.2 Flight Parameter Estimation

Many people who have been able to estimate flight parameters with embedded surface sensors. Angle of attack of the flow around a cylinder has been estimated using artificial hair sensors [3]. Angle of attack, sideslip and free stream velocity on a wing have been estimated using heat film pressure sensors embedded in a flat plate [4]. The development of a system which is capable of estimating the flight parameters of angle of attack, sideslip angle and freestream velocity is essential for development of contained autopilot systems using flow measurements. However, the development of methods to estimate stability derivatives based

on aerodynamic moment estimates has not been shown in the literature, which would be a very useful tool in the development of real time SUAV control systems. All control systems for SUAVs require knowledge of the aircraft dynamic model, the above stability derivatives are seen in most traditional flight controllers. The flight state estimates (angle of attack, sideslip angle and freestream velocity) can be useful in controller designs, thus an integrated system for estimating these parameters based on the flow sensor measurements would be useful.

1.1.3 SUAV Pressure Based Flight control

In SUAVs, embedded pressure sensor arrays have been utilized to develop a pitching controller [5] as well as a fault tolerant attitude controller [6]. These controller designs have shown the benefit of utilizing real time pressure measurements to generate control commands in environments where SUAVs experience unsteady aerodynamic forces due to gusts or flow separation. The SUAV control benefits by reacting directly to the stimulus causing a change in attitude of the SUAV (gusts or flow separation) compared to the traditional rigid body sensor based controllers which are only capable of measuring the induced acceleration caused by the disturbance. The above controllers are limited in application, as they are dependent on sparse sensor networks. It is expected that if a denser sensor network could be utilized, the aerodynamic moment estimate accuracy would increase resulting in higher performance and robustness.

1.2 Contributions

1.2.1 Aerodynamic Moment Mapping Function

A method of calibrating the the aerodynamic mapping function has been developed using online pressure measurements to reduce the errors associated with sparse measurements. In this work a sparse array is defined as having 20 or fewer embedded flow sensors. This calibration method utilizes a modified version of established recursive least squares parameter estimation methods to determine a sensor error bias for each sensor measurement to reduce the error experienced by the overall aerodynamic moment estimate error. The least squares method has been modified to prevent the sensor error bias calculated for an individual sensor from overpowering the other measurement values, this ensures that the error correction is distributed between all of the sensor measurements.

The calibration method can reduce the influence of malfunctioning sensors in real time, minimizing the effect that they have on the overall mapping function moment errors. The error induced by having a sparse sensing network can also be reduced through calibration by allowing the bias term calculated to compensate for integration errors introduced by a sparse sensor layout as well as errors introduced by an incorrect estimate of the sensor area.

1.2.2 Flight Parameter Estimation

A method of estimating flight parameters based only on the surface pressure or shear measurements is developed and is capable of estimating aerodynamic moment, angle of attack, sideslip angle and free stream velocity. These estimates are used in the development of a pressure image based attitude controller.

1.2.3 SUAV Pressure Based Flight Control

The first objective for the development of a pressure image based flight controller is to establish qualitative relationships between the changes in flight parameters using pressure profiles over the wing. These relationships allow the controller to know how the pressure profile changes for a given change in angle of attack, sideslip angle or velocity. These changes need to be consistent over a flight envelope for the development of a robust proportional-derivative (PD) controller based on the SUAV wing pressure profile. The second objective for the pressure image based flight controller is to develop image operators which will be used to convert a pressure image over the wing into usable information for the pressure image based controller. These developed operators allow the pressure image to easily be implemented in the controller and used for generating control commands based solely on the direct pressure measurements.

1.3 Literature Review

In recent years, small unmanned aerial vehicles have drawn significant attention from academia, research laboratories, industry, regulation offices, and the general public. The properties of these vehicles have been classified by the United States department of defense as being Group 1 [7] with properties summarized in **Table 1.1**.

Table 1.1: Properties of SUAVs

Max Gross Takeoff Weight	$\leq$ 20 pounds
Operating Altitude	$\leq$ 1200 ft above ground level
Airspeed	$\leq$ 100 knots
Size	One dimension $>$ 1.5 ft none larger than 6.5 ft
Launch	Hand launch, catapult or runway

With many salient features such as small size, ultralight weight, and relatively low cost, the emerging of this type of vehicle has been seen in transportation [8, 9], agriculture [10], wildlife monitoring [11], defense [12–15], and commercial [8, 16] applications. These various applications demonstrate the utility of these aircraft for various altitude, payload and mission objectives. In most of these applications the SUAV is operating at altitudes below 1000 feet with a rough chord Reynolds number below 500,000 [17]. In this flight regime, the aircraft is sensitive to wind and atmospheric turbulence, potentially to the point of instability.

Zibikowski introduces the concept of sensor rich feedback control, [18]. In sensor rich control the flight controller utilizes measurements from many distributed sensors to generate computationally easy control commands. Traditional control systems use the opposite ideology, where few measurements are taken and the complex flight dynamics are controlled via complex computations by the flight controller. In SUAV applications, computation resources are at a premium thus, any method to simplify the computation of control commands is beneficial to their implementation in autonomous flight control applications. To this end, SUAV flight control systems have been studied recently in [19–22] which integrate distributed air flow feedback from an array of flow sensors. The conceptual relationship between stagnation points, unsteady loads or moments, and pressure distribution over the wing is discussed in [19]. Specifically, real time pressure or wall shear stress fields are used to calculate aerodynamic forces and moments to determine appropriate control surface deflections [23]. In [21], freestream static pressure, stagnation pressure, angle of attack, and sideslip angle are calculated via a pressure tap array mounted on the SUAV's leading edge using neural networks.

Robust controllers have been developed for pressure-sensor empowered flight control systems of SUAV and tested in simulation and wind tunnel experiments [2, 5, 6]. Therein, an aerodynamic moment model is established which exploits local streamwise pressure and shear information along the wing surface to calculate the aerodynamic moment [6]. Although successful, the accuracy of this method depends greatly upon the number of sensors used. Along with new flight control strategies, progress has been continuously made in terms of

developing new bioinspired microscale flow sensors, such as artificial hair sensors [24] [25] or surface pressure sensors [26], with reduced size and increased accuracy.

Most flight control designs in existing SUAVs rely on rigid body sensor measurements. The sensors used include inertial measurement unit (IMU) [27, 28] and global positioning system (GPS) [12, 29] to measure translational and rotational states or cameras [28, 30–34] to detect information from their surrounding environment (e.g. buildings and trees). The performance of such controllers strongly depends on the accuracy of the aerodynamic coefficients, stability derivatives, and control derivatives obtained offline. Furthermore, rigid body sensor driven controllers are not effective in responding to sudden changes in surface flow fields such as turbulence and flow separation, since actual airflow information over SUAV surfaces is not promptly captured by the controller.

SUAVs, birds and bats are fly in similar Reynolds number regimes. It is experimentally validated in [35–39] that birds and bats can use sensed airflow information such as flow separation and flow reattachment to achieve graceful flights. One fundamental difference in sensing and control mechanisms between man-made SUAVs and naturally evolved creatures is: airflow information, such as pressure and boundary layer characteristics, is felt by birds via distributed airflow sensors, whereas rigid body sensors dominate flight control systems in SUAVs. To close this gap, microscale flow sensors and associated control designs using flow sensor information have been studied simultaneously. There has been much research conducted in manufacturing flow sensors for SUAVs such as wall-shear stress [40], embedded skin sensors [41–43]. In the meantime, pressure sensors have been integrated into SUAV

designs to achieve pitching control [44, 45] or three-axis attitude control [6] , to sense flow separation [3, 46, 47] or stagnation points [3, 46], or to enhance calibrations of aerodynamic coefficients [48, 49].

CHAPTER 2

CALIBRATION OF AERODYNAMIC MAPPING FUNCTION

This chapter summarizes work published in [48] and discusses the calibration of an aerodynamic moment model based on sparse flow measurements, where it is assumed that the moment is encoded in the flow patterns received by the sensor array. Though this chapter focuses on calibrating a group of sensors to accurately estimate the aerodynamic moment experienced by the aircraft, this methodology could be applied directly to individual measurements to calibrate their contribution to aircraft control maneuvers. The rationales of the study are fourfold. First, microscale flow sensors, such as pressure or flow velocity sensitive devices, have inherent uncertainty in their readings and are subject to malfunction, degradation, or failure during flight. Second, sensors in different locations on the SUAV surface may have different bias and noise characteristics at different flight conditions. Third, the number of sensors onboard is finite and not all the flow information on the SUAV surface can be measured and utilized. Finally, no commercially available sensor can simultaneously measure both pressure and shear stress information on wing surfaces. As a result, the direct integration of point-wise flow measurement data over a wing skin surface can lead to large errors in quantifying aerodynamic force and moment. Thus, a calibration process is warranted for better estimation of the aerodynamic moment.

In this study, we propose a constrained recursive least squares (LS) estimator (CRLSE) to calibrate an aerodynamic moment model. To compensate for moment model errors, a bias is identified for each flow sensor and constrained to prevent values from exceeding physical limits of the SUAV. Although LS estimators have been previously considered [50] [51], the CRLSE is intended to be more intuitive. Also, as compared with the widely used recursive LS method [52], a constraint is added into the performance index to increase the accuracy of the calculated bias for the SUAV.

2.1 Overview of Aerodynamic Mapping Function

Inspired by natural flyers [18], SUAV flight control systems using flow information fed back from distributed flow sensor arrays have been recently studied [6, 20, 53–55]. A basic idea for distributed flow sensor feedback is to sense real time pressure or wall shear stress fields so that aerodynamic forces and moments are determined and used to generate control surface deflection commands.

The SUAV platform for the simulation is similar to that reported by Shen, Xu, and Dickinson [6], and contains a total of 40 flow sensors, 20 each on the top and bottom surfaces along the mean aerodynamic chord (MAC) at 1%, 4%, 10%, 25%, 50%, 70%, 74%, 76%, 85% and 98% of the chord length. The sensor layout can be seen below in **Figure 2.1a**. For this simulated platform, the root chord length c_r is 10cm, the tip chord length c_t is 5cm, the elevator width at the mean aerodynamic chord c_e is 2cm, the wingspan b is 15cm, the

elevator width b_e is 7.5cm, the dihedral height at the tip d is 1cm, the width of the rudder w is 3cm, and the height of the rudder h is 3cm.

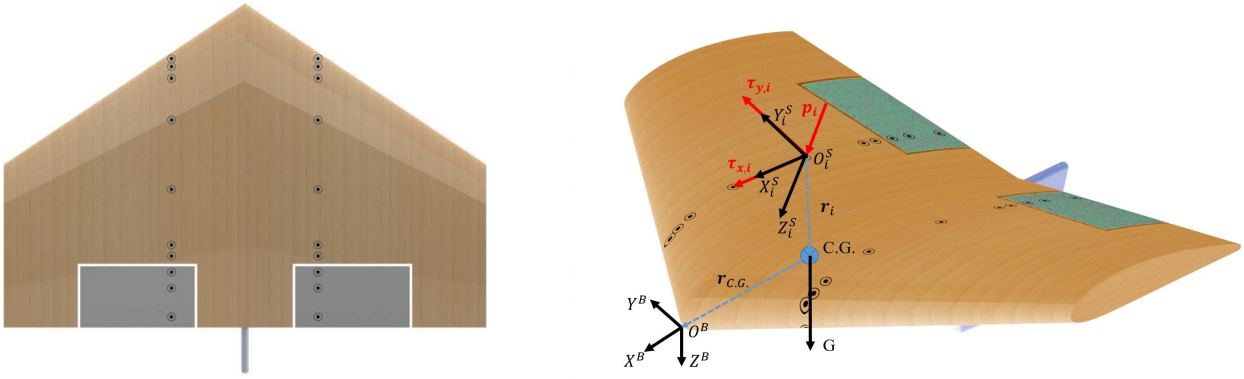

(a) Sensor locations for simulation

(b) Coordinates for the mapping function

Figure 2.1: Wing configuration for simulation [48]

This geometry information was programmed into the Athena Vortex Lattice (AVL) code, AVL 3.35 [56], for use in subsequent simulations. It should be noted that the results from AVL are used to approximate the flow information obtained during flight and the wing may experience significantly different flow profiles during actual flight. However, the goal of the simulation is to validate the effectiveness of the calibration procedure which the data from AVL accomplishes. AVL requires the following inputs: angle of attack α, air speed v, side slip angle β, left elevon deflection $\delta_{a,L}$, right elevon deflection $\delta_{a,R}$, and rudder deflection δ_r. AVL outputs the total aerodynamic moment $\boldsymbol{m}_{AVL}$ which is composed of the roll, pitch and yaw moments, L_{AVL}, M_{AVL} and N_{AVL}, respectively, and pressure information p_i of sensor i.

Since AVL applies an inviscid approximation, shear force at the sensor i location, $\tau_{x,i}$ and $\tau_{y,i}$, is assumed to be Newtonian, and calculated using the local Reynolds number based on pressure, which can be found in [2] [57].

As shown in **Figure 2.1b**, there are two coordinate systems required to calculate the aerodynamic moment contributed by flow information at sensor location i: the body coordinate O^B, X^B, Y^B, Z^B, and the local surface coordinate O_i^S, X_i^S, Y_i^S, Z_i^S. The origin of the body coordinate, $\boldsymbol{O}^B$ is located at the nose of the SUAV, with X^B pointed forward along the root chord, Y^B is pointed to the right and Z^B is pointed downward according to the right hand rule. The surface element coordinate origin $\boldsymbol{O}_i^S$ is located at the center of the i^{th} sensor's surface coverage area with X_i^S and Y_i^S tangential to the wing surface and Z_i^S normal to the surface. The coordinate system X_i^S, Y_i^S, Z_i^S is aligned with the principle stresses, shear $\tau_{x,i}, \tau_{y,i}$ and pressure p_i, that comprise $\boldsymbol{q}_i = [\tau_{x,i}, \tau_{y,i}, p_i]^T$, respectively. For the mapping function, described in **Section 2.2**, the position vectors $\boldsymbol{r}_i$ and $\boldsymbol{r}_{C.G.}$ are defined as the position of sensor i and the center of gravity from the body coordinate origin, respectively.

2.2 Problem Definition

The aerodynamic moment, $\boldsymbol{m}$, can be approximated from N_s embedded flow sensor pointwise measurements using the mapping function developed in [6],

$$\boldsymbol{m} = \sum_{i=1}^{N_s} s_i[\boldsymbol{r}_i \times (R_i \boldsymbol{q}_i)] \tag{2.2.1}$$

where s_i represents the effective area covered by the i^{th} sensor, $\boldsymbol{r}_i$ is the position vector from the sensor location to the origin of the SUAV body coordinate, $\boldsymbol{q}_i = [\tau_{x,i}, \tau_{y,i}, p_i]^T$ is the shear $(\tau_{x,i}, \tau_{y,i})$ and pressure (p_i) measurements of sensor i, and R_i is the rotation matrix from the local surface element coordinate frame to the body coordinate frame. This equation is further simplified as

$$\boldsymbol{m} = M\,\boldsymbol{q} \tag{2.2.2}$$

where $\boldsymbol{q} = \{\boldsymbol{q}_i\}_{i=1}^{N_s}$ is the aggregated set of instantaneous pressure and shear stress measurements, and M is the aggregated mapping function comprised of the sum expressed in **Eq. (2.2.1)** evaluated for the number of sensors on the SUAV. The resulting aggregated mapping function matrix, M, is a $3 \times 3N_s$ matrix and the aggregated shear and pressure measurement vector,$\boldsymbol{q}$, is a $3N_s \times 1$ vector. There are several sources of potential uncertainty in the aerodynamic moment calculated using **Eq. (2.2.2)**:

1. Each sensor reading may be inaccurate and some of the sensors onboard may be malfunctioning.

2. Only a finite number of sensors can be installed on an aircraft due to the power, weight, and geometry limitations.

3. Since sensors that can simultaneously measure pressure and shear stress on aircraft surfaces are not commercially available, the moment component due to shear is neglected because its contribution is small relative to the pressure component. The omission of the shear components can easily be compensated for by the calibration method.

4. The contribution to the total aerodynamic moment may be different for the sensors at different locations thus, a single correction factor applied to the entire mapping function would be difficult to implement and may increase error in certain flight conditions.

An adaptive or robust flight controller can be developed to function despite these uncertainties [2,6]; however, an alternative is to construct a more accurate relationship between measurement data and moment calculation using **Eq. (2.2.2)**. To this end, considering the above uncertainties represented at the flow sensor level can be represented as an additive term, $\boldsymbol{\delta_q}$, further referred to as a bias, that when calibrated produces more accurate moment estimates via the mapping function **Eq. (2.2.2)**. Therefore, **Eq. (2.2.2)** can be rewritten as

$$\boldsymbol{m}_c = M\left(\boldsymbol{q} + \boldsymbol{\delta_q}\right) \tag{2.2.3}$$

in which $\boldsymbol{m}_c$ is the calibrated aerodynamic moment and $\boldsymbol{\delta_q}$ is the vector of bias values, $\boldsymbol{\delta_q} = \delta_{q,i}$ for $i = 1, ...N_s$. The bias vector $\boldsymbol{\delta_q}$ is calculated using trimmed states of the aircraft, where $\boldsymbol{m} = 0$.

2.3 Constrained Recursive Least Squares Estimation

The recursive least squares estimator (RLSE) from [52] is briefly summarized in this section to prepare for the development of CRLSE. The measurement model is described by

$$\boldsymbol{y}_k = M\boldsymbol{x}_k + \boldsymbol{v} \tag{2.3.1}$$

where $\boldsymbol{y}_k$ is the aerodynamic moment at time instant t_k, $\boldsymbol{x}_k$ is the flow sensor output, M is the mapping function , and $\boldsymbol{v} = M\boldsymbol{\delta_q}$ is the noise associated with the measured values which is assumed to be a zero mean Gaussian. The estimate $\hat{\boldsymbol{x}}$ is updated recursively using

$$\hat{\boldsymbol{x}}_k = \hat{\boldsymbol{x}}_{k-1} + K_k(\boldsymbol{y} - M\hat{\boldsymbol{x}}_{k-1}) \tag{2.3.2}$$

The gain K_k is obtained by minimizing the following performance index J_{k1}

$$J_{k1} = E[\boldsymbol{\epsilon}_k^T \boldsymbol{\epsilon}_k] = Tr(P_k) \tag{2.3.3}$$

in which $\boldsymbol{\epsilon}_k = \boldsymbol{x} - \hat{\boldsymbol{x}}_k$ is the error between the true and estimated pressure readings in step k. E is the expected value and Tr is the trace value of the covariance matrix P_k which is updated by

$$P_k = (I - K_k M)P_{k-1}(I - K_k M)^T + K_k R K_k^T \tag{2.3.4}$$

Here, R is the covariance of $\boldsymbol{v}$, and I is the identity matrix with a proper dimension. The partial derivative of the performance index is

$$\frac{\partial J_{k1}}{\partial K_k} = 2(I - K_k M)P_{k-1}(-M^T) + 2K_k R \tag{2.3.5}$$

The optimal gain is found by setting **Eq. (2.3.5)** zero and solving for K_k, which leads to

$$K_k = P_{k-1}M^T(MP_{k-1}M^T + R)^{-1} \tag{2.3.6}$$

The RLSE is used to compute sensor bias, $\boldsymbol{\delta_q}$, such that the aerodynamic moment calculated via the mapping function best matches the true value. Additionally, it is preferred that the magnitude of the bias values for sensors at different locations is not large. To this end, an

additional term J_{k2} will be added in the performance index J_{k1} to minimize the magnitude of individual terms in $\boldsymbol{\delta_q}$. The new performance index J_k can be established, where

$$J_{k2} = W(\hat{\boldsymbol{x}}_k - \boldsymbol{q})^T(\hat{\boldsymbol{x}}_k - \boldsymbol{q}) \tag{2.3.7}$$

and $\hat{\boldsymbol{x}}_k$ is the optimal estimate of pressure at step k. Since

$$\begin{aligned} \hat{\boldsymbol{x}}_k - \boldsymbol{q} &= \hat{\boldsymbol{x}}_{k-1} + K_k(\boldsymbol{y} - M\hat{\boldsymbol{x}}_{k-1}) - \boldsymbol{q} \\ &= \hat{\boldsymbol{x}}_{k-1} - \boldsymbol{q} + K_k(\boldsymbol{y} - M\hat{\boldsymbol{x}}_{k-1}) \end{aligned} \tag{2.3.8}$$

Let us define $\boldsymbol{c}_k$ as $\hat{\boldsymbol{x}}_{k-1} - \boldsymbol{q}$ and $\boldsymbol{d}_k$ as $\boldsymbol{y}_k - M\hat{\boldsymbol{x}}_{k-1}$. Then, J_{k2} can be represented as

$$\begin{aligned} J_{k2} &= W(\boldsymbol{c}_k + K_k\boldsymbol{d}_k)^T(\boldsymbol{c}_k + K_k\boldsymbol{d}_k) \\ &= W\,c_k^T\,\boldsymbol{c}_k + W\,\boldsymbol{d}_k^T K_k^T\,\boldsymbol{c}_k + W\,\boldsymbol{c}_k^T K_k\boldsymbol{d}_k + W\,\boldsymbol{d}_k^T K_k^T K_k\boldsymbol{d}_k \end{aligned} \tag{2.3.9}$$

The partial derivatives are

$$\frac{\partial \boldsymbol{d}_k^T K_k^T \boldsymbol{c}_k}{\partial K_k} = (\boldsymbol{d}_k\boldsymbol{c}_k^T)^T = \boldsymbol{c}_k\boldsymbol{d}_k^T \tag{2.3.10}$$

$$\frac{\partial \boldsymbol{c}_k^T K_k \boldsymbol{d}_k}{\partial K_k} = \boldsymbol{c}_k\boldsymbol{d}_k^T \tag{2.3.11}$$

$$\frac{\partial \boldsymbol{d}_k^T K_k^T K_k \boldsymbol{d}_k}{\partial K_k} = 2K_k\boldsymbol{d}_k\boldsymbol{d}_k^T \tag{2.3.12}$$

For the total performance index $J_k = J_{k1} + J_{k2}$, the partial derivative with respect to K_k is

$$\begin{aligned} \frac{\partial J_k}{\partial K_k} &= \frac{\partial J_{k1}}{\partial K_k} + \frac{\partial J_{k2}}{\partial K_k} \\ &= 2(I - K_kM)P_{k-1}(-M^T) + 2K_kR + 2W\boldsymbol{c}_k\boldsymbol{d}_k^T + 2WK_k\boldsymbol{d}_k\boldsymbol{d}_k^T \end{aligned} \tag{2.3.13}$$

Thus the optimal gain is solved by making $\frac{\partial J_k}{\partial K_k} = 0$, as

$$K_k = (P_{k-1}M^T - W\boldsymbol{c}_k\boldsymbol{d}_k^T)(MP_{k-1}M^T + R + W\boldsymbol{d}_k\boldsymbol{d}_k^T) \tag{2.3.14}$$

The CRLSE method (**Eq. (2.3.2)** and **Eq. (2.3.14)**) may generate an estimate $\hat{\boldsymbol{x}}_k$ close to the sensor reading $\boldsymbol{q}$; while the calculated aerodynamic moment based on **Eq. (2.2.3)** is inaccurate. To avoid this scenario, a switch mechanism is introduced as follows. If at step k, an individual sensor's bias calculated $\delta_{\boldsymbol{q},i}$ using the CRLSE exceeds a threshold value ϵ_k, which is defined as the maximum allowable offset for the sensor, the weight W in **Eq. (2.3.14)** will be set to a constant non-zero value at step $k+1$. This value of W was determined through trial and error to determine which value gave the best response while limiting the value of $\delta_{\boldsymbol{q},i}$. Otherwise, the weight W is zero. The CRLSE algorithm with the switch mechanism is outlined in the following algorithm table, **Table 2.1**.

Table 2.1: CRLSE Algorithm with Switching Mechanism

Step 1	Initialize the pressure bias reading $\hat{\boldsymbol{x}}_0$, error covariance P_0, noise covariance R, and reference moment $\boldsymbol{y}_0$
Step 2	Apply a moving average filter to smooth experiment data. For the calibration in simulation cases, this step is skipped
Step 3	Generate the mapping function M based on geometry information of the SUAV
Step 4	Begin the loop to find the value of the pressure reading bias $\hat{\boldsymbol{x}}$
Step 5	Find the augmented pressure, $\boldsymbol{q}^* = \boldsymbol{q} + \hat{\boldsymbol{x}}_{k-1}$
Step 6	Calculate the moment estimate based on the augmented pressure $\boldsymbol{q}^*$ with, $\hat{\boldsymbol{y}}_k = M\boldsymbol{q}^*$
Step 7	Calculate $\boldsymbol{c}_k$ and $\boldsymbol{d}_k$
Step 8	For $\hat{\boldsymbol{x}}_{k-1}$, evaluate the maximum component of the bias value
Step 9	If the value is less than ϵ_k, set $W = 0$; otherwise set $W = 0.002$
Step 10	Calculate K_k using **Eq. (2.3.14)**
Step 11	Update $\hat{\boldsymbol{x}}_k$ using **Eq. (2.3.2)** and P_k using **Eq. (2.3.4)**
Step 12	Repeat Steps 5-11 until a solution is found for the sensor reading bias $\hat{\boldsymbol{x}}$. A solution is considered to be found when $tr(P_k)$ converges to a constant value, i.e. $P_{k-1} \approx P_k$.

It was found that the bias for each sensor was not consistent for varying flight conditions. To increase the accuracy of the calibration, a polynomial was used to fit the pressure bias to a function of angle of attack and sideslip angle. The objective of this process is to allow the calibrated aerodynamic model to change depending on the current flight conditions of the aircraft, which will reduce the error when calculating the aerodynamic moment.

For the simulation, it was found that the 2^{nd} order polynomial fit was similar to the higher order fits, so to reduce the number of constants that need to be stored the 2^{nd} order fit was used as follows for sensor i.

$$\delta_{q,i} = c_{0,i} + c_{1,i}\alpha + c_{2,i}\beta + c_{3,i}\alpha^2 + c_{4,i}\alpha\beta + c_{5,i}\beta^2 \tag{2.3.15}$$

where $c_{i,j}$, $j = 0, ..., 5$ are the constants identified using the surface fitting toolbox found in MATLAB for the i^{th} sensor.

For the experiment calibration, a 3^{rd} order polynomial fit was used since the lower order polynomials did not accurately represent the data, this calibration function can be seen below for the i^{th} sensor. For the experiment, sideslip angle was not able to be varied so the bias was calculated with respect to velocity and angle of attack since variance was seen between velocity during the experiment.

$$\delta_{q_i} = c_{0,i} + c_{1,i}V + c_{2,i}\alpha + c_{3,i}V^2 + c_{4,i}V\alpha + c_{5,i}\alpha^2 + c_{6,i}V^3 + c_{7,i}V^2\alpha + c_{8,i}V\alpha^2 + c_{9,i}\alpha^3 \tag{2.3.16}$$

where $c_{i,j}$, $j = 0, ..., 9$ are the constants identified using the surface fitting approach for the i^{th} sensor. During flight the equations representing the calibration surfaces seen in **Eq. (2.3.16)** will be used to estimate the bias that should be used based on current flight conditions.

The algorithm used to conduct the CRLSE based moment calibration is summarized in **Table 2.2**.

Table 2.2: Moment Model Calibration Algorithm Table

Step 1	Find the trimmed flap deflections for each V, α, and β case
Step 2	Use the CRLSE method shown in **Table 2.1** to find the bias for flow sensor readings
Step 3	Repeat Step 1 and Step 2 until all the trimmed cases have been computed
Step 4	The surface fitting method is used to find the calibrated bias profile

2.4 Simulation Validation of CRLSE Method

2.4.1 Simulation Settings

The proposed aerodynamic moment model calibration method is tested in a simulation environment developed using AVL [56]. Note that AVL is not capable of giving the pressure on the top and bottom surface independently; instead ΔC_p, the difference of the pressure coefficient between the top and bottom surfaces, is used to calculate a net pressure force. Further, as mentioned in [2], there is no efficient computational fluid dynamic software can accurately compute shear stress for a SUAV for all flight regimes. Also, the pressure information computed in AVL is not accurate for the Reynolds number regime of a SUAV and

is based on a quasi-steady flow assumption which does not accurately reflect the unsteady low Reynolds number flight regime. Nevertheless, the AVL simulation environment is only used as a proof of concept for the calibration process and in a real situation, the pressure and shear information will be obtained either through wind tunnel tests or flight tests.

2.4.2 Simulation Results

It is observed in AVL simulations that the pressure profile on the SUAV surface due to variation in V_∞ is relatively small as compared with those of α and β. Therefore, a reasonable flight envelope for the SUAV is considered to be α values ranging from -4° to 12°, β values ranging from -10° to 10° and the velocity being held constant at 15 m/s. With an increment of 2° for both α and β, this results in 99 points for CRLSE to find bias values of flow sensor readings $\delta_{q,i}$, which then will be used to construct the calibration surface.

For brevity, the CRLSE results for only five of these 99 trimmed cases of are shown in **Table 2.3**. The cases selected represent an approximate diagonal line drawn across the surface to demonstrate the accuracy for the entire flight envelope. In these trimmed cases, the aerodynamic moment should be zero. It is shown that after the calibration, the aerodynamic moments (with a subscript "C") are much closer to zero as compared with the un-calibrated raw aerodynamic moments (with a subscript "R").

Table 2.3: Calibrated Aerodynamic Moments for Five Trimmed Cases Using CRLSE

β (°)	α (°)	L_R (Nm)	M_R (Nm)	N_R (Nm)	L_C (Nm)	M_C (Nm)	N_C (Nm)
-10	-4	-1.64	1.87	0.22	-0.14	0.15	0.02
-6	0	-0.32	1.62	0.23	-0.01	0.02	0.00
0	4	0.00	1.44	0.00	0.00	0.01	0.00
4	8	-0.67	1.37	-0.27	-0.01	0.02	0.00
10	12	-2.70	1.43	-0.81	-0.75	0.39	-0.22

As discussed in the previous section, the bias of sensor i for aerodynamic moment calibration changes for different trim cases and sensor locations. Therefore, the surface fitting approach **Eq. (2.3.15)** described in **Section 2.3** is used to construct the reading bias of sensor i as a function of α and β. For N_s sensors which can measure both shear and pressure stresses, N_α α-cases, and N_β β-cases are used to compute the bias surfaces for each sensor with respect to τ_x, τ_y and p. A total of $3N_s$ surface functions are generated. For the simulated aircraft, 120 surfaces are generated to represent the bias with respect to α and β for both pressure and shear measurements. The surface generated for pressure sensor 20 can be seen in **Figure 2.2**. Note that the error bias values closer to the edge of the flight envelope experience larger errors due to the method of surface construction. In one trimmed condition example, the surface fitted constants for sensor 1 (denoted as $S1$) and sensor 5 (denoted as $S5$) are shown in **Table 2.4**.

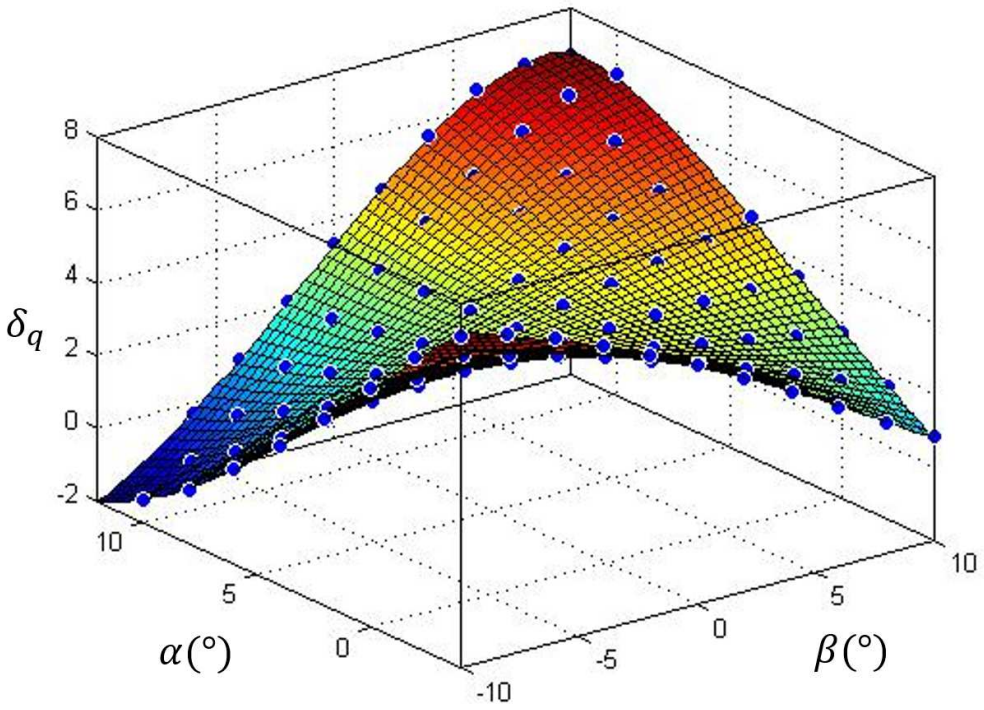

Figure 2.2: Pressure Bias Surface for Sensor 20 [48]

Ten random trim conditions are used to evaluate the calibrated results. The points selected were chosen in different quadrants of the surface to ensure that the calibration results are accurate for the entire flight envelope. The calibrated aerodynamic model (represented by the subscript "C") are compared to the uncalibrated calculated aerodynamic moment (represented by the subscript "R") as shown in **Table 2.5**.

As compared with the uncalibrated aerodynamic moments, the calibrated aerodynamic moments match very close with the true trimmed values (i.e. zeros). It can be seen that this method of calibration is capable of reducing the calculation error for the total aero-

Table 2.4: Surface Fitted Constants Used in Sensor 1 and Sensor 5

Sensor	c_0	c_1	c_2	c_3	c_4	c_5
$S1, \tau_x$	-0.141	-0.001	0.01	-8.94x10^{-5}	0.008	-8.56x10^{-4}
$S1, \tau_y$	0.008	0.012	0.005	1.07x10^{-4}	-0.004	-6.34x10^{-4}
$S1,\ p$	0.247	0.052	0.014	1.78x10^{-5}	-0.022	-0.003
$S5, \tau_x$	-0.346	-0.02	0.012	-1.56x10^{-4}	-0.006	-5.51x10^{-4}
$S5, \tau_y$	-3.51x10^{-4}	0.038	0.01	6.78x10^{-4}	-0.003	-0.001
$S5,\ p$	1.717	0.091	-0.023	-0.002	-0.042	-0.003

dynamic moments at the trim conditions. Though this method does not allow for a perfect moment match at the trim conditions, it does significantly reduce the errors seen from the uncalibrated moment calculation. The results from this simulation show that the method is viable for an actual SUAV. In the following section, wind tunnel test involving a rectangular wing with embedded pressure sensors are presented to further validate the CRLSE moment calibration.

Table 2.5: Validation of the Aerodynamic Moment Calculation

β (°)	α (°)	L_R (Nm)	M_R (Nm)	N_R (Nm)	L_C (Nm)	M_C (Nm)	N_C (Nm)
-5	-3	-0.69	1.87	0.13	-0.07	0.05	-0.01
5	1	0.13	1.57	-0.21	0.00	0.00	-0.01
3	3	-0.09	1.47	-0.15	-0.02	-0.02	-0.01
-7	5	0.59	1.39	0.39	0.08	0.02	0.03
1	7	-0.14	1.38	-0.06	-0.02	-0.01	-0.01
-9	9	1.72	1.36	0.63	0.19	0.11	0.05
-2	11	0.50	1.41	0.16	0.05	0.05	0.02
4	-1	0.33	1.71	-0.14	0.03	0.02	0.00
-3	1	-0.08	1.58	0.12	0.00	-0.01	0.00
-1	3	0.03	1.48	0.05	0.01	-0.03	0.00

2.5 Experimental Validation of CRLSE Method

2.5.1 Wing Design for Experiment

For testing the CRLSE method, a rectangular wing section was designed which would hold a total of 10 sensors as shown in **Figure 2.3a**. These sensors are located along the center

of the wing at 10%, 25%, 50%, 65% and 80% of the chord length on both top and bottom surfaces of the wings. The Bosch BMP 085 barometric pressure sensors used in the wing have a reading range of 30 kPa to 110 kPa with a resolution of 3 Pa. The wing also contains a HiTec S-50 servo motor for controlling the elevator deflection. An Arduino Uno is used to control the elevator as well as collect the pressure readings from the BMP 085 barometric pressure sensor and transmit them to MATLAB via USB. The outer surface of the wing and elevator was covered with MonoKote to produce a smooth uniform surface on the wing. A plastic tube, running through the center of mass of the wing located at 20% of the chord length, supports the wing in the wind tunnel and holds the wiring to the micro-controller. Weight was added to the leading edge of the aircraft to maintain this center of gravity location for all experiment flight conditions.

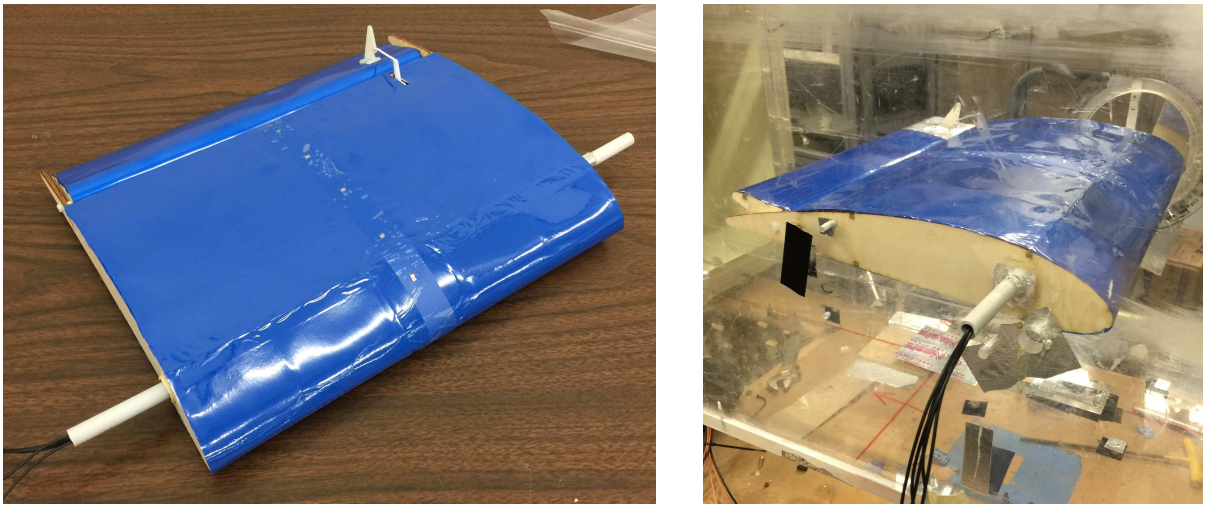

(a) Wing Constructed for Wind Tunnel Tests

(b) Wind Tunnel Experiment setup

Figure 2.3: Wind Tunnel Experiment Setup and Wing Configuration [48]

2.5.2 Wind Tunnel Specification and Experiment Setup

The wind tunnel, shown in **Figure 2.3b**, used to conduct the experiments is a low speed, suction type, non-return wind tunnel which has a test section of 30.78 x 30.78 x 60.96 cm and can provide wind speeds ranging from 10 m/s to 35 m/s. The wind tunnel has both a protractor and a wind speed measurement unit, which were used for the experiment. The protractor has a measurement accuracy of 1 degree and the wind speed measurement unit, a DATUM 2000TM, has a pressure measurement accuracy of 0.001 inch water column (inw). The pressure measurement from the DATUM 2000TM is converted to find the wind speed using the pressure-speed relation,

$$V = \sqrt{\frac{2\Delta P}{\rho_{atm}}} \tag{2.5.1}$$

where ΔP is the measurement from the DATUM 2000TM and ρ_{atm} is the density of air. To verify the CRLSE method many data points are necessary to construct the calibration surfaces for the moment model. For the wind tunnel experiments, the velocity and angle of attack will vary, though we saw little variation in pressure for varying velocity. The sideslip angle is invariant based on the current wind tunnel facility limitations. The velocity during the experiments is varied from 10 m/s to 25 m/s in increments of 5 m/s, while the angle of attack, α, is varied from -4° to 4° in increments of 2°. These parameters will result in calibration surface containing 25 points.

2.5.3 Surface Calibration Experiment Procedure

During the experiment the free stream velocity of the wind tunnel is set to be a constant for each trimmed flight condition. The sample data is collected from the test wing at a rate of 1 Hz for 100 seconds per experiment case. The pressure measurements recorded are used in the CRLSE method to estimate the calibration parameters and to create the calibration surfaces for each sensor. For the experiment, the weight for the constraint W and the constraint threshold ϵ_k are set equal to 0.002 and 25, respectively.

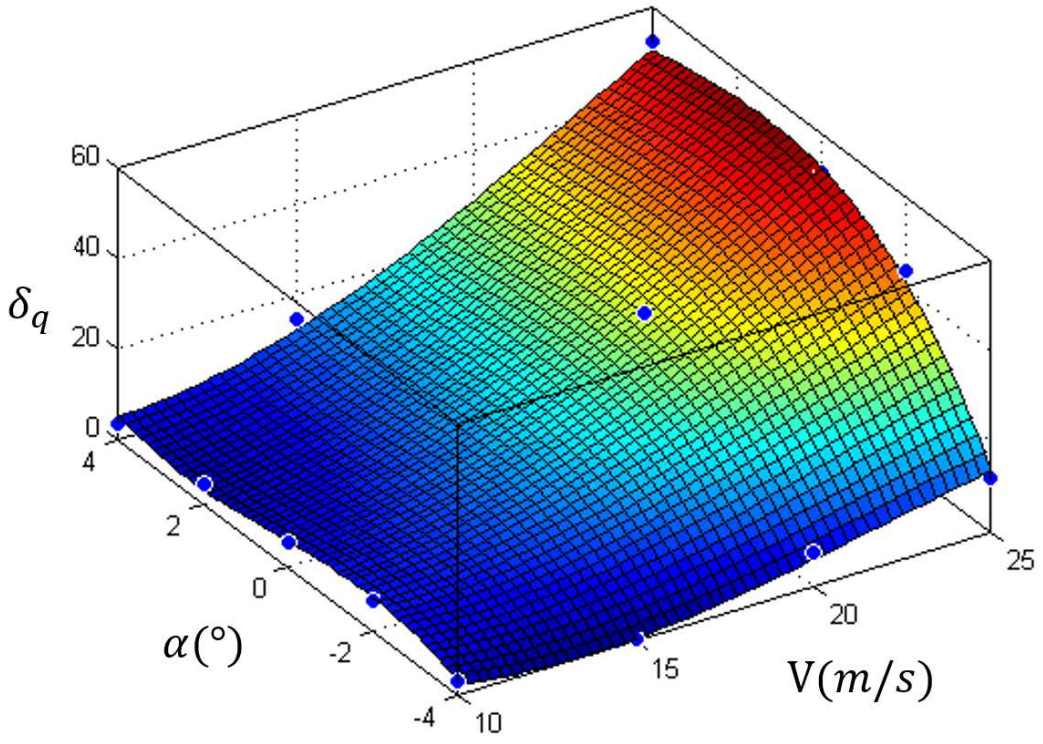

Figure 2.4: Calibration Surface for Sensor 10 Using Experiment Data [48]

The following points (V_∞, α) are removed for validation: (15 m/s, 0°), (15 m/s, 2°), (20 m/s, -2°), and (20 m/s, 2°). The calibration of pressure bias, $\boldsymbol{\delta_q}$, is constructed using the remaining 21 points to construct the calibration surface, which is fit via **Eq. (2.3.16)**. **Figure 2.4** illustrates one example calibration surface for sensor 10 located at the trailing edge of the bottom surface. The blue dots show the location of the data points used in surface construction. The constants found for the different calibration cases can be seen in **Table 2.6**. It should be noted that the constants for the upper surface and lower surface sensors at the same x-position have very similar magnitudes since they have similar contributions to the aerodynamic moment of the aircraft.

2.5.4 Model Validation Experiment Procedure and Results

The calibration constants found are then used to evaluate the accuracy of the CRLSE calibration for the aerodynamic moment calculation. With the offsets found using **Eq. (2.3.16)** the aerodynamic moment can be approximated using **Eq. (2.2.3)**.

To visualize the effectiveness of the CRLSE calibration method, the four validation cases are evaluated to determine the effectiveness of the calibration method for wind tunnel measurements. In each of these cases, the first step was to evaluate the raw (uncalibrated) pressure values using the mapping function to create a baseline for the estimated aerodynamic moment M_R. The CRLSE calibration was then used to calculate the bias vector for the

Table 2.6: Surface-Fitted Constants Used in Model Calibration

Sensor	c_0	c_1	c_2	c_3	c_4	c_5	c_6	c_7	c_8	c_9
$S1$	-2.61	0.54	0.23	-0.04	-0.01	-0.05	5.34x10^{-4}	-4.45x10^{-4}	0.01	-0.01
$S2$	1.05	-0.22	-0.09	0.02	2.6x10^{-3}	0.02	-2.14x10^{-4}	1.79x10^{-4}	-2.410^{-3}	3.8x10^{-3}
$S3$	7.01	-1.45	-0.62	0.1	0.02	0.14	-0.14x10^{-3}	1.2x10^{-3}	-0.02	0.03
$S4$	11.7	-2.41	-1.04	0.17	0.03	0.24	-2.4x10^{-3}	2.0x10^{-3}	-0.03	0.04
$S5$	32.72	-6.75	-2.91	0.47	0.08	0.66	-6.7x10^{-3}	5.6x10^{-3}	-0.08	0.12
$S6$	-2.73	0.56	0.24	-0.04	-0.01	-0.06	5.59x10^{-4}	-4.66x10^{-4}	0.01	-0.01
$S7$	1.06	-0.22	-0.09	0.02	2.6x10^{-3}	0.02	-2.17x10^{-4}	1.8x10^{-4}	-2.510^{-3}	3.8x10^{-3}
$S8$	7.01	-1.45	-0.62	0.1	0.02	0.14	-0.14x10^{-3}	1.2x10^{-3}	-0.02	0.03
$S9$	11.8	-2.43	-1.05	0.17	0.03	0.24	-2.4x10^{-3}	2.0x10^{-3}	-0.03	0.04
$S10$	33.41	-6.89	-2.97	0.48	0.08	0.68	-6.8x10^{-3}	5.7x10^{-3}	-0.08	0.12

sensors in the wind tunnel, then using the calibration vector the aerodynamic moment was estimated using the mapping function and thee calibrated pressure, this calibrated moment estimate, M_C, shows the reduction in error using the calibration method. Since the pressure measurements inherently contain noise, the mean was taken of all 100 calculated moments to easily visualize the center of the data for each aerodynamic moment estimation method. The first two cases both have a free stream wind velocity of $V_\infty = 15$ m/s and an angle of attack of $\alpha = 0^\circ$ for **Figure 2.5** and $\alpha = 2^\circ$ in **Figure 2.6**. It can be seen in **Figure 2.5** the estimated moment is reduced from 4.75 N-m to 0.87 N-m and it is worth noting that the CRLSE method does not reduce the impact of noise in the signal and merely shifts

the moment estimate by a constant closer towards the actual moment of 0 N-m. Similarly in **Figure 2.6**, the estimated moment is reduced from 4.25 N-m to -1.22 N-m which is a significant reduction in error.

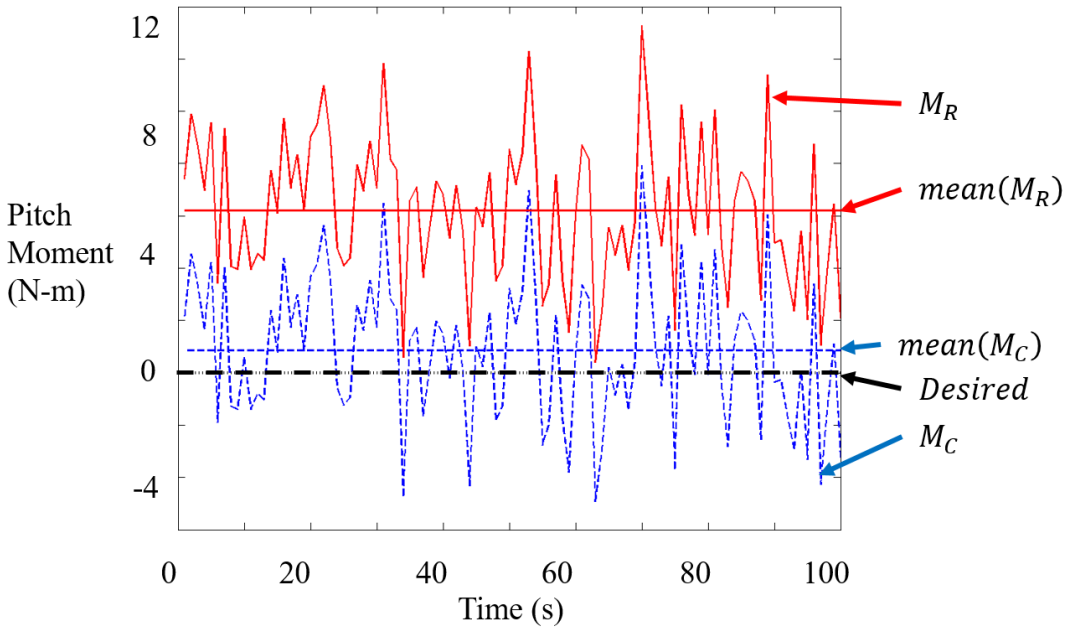

Figure 2.5: Comparison of uncalibrated and calibrated models for $V_\infty = 15$ m/s and $\alpha = 0°$ [48]

The last two cases both have a free stream wind velocity of $V_\infty = 20$ m/s and an angle of attack of $\alpha = -2°$ in **Figure 2.7** and $\alpha = 2°$ in **Figure 2.8**. It can be seen in **Figure 2.7** the estimated moment is reduced from 11.39 N-m to nearly 0.45 N-m and it is worth noting that the CRLSE method works for both positive and negative angles of attack, as long as the angle of attack is within the nearly linear portion of the flight regime. Similarly in **Figure 2.8**, the estimated moment is reduced from 13.95 N-m to 0.22 N-m which reduces

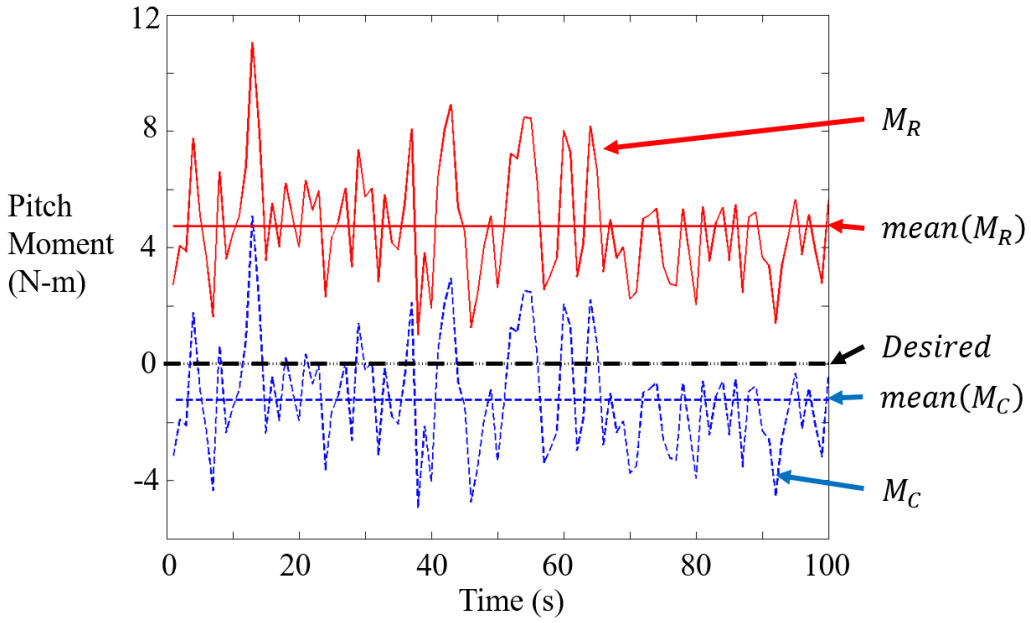

Figure 2.6: Comparison of uncalibrated and calibrated models for $V_\infty = 15$ m/s and $\alpha = 2°$ [48]

the error from the mapping function estimate to nearly 0. The CRLSE method will have different levels of effectiveness for different angles of attack and velocities however the general trends that the error in the estimate of the aerodynamic moment is greatly reduced.

These figures show a drastic reduction in error for the aerodynamic moment calculated using the calibration surfaces. A table summarizing the improvement for the four test flight conditions in **Figure 2.5** to **Figure 2.8** can be seen in the first four rows of **Table 2.7**. A new metric is used to quantify how effective the calibration method is, this metric is the factor of improvement and represents the percent reduction in the aerodynamic moment estimate error. It can be seen that the validation points experience high factors of improvement with

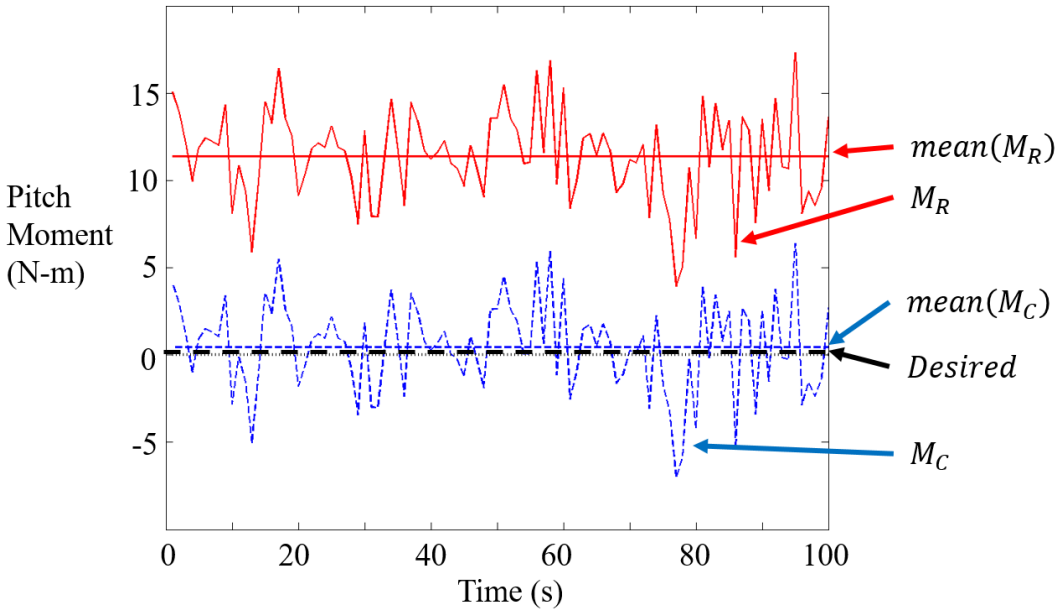

Figure 2.7: Comparison of uncalibrated and calibrated models for $V = 20$ m/s and $\alpha = -2°$ [48]

the minimum improvement of 86 percent and a maximum of 126 percent. The bottom half of **Table 2.7** shows that even for the training data there is a significant improvement in the moment estimate error with the smaller values for factor of improvement coming from cases which the initial moment estimate error was relatively low.

It can clearly be seen from this table that the CRLSE method to calibrate the mapping function greatly reduces the error in calculating the aerodynamic moment for an airfoil based on pressure measurements from the surface of the airfoil compared to the actual moment M_A. Every experiment case was used to evaluate the raw and calibrated aerodynamic moments

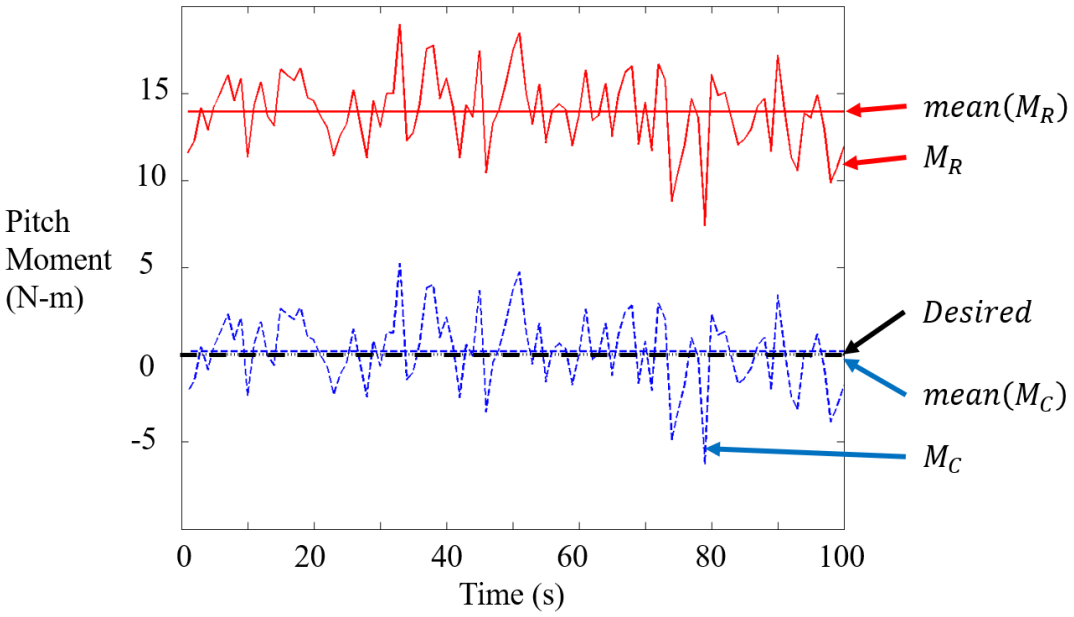

Figure 2.8: Comparison of uncalibrated and calibrated models for $V = 20$ m/s and $\alpha = 2°$ [48]

similar to the test cases, a summary of the results from this process can be seen in the bottom part of **Table 2.7**.

Table 2.7: Summary of Aerodynamic Moment Calculation Validation

Velocity (m/s)	α $(^\circ)$	M_A (Nm)	M_R (Nm)	M_C (Nm)	Factor of Improvement $(\frac{\lvert M_R - M_C \rvert}{M_R})$
15	0	0.0	4.25	-1.22	1.26
15	2	0.0	4.75	0.87	0.86
20	-2	0.0	11.39	0.45	0.96
20	2	0.0	13.95	0.22	0.98
10	-4	0.0	1.20	0.11	0.91
10	-2	0.0	2.82	-0.08	1.03
10	0	0.0	2.42	0.22	0.91
10	2	0.0	1.75	0.51	0.78
10	4	0.0	1.53	-0.76	1.50
15	-4	0.0	0.14	0.07	0.53
15	-2	0.0	4.25	-0.72	1.17
15	4	0.0	6.21	1.01	0.84
20	-4	0.0	6.33	0.43	0.87
20	0	0.0	13.94	0.10	0.99
20	4	0.0	11.65	-1.19	1.10
25	-4	0.0	5.07	-0.82	1.16
25	-2	0.0	18.78	1.23	0.93
25	0	0.0	22.17	-0.39	1.02
25	2	0.0	22.44	-0.73	1.03
25	4	0.0	22.36	0.74	0.97

2.6 Calibration of Aerodynamic Mapping Function Discussion

As shown in **Table 2.5** and **Table 2.7**, the error after model calibration in the simulation cases is smaller than that of wind tunnel experimental results. We attribute this to the fact that the simulations used a more complex geometry and four times as many sensors as in the experiments. Further, we expect that the simulation geometry, which included the sweep and dihedral angles, allowed the sensor locations to contribute more uniquely to the overall aerodynamic moment of the aircraft. As the number of sensors increases, the accuracy of the calibrated aerodynamic moments increases.

Another factor which contributes to the better performance in the simulations compared to the experiment results is the the way in which the noise was simulated. The noise in the simulations was assumed to be perfectly zero mean Gaussian. As validated later in the experiment, the distributions of the calibrated sensor reading and aerodynamic moments are similar to a zero-mean Gaussian. Thus the assumption about the noise used in **Eq. (2.3.1)** is reasonable. The simulations were also able to be ran with a pressure differential between the upper and bottom surfaces which will be inherently less sensitive to noise as any noise generated by inconsistency in the free stream velocity would be observed by both sensors simultaneously. Another possible source of error in the experimental results is the positioning of the sensors on the wing. For the experiment all of the sensors were placed along the center of the wing with no sensors on the control surface, where some flow information could

have been lost, though this did make the calculation of the mapping function significantly easier.

Although the results from the experimental model calibration perform worse than the simulations, the experimental calibration still significantly increases the accuracy of the moment model while remaining computationally tractable for execution on a standard desktop. With the addition of new state-of-the art sensor technologies this method could be implemented on larger sensor arrays as a means of accurately calibrating the moment model for any aircraft utilizing distributed flow sensors.

CHAPTER 3

FLOW MEASUREMENT BASED PITCH CONTROL

3.1 Flow Field Based Pitch Control

This chapter contains portions of a conference paper which was presented by the author at AIAA Scitech Forum 2017 [45]. In this work, relationships were established for how a change in angle of attack or sideslip angle changes the aerodynamic moment experienced by the aircraft. The relationships established were then used to create a robust PD controller based on measurements from sparse pressure sensors.

The relationships between the pressure field and the angle of attack α , side slip angle β , and incoming freestream airspeed V_∞, are first studied. Since only a qualitative relationship is required to form a feedback controller, an AVL simulation is conducted, although it cannot precisely calculate the pressure field for typical SUAV working Reynold regimes. The roll, pitch, and yaw moments are calculated from AVL using

$$\boldsymbol{m}_{AVL} = q_\infty s_{ref} \begin{bmatrix} b_{ref} C_l \\ c_{ref} C_m \\ b_{ref} C_n \end{bmatrix} \tag{3.1.1}$$

here q_∞ is the dynamic pressure, b_{ref} is the reference span, c_{ref} is the reference chord, and s_{ref} is the reference wing area which is found by multiplying b_{ref} and c_{ref} . C_l, C_m , and C_n are the roll, pitch, and yaw moment coefficients, found using AVL. The invariant mapping function established in **Eq. (2.2.2)**, is used to approximate the aerodynamic moment experienced by the fixed-wing SUAV based on the pressure measurements. As there is currently no sensor capable of simultaneously measuring pressure and shear on the surface of the SUAV wings, and as the shear terms have a relatively low impact on the aerodynamic moment within this Reynolds number regime, the shear measurements are assumed to be equal to zero. The pressure fields are generated using AVL based on the differences between the upper and lower surface pressure coefficients calculated at each node. In **Figure 3.1**, two sample images are shown. These images are taken from two separate time steps at angles of attack of (a) $\alpha = 8^\circ$ and (b) $\alpha = 10^\circ$. The color and size of the dots show the magnitude of the pressure coefficient differences, ΔC_p.

3.1.1 Flow Field Parameter Relationships

First, a relationship is constructed between the pressure profile changes with varying angles of attack. With the freestream velocity held constant at 20 m/s, the angle of attack is varied from 0° to 20° in increments of 4°. Due to limitations of AVL, the pressure on the upper and lower surfaces cannot be directly obtained, but the difference between these pressures is available, and can be used as a net pressure for calculating the aerodynamic moment

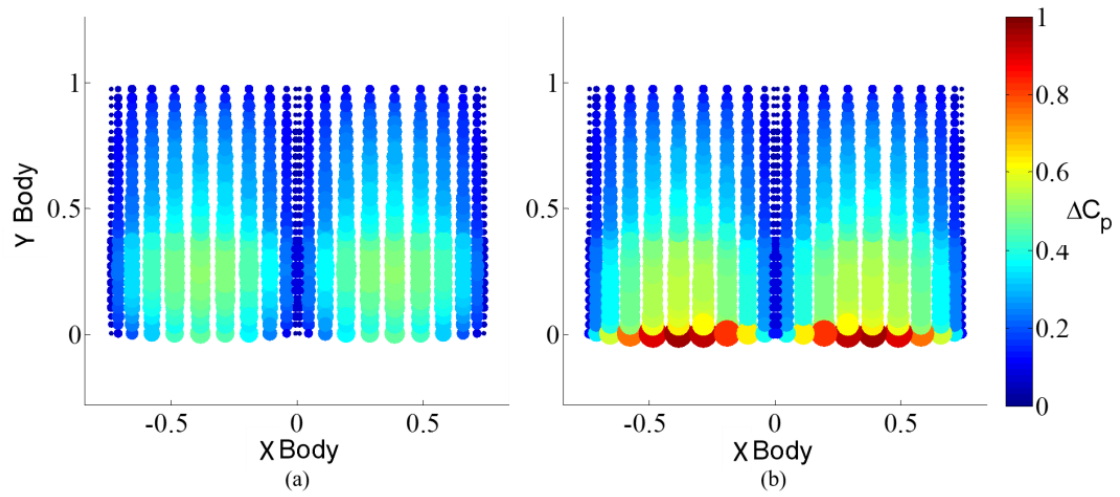

Figure 3.1: Sample Pressure Fields for (a) $\alpha = 8°$ and (b) $\alpha = 10°$ [45]

generated on the wing. This net pressure ΔC_p can be found using the following relationship

$$\Delta P = \Delta C_p q_\infty \tag{3.1.2}$$

3.1.2 Flow Pattern Relationships

It was found that as the angle of attack increases, the pressure difference between the upper and lower surfaces increases along the leading edge, with the pressure stabilizing near the quarter chord location, as expected for a rectangular wing. This trend shows that the sensors should be clustered near the leading edge of the wing, since these areas experience the greatest changes in pressure as the angle of attack changes. It is important to know a qualitative relationship between the change in pressure field with respect to changes in angle of attack, α. This relationship can be established by first selecting an angle of attack

and setting the control surface deflections at a trimmed condition. Then, while keeping the flap deflections constant, the angle of attack can be changed to see how the pitch moment calculated via the sensed pressure field changes. The moment error $\tilde{\boldsymbol{m}}$ can then be calculated by subtracting the pressure data generated by varying α from the trimmed pressure data, as

$$\tilde{\boldsymbol{m}} = M\left(\boldsymbol{q}_{trim} - \boldsymbol{q}\right) \tag{3.1.3}$$

here $\boldsymbol{q}_{trim}$ is the pressure profile at the trimmed angle of attack, $\boldsymbol{q}$ is the pressure profile for the varied angle of attack, and M is the mapping function. The equation above gives the total moment error, but for the case where there is only a change in angle of attack, the pitch moment is the only component of $\tilde{\boldsymbol{m}}$ which will change. This process is done for several velocities to ensure that the linear relationship is valid for all reasonable flight regimes. The results for this can be seen below in **Figure 3.2**, in which the approximate linear trend is self-evident within the flight regime.

Next, a relationship is constructed between the pressure profile changes with varying sideslip angles. For each angle of attack in the previous section, the sideslip angle, β, is changed from -10° to 10° by 5°. The change in the pressure profile for the right wing is inversely mirrored in the left wing, i.e. the right wing profile for β= -10° is the same as the left wing profile for β=10°. This relationship is expected as the aileron deflections are equal and opposite. Taking the left wing, as β increases, the change in pressure between the upper and lower surface decreases as the camber of this wing is decreasing, which will decrease the pressure on that section of the wing. Similarly, looking at the right wing, as β increases, the change in pressure between the upper and lower surface increases as the camber of the

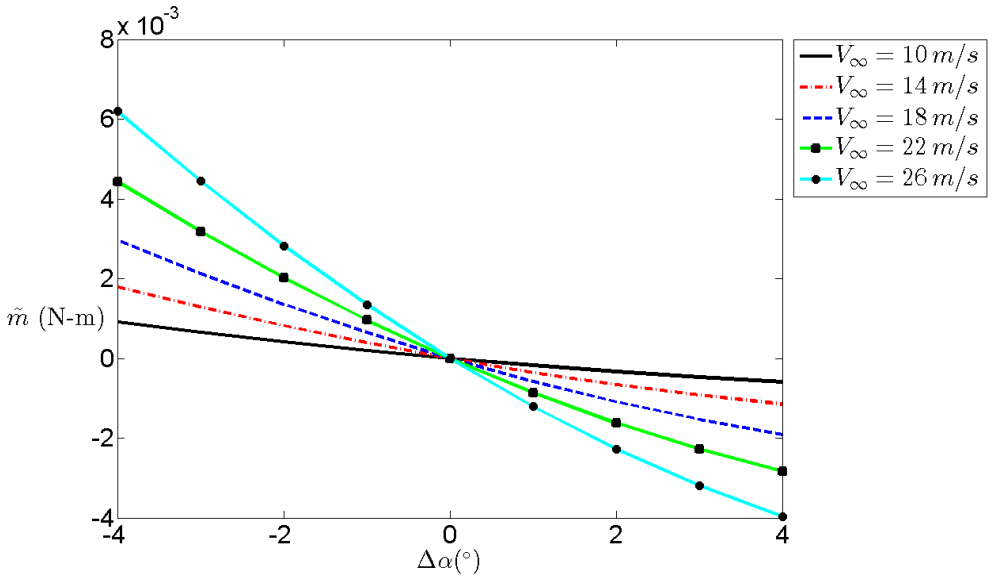

Figure 3.2: Change in Pitch Moment for Change in α [45]

wing is increasing which will increase the pressure on that section of the wing. Looking at a steeper angle of attack of 16°, it can be seen that the influence of the sideslip angle on the pressure profile is significantly reduced. Similar to the case for the pitch moment change as a function of change, the changes in the roll and yaw moments as a function of are also constructed here. To test this relationship, a constant angle of attack was set to be 10°. The trimmed sideslip angle was set to be 0°, and keeping the control surface deflections constant, the sideslip angle was varied by 4 degrees in both directions. The pressure measurements for each of these configurations was subtracted from the trimmed pressure measurement. This difference was then multiplied by the mapping function to find the moment generated by the error in sideslip angle. Similar to the results found from the pitch moment case, for both the roll moment **Figure 3.3** and yaw moment **Figure 3.4**, the moment as a function of the

changes in sideslip angle, $\Delta\beta$, exhibits a near linear behavior. This same methodology was evaluated at multiple velocities to verify that the linear trend held for all velocities within the flight envelope of the SUAV.

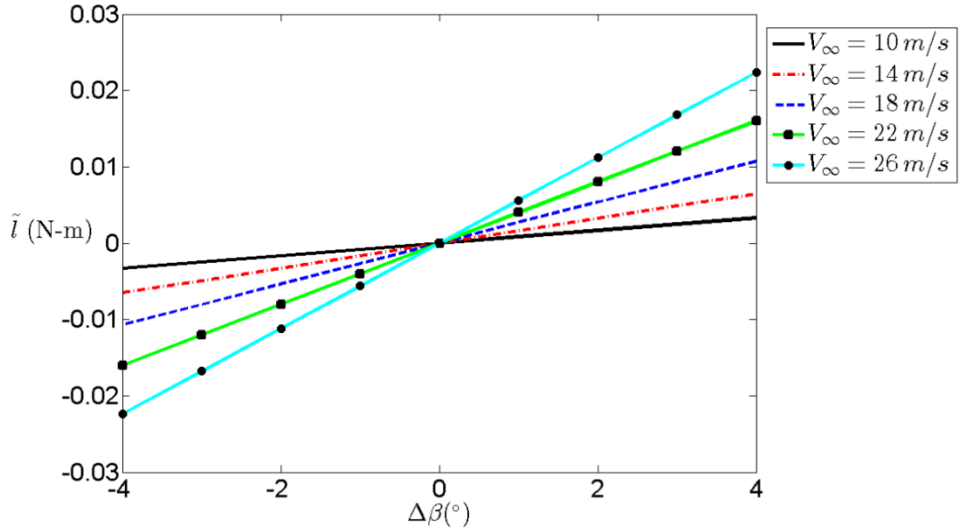

Figure 3.3: Change in Roll Moment for Change in β [45]

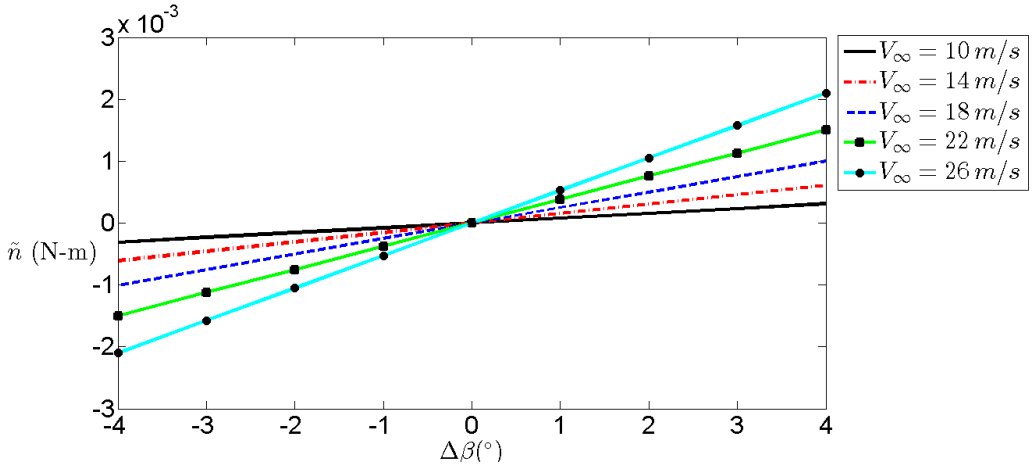

Figure 3.4: Change in Yaw Moment for Change in β [45]

3.1.3 Control Using Flow Field Patterns

The relationships established by these simulations provide the foundation for the creation of the PD robust controller based on pressure measurements. PD controllers are used to directly influence the error experienced by a system, if the change in aerodynamic moment is considered to be the state error, it is easy to implement a PD controller in this application. The performance of these controllers is increased if the relationship between the error and the state are linearly related, **Figure 3.2** demonstrates that the change in moment due to change in angle of attack is a linear relationship. **Figure 3.3** and **Figure 3.4** demonstrate that the change in moment caused by changes in sideslip angle result in a linear change in the moments in the roll, and yaw directions.

Using the above introduced pressure field pattern and mapping function, a nonlinear robust pitching moment controller is designed. The type of sensors utilized for this control is not important as long as they are capable of measuring pressure or shear and can be densely placed along the wing surface to reduce the mapping function induced error. The pitch only model of the SUAV [58] is given as

$$\begin{aligned} \dot{\theta} &= q \\ \dot{q} &= aM\boldsymbol{q}_{p,wf} + b\delta_e \end{aligned} \tag{3.1.4}$$

in which $a = 1/I_y$ and $b = M_{\delta_e}/I_y$. Here θ and q are the pitch angle and pitch rate, respectively. I_y is the moment of inertia along the body y axis and M_{δ_e} is the control power of the elevator. $\boldsymbol{q}_{p,wf}$ is the flow field on the wing-fuselage of a SUAV. In addition, $\hat{b}$ is

assumed to be the nominal values in the plant, and this uncertainty is bounded by $b\hat{b} = 1+d$, and $|d| < D \leq 1$. Here the pitching moment acting on the wing-fuselage can be calculated using **Eq. (2.2.2)**. The following pressure profile based controller is proposed:

$$\delta_e = (\hat{b})^{-1}\left[-\widehat{aM\boldsymbol{q}}_{p,wf} + \ddot{\theta}_d - k_1 M\tilde{\boldsymbol{q}}_{p,wf} - k_2 M\dot{\tilde{\boldsymbol{q}}}_{p,wf}\right] \tag{3.1.5}$$

Here $\tilde{\boldsymbol{q}}_{p,wf}$ is the image difference between the actual and desired pressure profile. The signs of the control gains k_1 and k_2 are case dependent. The uncertainty bound on the nominal value of the pitching moment calculated via the mapping function is given by $|M\boldsymbol{q}_{p,wf} - \widehat{M\boldsymbol{q}}_{p,wf}| \leq T$. The values of the control gains, k_1 and k_2 are case dependent and will be provided in the following brief proof of the asymptotic stability. The desired or trimmed values are represented by the subscript d.

Proof. Let us define the error between the desired and actual pitch angle to be $\tilde{\theta} = \theta - \theta_d$. The Lyapunov function is defined as $V = 0.5s^2 \geq 0$ in which $s = \dot{\tilde{\theta}} + \lambda M\tilde{\boldsymbol{q}}_{p,wf}$. Therefore, the derivative of s is

$$\begin{aligned}
\dot{s} &= \dddot{\tilde{\theta}} + \lambda M\dot{\tilde{\boldsymbol{q}}}_{p,wf} \\
&= \ddot{\theta} - \ddot{\theta}_d + \lambda M\dot{\tilde{\boldsymbol{q}}}_{p,wf} \\
&= aM\boldsymbol{q}_{p,wf} + b\hat{b}^{-1}\left(-\widehat{aM\boldsymbol{q}}_{p,wf} + \ddot{\theta}_d - k_1 M\tilde{\boldsymbol{q}}_{p,wf} - k_2 M\dot{\tilde{\boldsymbol{q}}}_{p,wf}\right) - \ddot{\theta}_d + \lambda M\dot{\tilde{\boldsymbol{q}}}_{p,wf} \\
&= a\left(M\boldsymbol{q}_{p,wf} - \widehat{M\boldsymbol{q}}_{p,wf}\right) + \lambda M\dot{\tilde{\boldsymbol{q}}}_{p,wf} - \left(k_1 M\tilde{\boldsymbol{q}}_{p,wf} + k_2 M\dot{\tilde{\boldsymbol{q}}}_{p,wf}\right) \\
&\quad + \Delta\left(-\widehat{aM\boldsymbol{q}}_{p,wf} + \ddot{\theta}_d\right) - \Delta\left(k_1 M\tilde{\boldsymbol{q}}_{p,wf} + k_2 M\dot{\tilde{\boldsymbol{q}}}_{p,wf}\right)
\end{aligned} \tag{3.1.6}$$

If we define F_1 and F_2 as follows

$$\begin{aligned} F_1 &= -\widehat{aM\boldsymbol{q}}_{p,wf} + \ddot{\theta}_d \\ F_2 &= k_1 M\tilde{\boldsymbol{q}}_{p,wf} + k_2 M\dot{\tilde{\boldsymbol{q}}}_{p,wf} \end{aligned} \tag{3.1.7}$$

Eq. (3.1.6) can be further simplified as

$$\dot{s} = a\left(M\boldsymbol{q}_{p,wf} - \widehat{M\boldsymbol{q}}_{p,wf}\right) + \lambda M\dot{\tilde{\boldsymbol{q}}}_{p,wf} + \Delta F_1 - (1+\Delta)\,F_2 \tag{3.1.8}$$

For Lyapunov stability $\dot{V} < 0$ for all values of k and λ, $\dot{V}$ can be found as follows

$$\begin{aligned} \dot{V} &= s\dot{s} \\ &= \left[a\left(M\boldsymbol{q}_{p,wf} - \widehat{M\boldsymbol{q}}_{p,wf}\right) + \lambda M\dot{\tilde{\boldsymbol{q}}}_{p,wf} + \Delta F_1 - (1+\Delta)\,F_2\right] s \end{aligned} \tag{3.1.9}$$

The control gains can be selected based on three cases depending on the sign of s.

Case 1: $s > 0$

$$\begin{aligned} \dot{V} = s\dot{s} &\leq -\eta s^2 \\ &\leq s\left[aT + \lambda M\dot{\tilde{\boldsymbol{q}}}_{p,wf} + D|F_1| - (1-D)F_2\right] \\ &= -\eta s^2 < 0 \end{aligned} \tag{3.1.10}$$

If we define f_1 as

$$f_1 = aT + \lambda M\dot{\tilde{\boldsymbol{q}}}_{p,wf} + D|T_1|$$

and solve for F_2, two solutions are found depending on the sign of $f_1 + \eta s$ as follows

$$F_2 = \begin{cases} \dfrac{f_1 + \eta s}{1-D} & \text{if } f_1 + \eta s > 0 \\ \\ \dfrac{f_1 + \eta s}{1+D} & \text{if } f_1 + \eta s < 0 \end{cases} \tag{3.1.11}$$

Case 2: $s < 0$

$$\begin{aligned} \dot{V} &= s\dot{s} \leq -\eta s^2 \\ &\leq s\left[-aT + \lambda M \dot{\tilde{\boldsymbol{q}}}_{p,wf} - D|F_1| - (1+D)F_2\right] \\ &= -\eta s^2 < 0 \end{aligned} \tag{3.1.12}$$

If we define f_2 as

$$f_2 = -aT + \lambda M \dot{\tilde{\boldsymbol{q}}}_{p,wf} - D|F_1|$$

and solve for F_2, two solutions are found depending on the sign of $f_2 + \eta s$ as follows

$$F_2 = \begin{cases} \dfrac{f_2 + \eta s}{1+D} & \text{if } f_2 + \eta s > 0 \\ \\ \dfrac{f_2 + \eta s}{1-D} & \text{if } f_2 + \eta s < 0 \end{cases} \tag{3.1.13}$$

Case 3: $s = 0$

In this case, $\dot{V} = s\dot{s} = 0$, and we let $f_2 = 0$. Thus for all three cases, $\dot{V} \leq 0$, however the second derivative, $\ddot{V}$, must also be bounded since $\dot{V} = 0$ does not guarantee asymptotic stability, $\ddot{V}$ can be found as

$$\ddot{V} = s\ddot{s} + \dot{s}^2 \tag{3.1.14}$$

which can be simplified as

$$\ddot{V} = \left[a\left(M\boldsymbol{q}_{p,wf} - \widehat{M\boldsymbol{q}}_{p,wf}\right) + \lambda M \dot{\tilde{\boldsymbol{q}}}_{p,wf} + \Delta F_1 - (1+\Delta)F_2\right]^2 \tag{3.1.15}$$

Since $a\left(M\boldsymbol{q}_{p,wf} - \widehat{M\boldsymbol{q}}_{p,wf}\right)$ is bounded by aT and $\Delta F_1 - (1+\Delta)F_2$ is bounded by $D|F_1|$ when F_2 is taken to be equal to zero, the $\lambda M\dot{\tilde{\boldsymbol{q}}}_{p,wf}$ term is the only one that it is not intuitive to be bounded. However, as $\dot{\tilde{\boldsymbol{q}}}_{p,wf}$ is a measured value, it can be assumed to be bounded, thus $\ddot{V}$ is bounded as follows

$$\ddot{V} \leq \left[aT + \lambda M\dot{\tilde{\boldsymbol{q}}}_{p,wf} + D|F_1|\right]^2 \tag{3.1.16}$$

With $\ddot{V}$ bounded, $\dot{V}$ can be shown to be uniformly continuous for all values of s. From Barbalats Lemma [59], since $V > 0$, $\dot{V} \leq 0$ and $\ddot{V}$ is bounded, it can be concluded that the closed loop system is asymptotically stable. □

3.1.4 Simulation of Flow Field Pattern Controller

For the simulation of the controller, the pressure information is generated using AVL based on the current flight status of the vehicle. The SUAV has three control surfaces: a differential pair of ailerons on the main wing, an elevator on the tail horizontal stabilizer, and a rudder on the vertical stabilizer. For the simulated pitching motion, the ailerons and rudder are fixed as the pitch moment can be directly influenced by the elevator. Each half of the wing has 15 sensors on the upper and lower surfaces of the wing located at the mid-span of the wing for a total of sixty pressure sensors which are uniformly distributed along the chord line. In the simulation, each sensor is assumed to only be able to measure the pressure information

at a location, with no shear information considered. **Figure 3.5** shows the pitching control diagram used in the simulation.

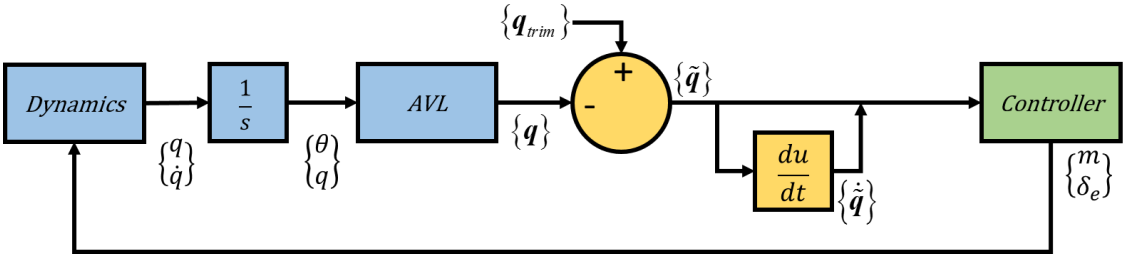

Figure 3.5: The Pitch Controller Diagram Based on Pressure Field Information [45]

3.1.4.1 Flow Field Pitch Controller Simulation Objectives

For the simulation of the pitching controller two cases were evaluated, disturbance rejection and pitching output tracking. To test the disturbance rejection properties of the robust pitching controller, a trim condition is selected as the initial and desired angle of attack. An impulse change in angle of attack is applied at the first time step to ensure that the controller will return to the trim condition in the presence of disturbances in the pressure field. For this simulation, the desired and initial angle of attack was set to be 8° and the magnitude of the disturbance was set to be 0.5°. Random noise is generated and is used by both the robust and constant gain PD controllers for comparison of performance. The constant gains used by the constant gain PD controller are -1 and -10 for k_1 and k_2 respectively. The plots for α, $\dot{q}$ and δ for a simulation time of 10 seconds can be seen below in **Figure 3.6**, which

show that both the PD and robust controllers achieve the goal of rejecting the perturbation of 0.5°.

3.1.4.2 Flow Field Pitch Controller Simulation Parameters

At each time step the difference between the desired pressure profile and the current pressure profile are found and used to determine the new elevator deflection following the robust controller **Eq. (3.1.4)** with λ set to be -10000 and η set to be 0.01. For comparison, a constant gain PD controller was also developed where the signs of k_1 and k_2 where the signs and magnitudes of the gains are selected based on the following relationship.

$$\ddot{\tilde{\theta}} + k_2\dot{\theta} + k_1 c\theta = 0 \tag{3.1.17}$$

where c is an unknown negative constant, the eigenvalues of this system must have negative real parts for stability, if k_1 and $k_2 < 0$ and are carefully tuned, values for k_1 and k_2 can be obtained such that the system will exhibit a stable response.

3.1.4.3 Flow Field Pitch Controller Simulation Results

For this simulation, the desired and initial angle of attack was set to be 8° and the magnitude of the disturbance was set to be 0.5°. Random noise is generated and is used by both the robust and constant gain PD controllers for comparison of performance. The constant gains

used by the constant gain PD controller are -1 and -10 for k_1 and k_2 respectively. The plots for α, $\dot{q}$ and δ for a simulation time of 10 seconds can be seen below in **Figure 3.6**, which show that both the PD and robust controllers achieve the goal of rejecting the perturbation of 0.5°.

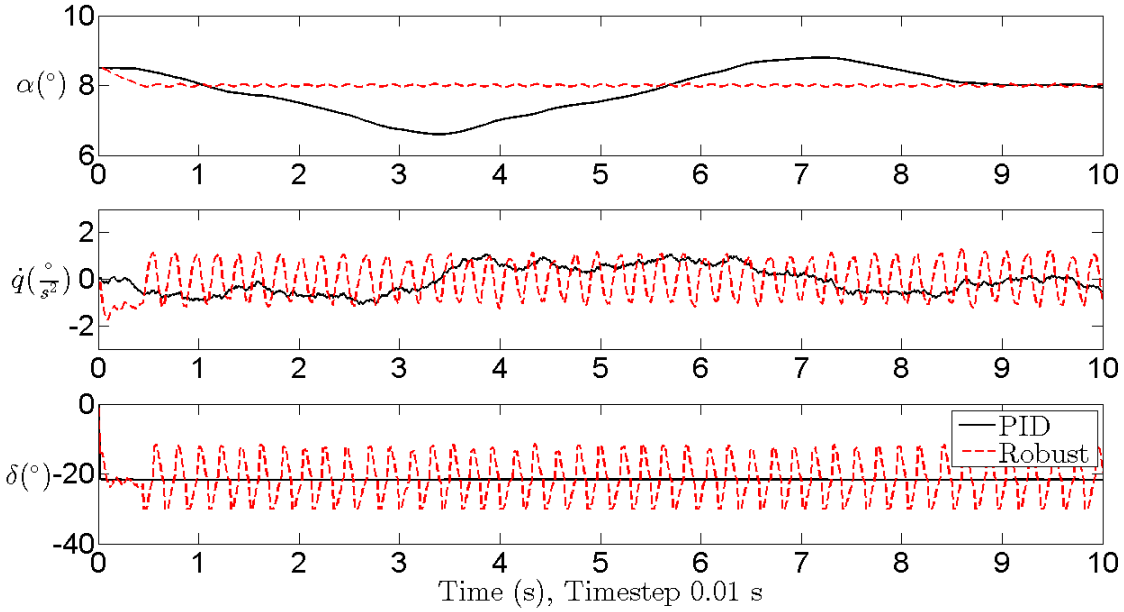

Figure 3.6: 0.5° Disturbance Rejection Simulation Results for α, $\dot{q}$ and δ [45]

It can be seen that the overshoot experienced by the robust controller is less than that seen of the PD controller while having a faster rise time, 1 second for the robust controller and 10 seconds for the PD controller. These features demonstrate that the robust controller outperforms the constant gain controller as it is able to reject the disturbance faster with less overshoot while remaining robust to modeling uncertainty that inevitably exists in all dynamic systems.

The second simulation scenario tested is that of output tracking, where the controller will transfer the SUAV from an initial stable condition to a different final stable condition. The initial stable condition is chosen to be a trim condition and the final condition is chosen to be a trim condition of either 4° above or below the initial angle of attack. The initial angle of attack was selected to be 12° with the final angle of attack chosen to be 8°. The plots for α, $\dot{q}$ and δ for a simulation time of 10 seconds can be seen below in **Figure 3.7**, which show that both the PD and robust controllers achieve the goal of output tracking for transferring the SUAV from a trimmed angle of attack of 8° to 12°.

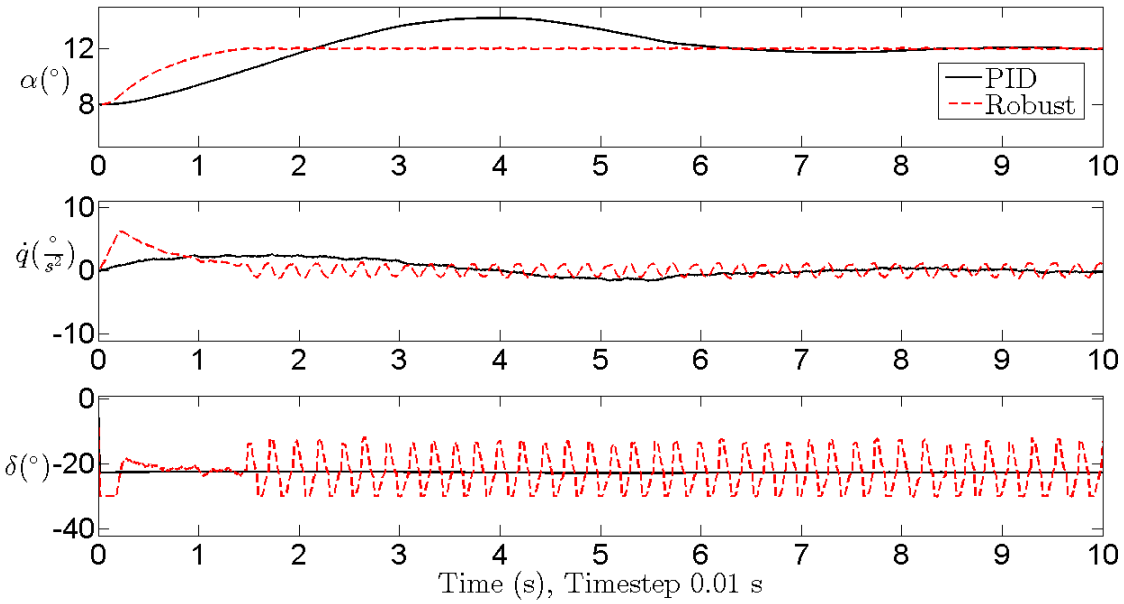

Figure 3.7: Output Tracking Simulation for $\alpha = 8°$ to $\alpha = 12°$ Results for α, $\dot{q}$ and δ [45]

It can be seen that both the robust controller and constant gain controllers are both capable of tracking the angle of attack from an initial angle of attack to a final angle of

attack. However, the robust controller has a faster 2% rise time of 1.5 seconds compared to the constant gain controller rise time of 2 seconds. It can also be seen that that the overshoot experienced by the robust controller is lower than that of the constant gain controller.

3.1.4.4 Flow Field Simulation Discussion

The results from both simulation cases validate the use of the pressure field information in a robust pitch attitude controller. These results also show that the performance improvements for the robust controller over the constant gain controller are significant. It also demonstrates the utility of this controller's implementation in an actual SUAV system by greatly increasing the stability properties of the aircraft. The changes in flow around the SUAV are the leading cause of instability in aircrafts of this size. The ability to detect flow changes and quickly adjust the control commands based on these changes in pressure directly is a significant advantage to the constant gain controller and existing inertial measurement based controllers. The linear relationships seen in **Figure 3.2**, **Figure 3.3** and **Figure 3.4**, allow the robust control to be easily implemented in an actual system as the trim conditions for the SUAV can be easily calculated off-line and interpolated within the flight regime to determine any intermediate trim conditions quickly. These linear relationships also demonstrate that the robust pitch controller can also easily be adapted to be a 3D robust attitude controller capable of controlling the roll, pitch and yaw to increase overall SUAV stability.

3.2 Flow Image Based Pitch Control

In the flow field controller [45], not all of the sensed information has been fully utilized in designing a unified controller for SUAVs. This section covers work that is currently under review with the title "Flow Field Image Based Attitude Control for Small Unmanned Aerial Vehicles". Here, a new control approach is studied working directly on the error between the desired and actual sensed flow field images. Example operators over images are summation/subtraction, integration, differentiation, and mapping. The differences between a typical flight controller, a pressure sensor based flight controller [6,44], and the new control approach studied here are illustrated in **Figure 3.8**. In a conventional flight control system as shown in **Figure 3.8a**, rigid body sensors such as IMU, speed indicator, and altimeter are used in navigation and control of an aircraft. Normally, aerodynamic coefficients, stability derivatives, and control derivatives needed in flight controllers are obtained offline via wind tunnel and/or flight tests. For low inertia aircraft like SUAVs, the aforementioned parameters can be very different from the values obtained offline or sometimes are not available. In **Figure 3.8b**, the aerodynamic moments used in a controller are approximately computed using a finite number of pressure measurements [44]. In the new control approach studied here **Figure 3.8c**, the control command operates on the error between the actual and desired flow field images, while rigid body sensor information is only used to augment the control system. Erroneous flow field images are manipulated before being sent into the flight controller.

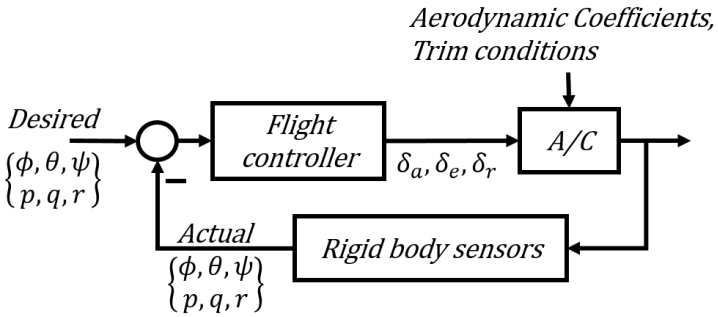

(a) Conventional A/C Controller, "A/C" means aircraft

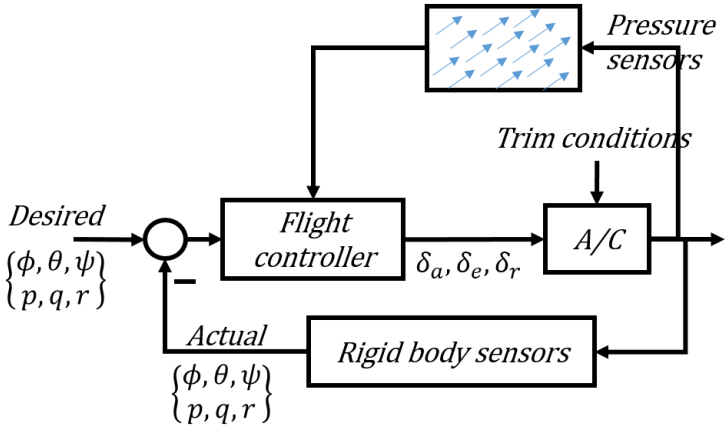

(b) Pressure Sensor based A/C Controller

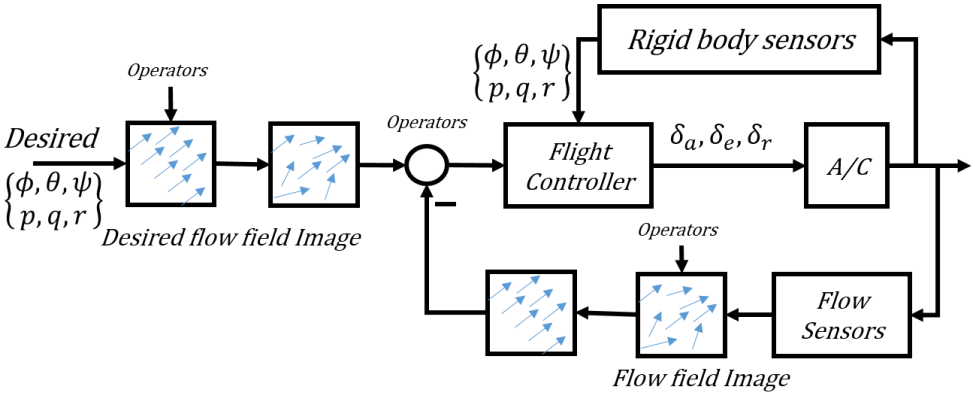

(c) Flow Field Image based A/C Controller

Figure 3.8: Comparisons among rigid body sensor driven conventional A/C controller, pressure sensor based A/C controller, and proposed flow field image based A/C controller

3.2.1 Flow Image Generation

The flow measurement can be aggregated in a 2D or 3D image. For example, the pressure field on a wing generated using the Athena Vortex Lattice (AVL) [56] software can be converted into a 2D image as shown in **Figure 3.9**, where at each sensor location, the normal pressure coefficient differential is plotted.

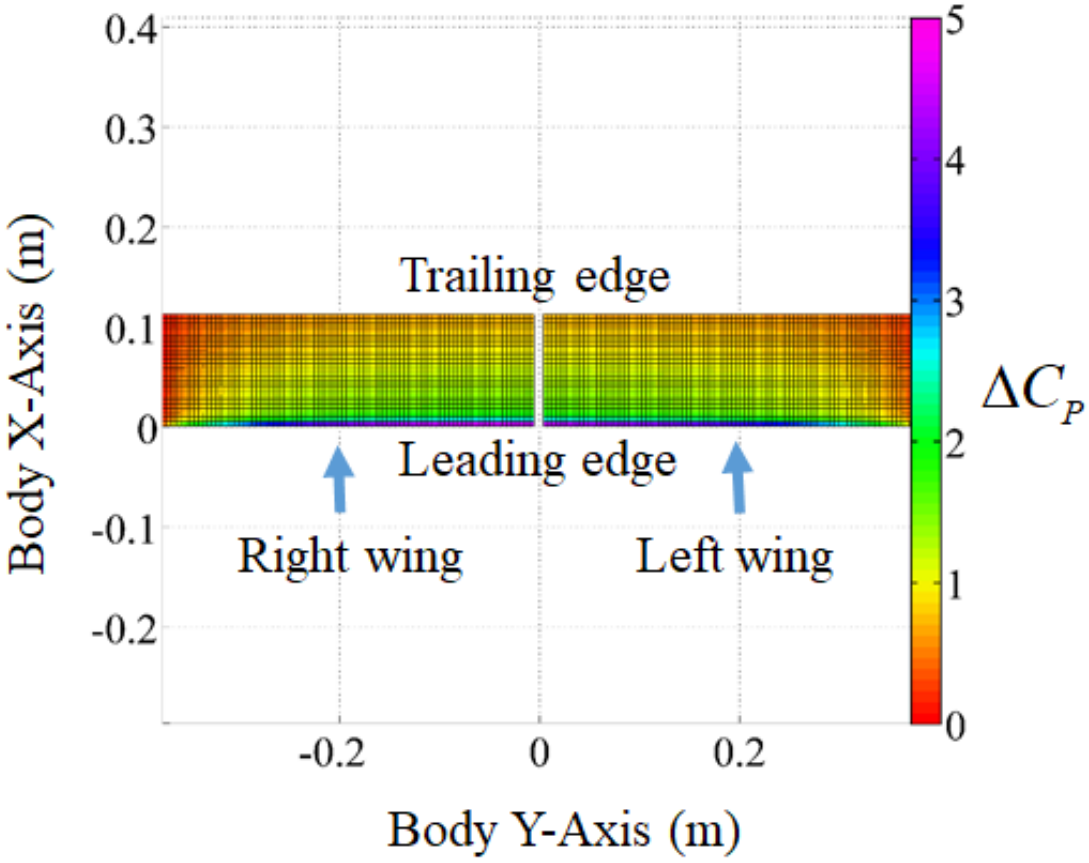

Figure 3.9: Pressure Image Generated Using AVL Pressure Measurements

The flow images are created by taking a discrete number of pressure measurements on the surface of the aircraft and linearly interpolating between them. This interpolation

process is constructed such that the new sensor locations form uniform "pixels" in the flow image to be used for estimating the aerodynamic moment via the mapping function.

3.2.2 Flow Image Operators

Let us denote a flow field image frame k as I_k, which could be 2D or 3D. In each pixel location i of the image, (x_i, y_i) for 2D or (x_i, y_i, z_i) for 3D, the corresponding flow information is represented by $\xi_{k,i}$. This information can be either a scalar (e.g. a pressure reading from pressure sensors or a wall-shear stress reading from hair sensors) or a vector (e.g. pressure and shear readings from hybrid sensors). It is assumed that there are a total of n_p sensors aboard a SUAV, which means there are n_p pixels in the flow image. A "unit image" *1* means $\xi_i = 1$ for all the pixels, whereas a "zero image" *0* means $\xi_i = 0$ for all the pixels.

3.2.2.1 Image operators

To facilitate the implementation of airflow field image into control designs, the following operations on flow field images are defined. It is worth noting that for different flow sensor generated images, the number of pixels and their physical locations on the surface of a fixed-wing SUAV are invariant in the A/C body coordinate system. The first group includes six point-wise operators:

Operation 1 - Addition/Subtraction: $I_3 = I_1 \pm I_2$ means $\xi_{3,i} = \xi_{1,i} \pm \xi_{2,i}$, $\forall i = 1, ..., n_p$.

Operation 2 - Power: $I_2 = I_1^k$ means $\xi_{2,i} = \xi_{1,i}^k$, $\forall i = 1, ..., n_p$. Here if $\xi_{1,i}$ represents vector information, $\xi_{1,i}^k$ will be each element of $\xi_{1,i}$ raised to the power of k.

Operation 3 - Affine: $I_2 = aI_1 + b$ means $\xi_{2,i} = a\xi_{1,i} + b$, $\forall i = 1, ..., n_p$. Here a and b are constant scalars. A special case is: when $a = -1$ and $b = 0$, $I_2 = -I_1$.

Operation 4 - Integration: $\int_{t_0}^{t_f} I_1 dt$ means $\int_{t_0}^{t_f} \xi_{1,i} dt$, $\forall i = 1, ..., n_p$.

Operation 5 - Differentiation: $\frac{d}{dt} I_1$ means $\frac{d}{dt} \xi_{1,i}$, $\forall i = 1, ..., n_p$.

Operation 6 - Point-wise Multiplication: $I_3 = I_1 * I_2$ means $\xi_{3,i} = \xi_{1,i} * \xi_{2,i}$, $\forall i = 1, ..., n_p$. Similar to Operator 2, if $\xi_{1,i}$ and $\xi_{2,i}$ include vector information, $\xi_{1,i} * \xi_{2,i}$ means each element in these two vectors are multiplied.

The second group of operators are those work on "a whole" or "a part" of an airflow field image:

Operation 7 - Sum: $sum(I)$ means all the values in image I are added together. If ξ_i is a vector, then corresponding components in the vector are added together.

Operation 8 - Aggregation: a vector $\boldsymbol{I}_1$ is a column vector of $[\xi_{1,1}, \xi_{1,2}, ..., \xi_{1,n_p}]^T$, where the superscript "T" represents a vector transpose.

The last group of operators includes all "mapping" operations, which are used to abstract high dimensional airflow information into low dimensional aerodynamic parameters, particularly for fixed-wing SUAVs. The mapping operator M on an aggregated vector $\boldsymbol{I}$,

$M\boldsymbol{I} = \sum_{i=1}^{n_p} M_i \xi_i$ is used to obtain a physical quantity with a lower dimension from the flow field image. Different mapping operators can be defined to find aerodynamic force, aerodynamic moment, angle of attack, center of pressure, etc. In this study, only the mapping function used in computing aerodynamic moments is listed, which is used in the controller designs.

Operation 9 - Mapping for Aerodynamic Moments: The mapping operator used to calculate the aerodynamic moment M is fully determined by the position vector of the sensors with respect to the mass center of the A/C and the rotation matrix from the sensor's local coordinate to the aircraft body coordinate. Based on [6] the aerodynamic moment $\mathbf{m}$ can be written as

$$\boldsymbol{m} = \sum_{i=1}^{n_p} s_i[\boldsymbol{r}_i \times (R_i \boldsymbol{q}_i)] \tag{3.2.1}$$

where s_i represents the effective area covered by the i^{th} sensor, $\boldsymbol{r}_i$ is the position vector from the sensor location to the origin of the SUAV body coordinate, $\boldsymbol{q}_i = [\tau_{x,i}, \tau_{y,i}, p_i]^T$ is the shear and pressure measurements of sensor i, and R_i is the rotation matrix from the local surface element coordinate frame to the body coordinate frame. Thus the mapping operator for calculating the aerodynamic on the flow field image aggregation $\boldsymbol{I} = [\boldsymbol{q}_1^T, \boldsymbol{q}_2^T, ..., \boldsymbol{q}_{n_p}^T]^T$ is

$$M = [M_1, ..., M_{n_p}], M_i = s_i \boldsymbol{r}_i \times R_i, i = 1, 2, ..., n_p \tag{3.2.2}$$

Thus, Eq. 3.2.1 can be rewritten as

$$\boldsymbol{m} = M\boldsymbol{I} \tag{3.2.3}$$

3.2.2.2 Image Operator Properties

The properties used in deriving the flow image based controllers are introduced here.

Property 1 - Commutative: Operators 1, 3, 4, and 5 are commutative with Operator 8 and Operator 9. In specific, $M(\boldsymbol{I}_1+\boldsymbol{I}_2) = M\boldsymbol{I}_1+M\boldsymbol{I}_2$, $M(\boldsymbol{I}_1-\boldsymbol{I}_2) = M\boldsymbol{I}_1-M\boldsymbol{I}_2$, $M(\alpha\boldsymbol{I}_1+b) = \alpha M\boldsymbol{I}_1 + Mb$, $\frac{d}{dt}M\boldsymbol{I} = M\frac{d}{dt}\boldsymbol{I}$ and $\int_{t_0}^{t_f} M\boldsymbol{I}_1 dt = M\int_{t_0}^{t_f}\boldsymbol{I}_1 dt$.

Property 2: Through the definitions above, the flow field images can be converted from one to another. For example, the pressure sensor network onboard of a SUAV will generate a pressure image I_p, and the hair sensor outputs wall-shear stress information which can be correlated with a local flow velocity image I_v. According to the Bernoulli theorem [57], the relationship between these two images is $I_p = I_{p0} - 1/2\rho I_v^2$, in which ρ is the air density, and I_{p0} is an image with all the pixel values equal to the static pressure.

3.2.3 Control using Flow Image

Based on the image operators and their properties, a simple pitching controller based on real time flow images is designed here. The flow sensors used can be either hair sensors or pressure sensors. The pitch dynamics of a SUAV is

$$\begin{aligned}\dot{\theta} &= q \\ \dot{q} &= aM\boldsymbol{I}_{p,wf} + b\delta_e\end{aligned} \tag{3.2.4}$$

in which $a = 1/J_y$ and $b = M_{\delta_e}/J_y$. Here θ and q are the pitch angle and pitch rate, respectively. J_y is the moment of inertia about the body y axis and M_{δ_e} is the control derivative of the elevator. $\boldsymbol{I}_{p,wf}$ is the flow image on the wing-fuselage of a SUAV. The uncertainty of the nominal values of the plant $\hat{b}$ is bounded by $b = (1+d)\hat{b}$, and $|d| < D \leq 1$. The pitching moment calculated using **Eq. (3.2.3)** with measurements from a finite number of onboard flow sensors is not accurate, and its uncertainty is bounded by $|M\boldsymbol{I}_{p,wf} - \widehat{M\boldsymbol{I}}_{p,wf}| \leq F$. The following flow image based controller is proposed:

$$\delta_e = (\hat{b})^{-1}\left[-a\widehat{M\boldsymbol{I}}_{p,wf} + \ddot{\theta}_d - k_1 M\tilde{\boldsymbol{I}}_{p,wf} - k_2 M\dot{\tilde{\boldsymbol{I}}}_{p,wf}\right] \tag{3.2.5}$$

Here $\tilde{\boldsymbol{I}}$ is the image difference between the actual and desired flow field. The signs of the control gains k_1 and k_2 are case dependent. ***Lemma 1****: It is assumed that the system is perfectly known (i.e., $d = 0$ and $F = 0$). In order to have the closed-loop system formed by* ***Eq. (3.2.4)*** *and* ***Eq. (3.2.5)*** *to be asymptotically stable, $k_2 < 0$ must be satisfied. The closed-loop system response depends on the selection of $k_2 < 0$ and k_1.*

Proof. Since the model is assumed to be perfectly known, for brevity, the nominal value symbols are omitted in the proof. Substitute **Eq. (3.2.5)** into **Eq (3.2.4)**, the closed-loop system becomes

$$\ddot{\theta} = \ddot{\theta}_d - k_1 M\tilde{\boldsymbol{I}}_{p,wf} - k_2 M\dot{\tilde{\boldsymbol{I}}}_{p,wf} \tag{3.2.6}$$

Therefore, the error dynamics ($\tilde{\theta} = \theta - \theta_d$) is derived as

$$\dddot{\tilde{\theta}} + k_1 M\tilde{\boldsymbol{I}}_{p,wf} + k_2 M\dot{\tilde{\boldsymbol{I}}}_{p,wf} = 0 \tag{3.2.7}$$

For a pitch stable SUAV and before stall, the partial derivative of the pitching moment coefficient, C_m, with respect to the angle of attack, α, is negative, (i.e. $\partial C_m/\partial\alpha < 0$). In a pitching only motion, there is a constant bias between the angle of attack and the pitch angle. Thus, $M\tilde{\boldsymbol{I}}_{p,wf} = c\tilde{\theta}$ and c is an unknown negative constant. Therefore, **Eq. (3.2.7)** can be rewritten as

$$\ddot{\tilde{\theta}} + k_2 c\dot{\theta} + k_1 c\theta = 0 \tag{3.2.8}$$

The eigenvalues of the error dynamics are

$$\lambda_{1,2} = \frac{-k_2 c \pm \sqrt{(k_2 c)^2 - 4k_1 c}}{2} \tag{3.2.9}$$

The eigenvalues can be real or a complex conjugate pair. In order to have two negative real part eigenvalues, k_2 must be negative. If k_1 and $k_2 < 0$ are carefully tuned, two real values can be obtained, and the closed-loop system will have flat responses. If k_1 and $k_2 < 0$ are selected such that a pair of complex conjugate eigenvalues are achieved, the closed-loop system will have oscillatory responses. □

Theorem 1: *With the bounded uncertainties* $b = (1+d)\hat{b}, |d| < D \leq 1$ *and* $|M\boldsymbol{I}_{p,wf} - \widehat{M\boldsymbol{I}}_{p,wf}| \leq F$*, the closed-loop system formed by* ***Eq. (3.2.4)*** *and* ***Eq. (3.2.5)*** *is asymptotically stable with properly selected control gains listed in the proof shown below.*

Proof. Let us define the error between the actual and desired pitch angles to be $\tilde{\theta} = \theta - \theta_d$. The Lyapunov function is defined as $V = 0.5s^2 \geq 0$ in which $s = \dot{\tilde{\theta}} + \lambda M\tilde{\boldsymbol{I}}_{p,wf}$. Therefore

the derivative of s is

$$\begin{aligned}
\dot{s} &= \ddot{\tilde{\theta}} + \lambda M \dot{\tilde{\boldsymbol{I}}}_{p,wf} \\
&= \ddot{\theta} - \ddot{\theta}_d + \lambda M \dot{\tilde{\boldsymbol{I}}}_{p,wf} \\
&= aM\boldsymbol{I}_{p,wf} \\
&+ b\hat{b}^{-1}\left(-a\widehat{M\boldsymbol{I}}_{p,wf} + \ddot{\theta}_d - k_1 M\tilde{\boldsymbol{I}}_{p,wf}\right. \\
&\left.-k_2 M\dot{\tilde{\boldsymbol{I}}}_{p,wf}\right) - \ddot{\theta}_d + \lambda M\dot{\tilde{\boldsymbol{I}}}_{p,wf} \\
&= a\left(M\boldsymbol{I}_{p,wf} - \widehat{M\boldsymbol{I}}_{p,wf}\right) + \lambda M\dot{\tilde{\boldsymbol{I}}}_{p,wf} \\
&- \left(k_1 M\tilde{\boldsymbol{I}}_{p,wf} + k_2 M\dot{\tilde{\boldsymbol{I}}}_{p,wf}\right) \\
&+ \Delta\left(-a\widehat{M\boldsymbol{I}}_{p,wf} + \ddot{\theta}_d\right) \\
&- \Delta\left(k_1 M\tilde{\boldsymbol{I}}_{p,wf} + k_2 M\dot{\tilde{\boldsymbol{I}}}_{p,wf}\right)
\end{aligned} \tag{3.2.10}$$

If we define T_1 as $-a\widehat{M\boldsymbol{I}}_{p,wf} + \ddot{\theta}_d$ and T_2 as $k_1 M\tilde{\boldsymbol{I}}_{p,wf} + k_2 M\dot{\tilde{\boldsymbol{I}}}_{p,wf}$, **Eq. (3.2.10)** can be further simplified as

$$\dot{s} = a\left(M\boldsymbol{I}_{p,wf} - \widehat{M\boldsymbol{I}}_{p,wf}\right) + \lambda M\dot{\tilde{\boldsymbol{I}}}_{p,wf} + \Delta T_1 - (1+\Delta)T_2 \tag{3.2.11}$$

The derivative of the Lyapunov function $\dot{V}$ is

$$\begin{aligned}
\dot{V} &= s\dot{s} \\
&= \left[a\left(M\boldsymbol{I}_{p,wf} - \widehat{M\boldsymbol{I}}_{p,wf}\right) + \lambda M\dot{\tilde{\boldsymbol{I}}}_{p,wf} + \Delta T_1 - (1+\Delta)T_2\right] s
\end{aligned} \tag{3.2.12}$$

There are three cases to select the combined control term T_2 based on the sign of s.

Case 1: $s > 0$

$$\begin{aligned}\dot{V} &= s\dot{s} \\ &\leq s\left(aF + \lambda M\dot{\tilde{\boldsymbol{I}}}_{p,wf} + D|T_1| - T_2 + D|T_2|\right) \\ &= -\eta s^2 < 0\,,\ \eta > 0\end{aligned} \tag{3.2.13}$$

If we define f_1 as $aF + \lambda M\dot{\tilde{\boldsymbol{I}}}_{p,wf} + D|T_1|$, two solutions of T_2 can be found depending on the sign of $f_1 + \eta s$ as follows

$$T_2 = \begin{cases} \dfrac{f_1 + \eta s}{1 - D} & \text{if } f_1 + \eta s > 0 \\ \\ \dfrac{f_1 + \eta s}{1 + D} & \text{if } f_1 + \eta s < 0 \end{cases} \tag{3.2.14}$$

Case 2: $s < 0$

$$\begin{aligned}\dot{V} &= s\dot{s} \\ &\leq s\left[-aF + \lambda M\dot{\tilde{\boldsymbol{I}}}_{p,wf} - D|T_1| - T_2 - D|T_2|\right] \\ &= -\eta s^2 < 0\end{aligned} \tag{3.2.15}$$

If we define f_2 as

$$f_2 = -aF + \lambda M\dot{\tilde{\boldsymbol{I}}}_{p,wf} - D|T_1|$$

and solve for T_2, two solutions are found depending on the sign of $f_2 + \eta s$ as follows

$$T_2 = \begin{cases} \dfrac{f_2 + \eta s}{1 + D} & \text{if } f_2 + \eta s > 0 \\ \\ \dfrac{f_2 + \eta s}{1 - D} & \text{if } f_2 + \eta s < 0 \end{cases} \tag{3.2.16}$$

Case 3: $s = 0$

In this case, $\dot{V} = s\dot{s} = 0$, and we let $T_2 = 0$. Therefore, considering all three cases, $\dot{V}(x,t) \leq 0$. When $s = 0$,

$$\ddot{V} = s\ddot{s} + \dot{s}^2 = \dot{s}^2 \tag{3.2.17}$$

which after inserting the controller **Eq. (3.2.5)** can be further reduces to

$$\begin{aligned} \ddot{V} &= \left[a\left(M\boldsymbol{I}_{p,wf} - \widehat{M\boldsymbol{I}}_{p,wf}\right) + \lambda M\dot{\hat{\boldsymbol{I}}}_{p,wf} + \Delta T_1 - (1+\Delta)T_2\right]^2 \\ &\leq aF + \lambda M\dot{\hat{\boldsymbol{I}}}_{p,wf} + D|T_1| \end{aligned} \tag{3.2.18}$$

It is worth noting that $a\left(M\boldsymbol{I}_{p,wf} - \widehat{M\boldsymbol{I}}_{p,wf}\right)$ is bounded by aF and $T_2 = 0$. Here $\ddot{\theta}_d$ is desired value and in practial should be always bounded. As the nominal value of the image moment $\widehat{M\boldsymbol{I}}_{p,wf}$ is a measured value, it is also bounded. Similarly the time derivative of the nominal moment is measured and bounded which makes the term $\lambda M\dot{\hat{\boldsymbol{I}}}_{p,wf}$ also bounded. Therefore $\ddot{V} = \dot{s}^2$ is bounded showing that $\dot{V}$ is uniformly continuous. Based on the Barbalat's Lemma in [59], since $V \geq 0$ is lower bounded, $\dot{V} \leq 0$, and $\ddot{V}$ is bounded, the closed-loop system is asymptotically stable. □

3.2.4 Simulation of Flow Image Controller

3.2.4.1 Flow Image Pitch Controller Simulation Objectives

Two simulation cases are conducted to validate the proposed pitch-axis attitude control. In Case 1A (output tracking), the SUAV pitch angle is commanded to track a new trimmed

pitch angle. In Case 1B (wind gust rejection), the SUAV pitch angle is stabilized when facing a simulated gust. In both of these cases, the rise time in the pitch angle should be less than 1 second with less than 5 % overshoot while the elevator deflection is less than the limit of the aileron of ± 60 degrees.

3.2.4.2 Flow Image Pitch Controller Simulation Parameters

For both simulations, the uncertainty bounds D and F are assumed to be $D = 2.0 \times 10^{-4}$ and $F = 5 \times 10^{-5}$ N-m. These uncertainty bounds are selected as roughly 10% of their respective nominal values. The control parameters λ and η after tuning are selected to be $\lambda = 205$ and $\eta = 32.5$.

3.2.4.3 Flow Image Pitch Controller Simulation Results

Simulation Case 1A: The initial pitch angle is $\theta = 13^\circ$ and the desired pitch angle is $\theta_d = 7^\circ$. The pitch angle time history can be seen in **Figure 3.10** and the elevator deflection can be seen in **Figure 3.11**. It can be observed that the rise time is less than 1 second and the steady state error is within 5 % and the elevator does not exceed the maximum deflection of $\pm 60^\circ$. In **Figure 3.12**, the magnitude of the image error is shown at 3 different time steps, and it can be seen that the image error goes to zero at the end of the simulation time.

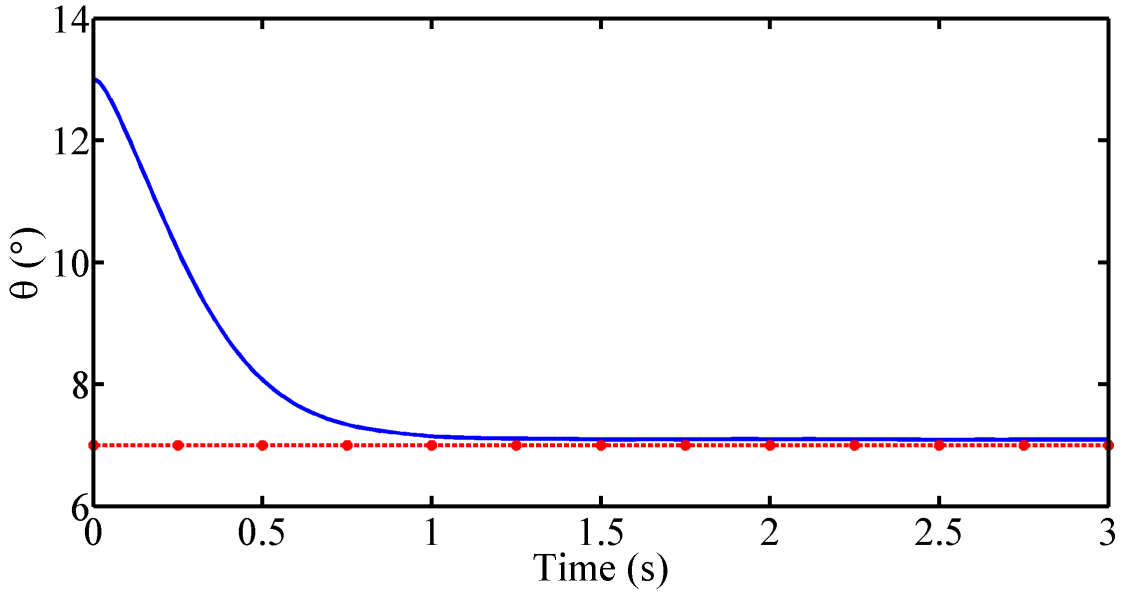

Figure 3.10: Pitch angle for the Tracking Controller Driving $\theta = 13°$ to $\theta_d = 7°$, Where the Dotted Line Represents θ_d

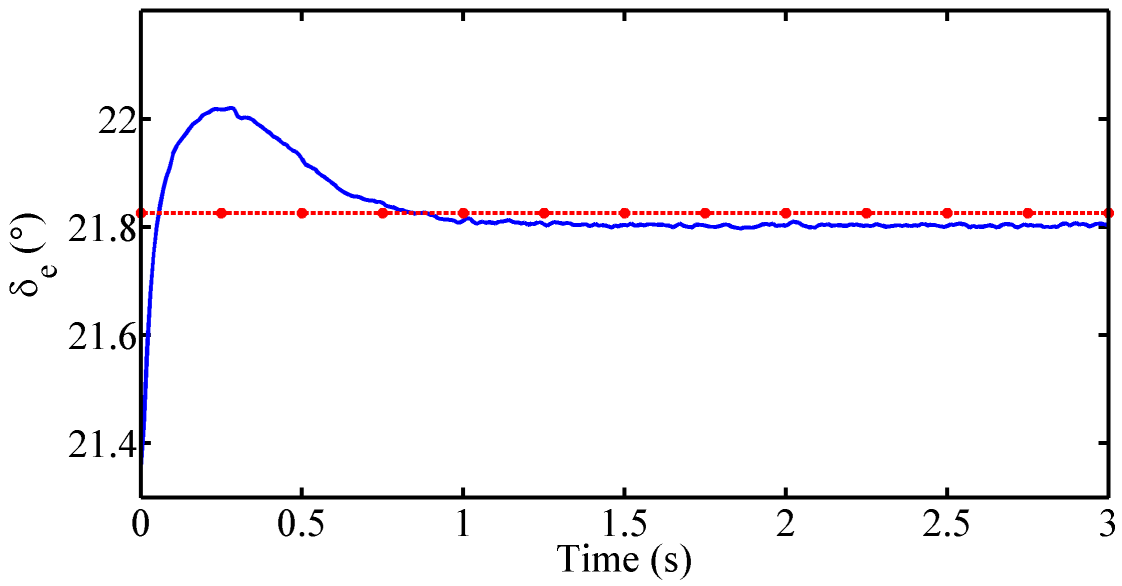

Figure 3.11: Elevator Deflection δ_e for the Tracking Controller Driving $\theta = 13°$ to $\theta_d = 7°$, Where the Dotted Line Represents $\delta_{e,trim}$

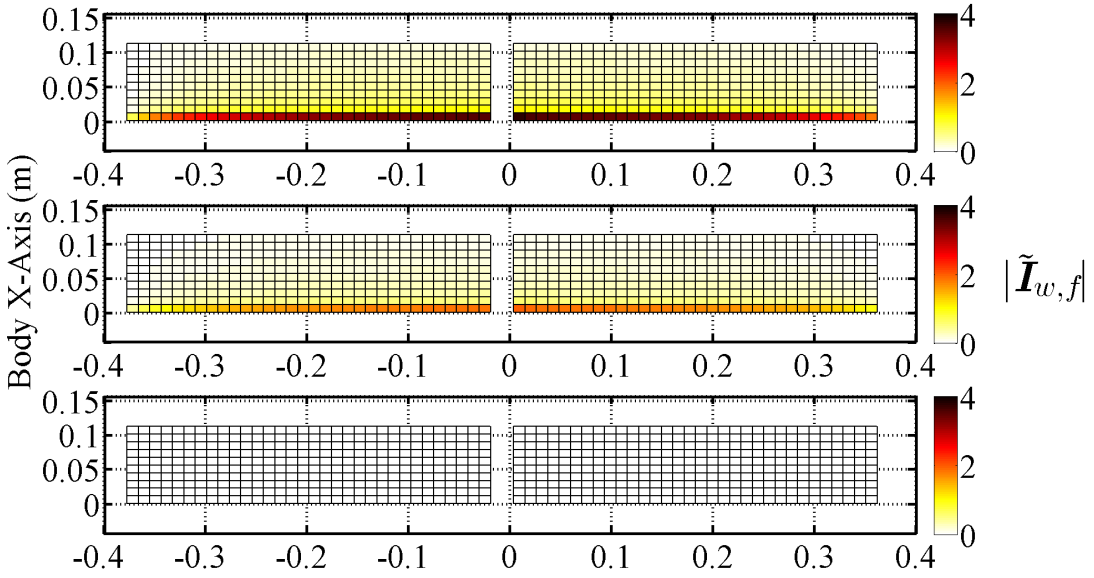

Figure 3.12: Case 1A Pressure Image Error Magnitude, $|\tilde{\boldsymbol{I}}_{w,f}|$, for $t = 0$ s (top), $t = 0.25$ s (middle), and $t = 1$ s (bottom)

Simulation Case 1B: In this simulation, a gust is simulated at $t = 0.25$ s, with a duration of 1 s. This gust is implemented by modifying the flow image measurements $\boldsymbol{I}_{wf}$ term in **Eq. (3.1.1)** as follows

$$\boldsymbol{I}_{wf}(\boldsymbol{X}(i)) = \begin{cases} \boldsymbol{I}_{wf}(\boldsymbol{X}(i)), \ x(i) < 0.4c \\ \epsilon(t)\boldsymbol{I}_{wf}(\boldsymbol{X}(i)), \ 0.4c \leq x(i) \leq 0.6c \\ \boldsymbol{I}_{wf}(\boldsymbol{X}(i)), \ x(i) > 0.6c \end{cases} \tag{3.2.19}$$

where $\boldsymbol{X}(i) = [x(i), \quad y(i), \quad z(i)]^T$ is the location of the i^{th} sensor, $\epsilon(t)$ is a uniformly distributed random variable between $1 \pm A$ where A is the maximum gust magnitude percentage, which for the simulation is set to be 33 %. The gust is assumed to have the greatest effect between $0.4c$ and $0.6c$ locations as shown in **Figure 3.13**.

The gust is applied using a cosine ramp to provide continuous application of the disturbance. The pitch angle plot for the gust applied at 0.25 seconds can be seen in **Figure 3.14** below. It can be seen that the gust causes a change of about 0.25° in the pitch angle. The system is able to resist the gust and converge to the desired condition while generating control deflections smaller than the specified maximum of ±60°.

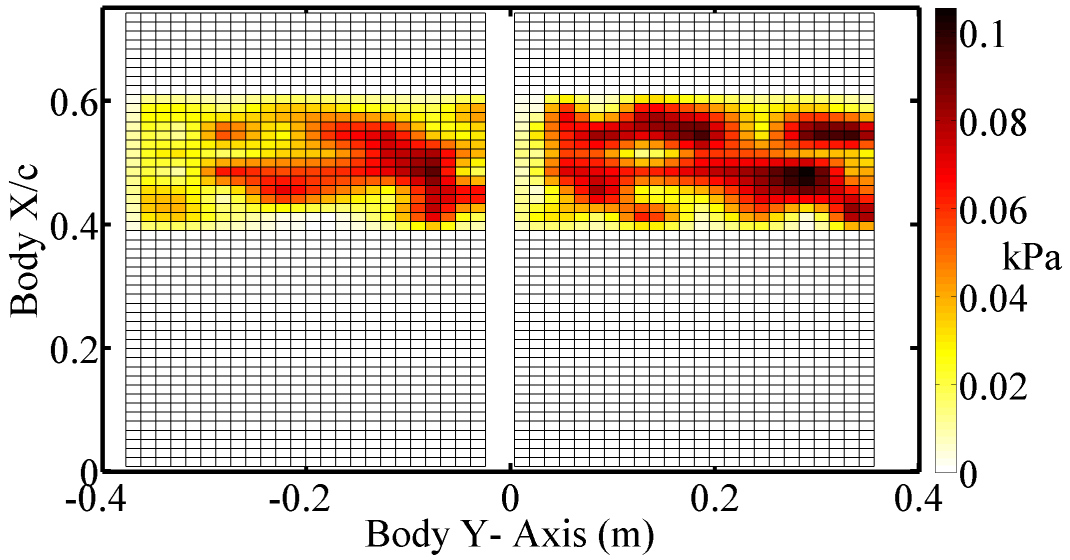

Figure 3.13: Measurement noise added between $x = 0.4c$ and $x = 0.6c$ for Case 1B at $t = 0.7s$ where sensors are not located on control surfaces between $x = 0.75c$ and $x = c$

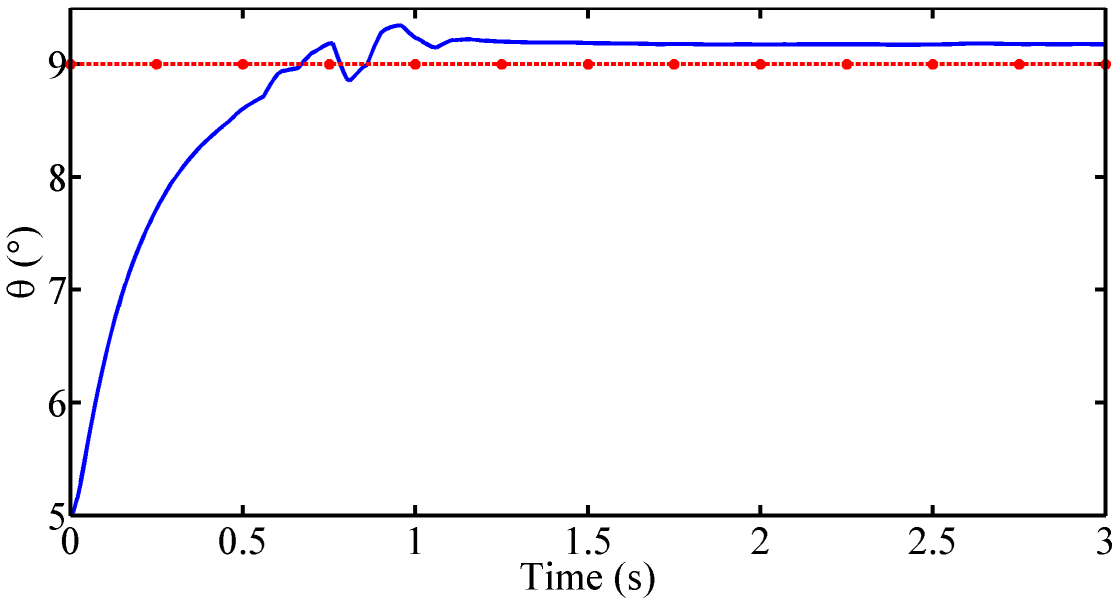

Figure 3.14: Pitch angle for the tracking controller driving $\theta = 5°$ to $\theta_d = 9°$ with $1s$ gust starting at $t = 0.25s$, where the dotted line represents θ_d

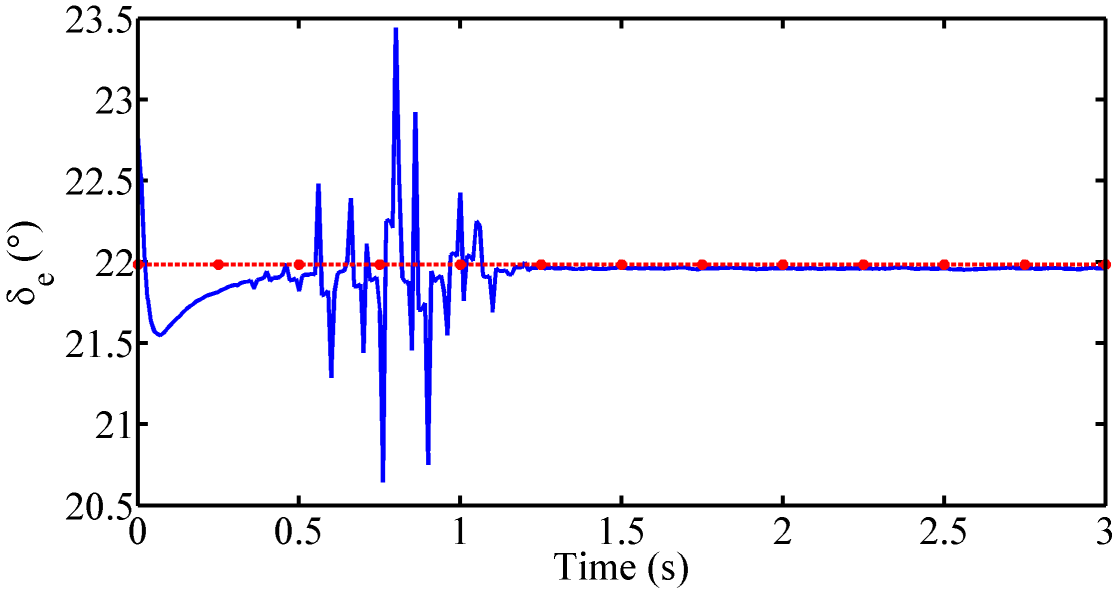

Figure 3.15: Elevator deflection δ_e for the Tracking Controller Driving $\theta = 5°$ to $\theta_d = 9°$ with $1s$ Gust Starting at $t = 0.25s$, Where the Dotted Line Represents $\delta_{e,trim}$

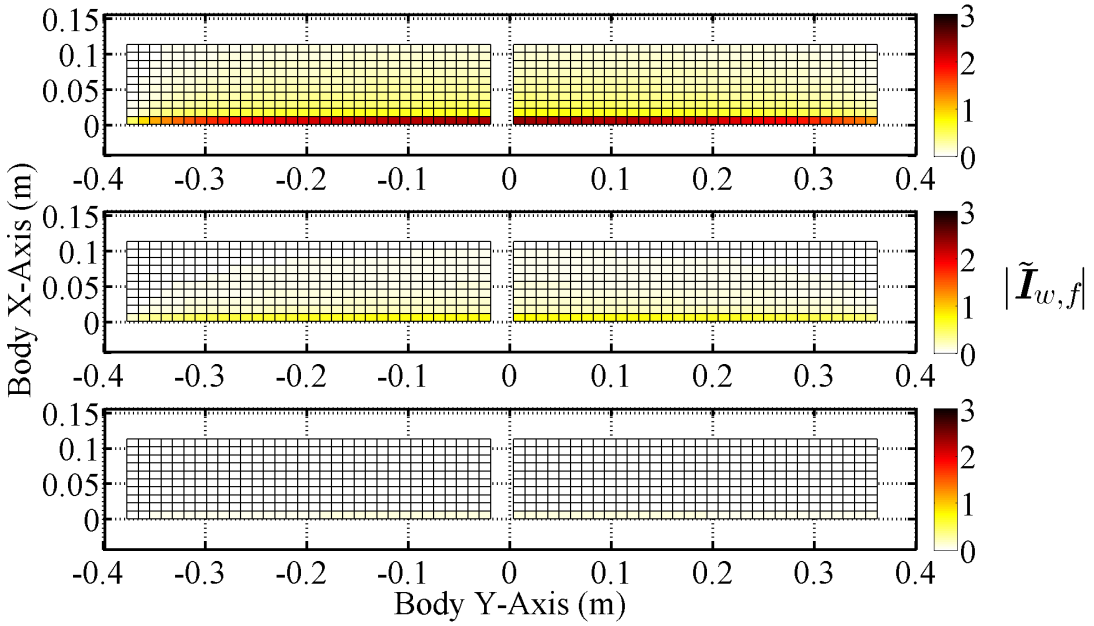

Figure 3.16: Case 1B Pressure Image Error Magnitude, $|\tilde{\boldsymbol{I}}_{w,f}|$, for $t = 0$ s (top), $t = 0.25$ s (middle), and $t = 1$ s (bottom)

3.2.5 Flow Image Pitch Controller Discussion

It can be seen that compared to the flow field based robust pitch controller presented in **Section 3.1**, that the performance of the flow image based controller removes the oscillatory control commands seen while maintaining the desired performance. The flow image controller utilizes more accurate estimates of the aerodynamic moment through the mapping function as it is utilizing the pressure over the entire surface of the wing instead of making the assumption that the pressure on the wing is uniform in the span-wise direction. Calculating the moment estimate using more sensors will inherently increase the accuracy of the aerodynamic mapping function which allows the controller to be more robust to changes in flow around the wing as they should be captured by the denser sensor network on the SUAV. The operators established for the flow image pitch controller can be utilized to easily manipulate the flow images for the development of a flow image based attitude controller as shown in the following chapter.

CHAPTER 4

FLOW IMAGE BASED ATTITUDE CONTROL

4.1 Overview of Flow Image Based Attitude Control

This chapter covers work that is currently under review with the title "Flow Field Image Based Attitude Control for Small Unmanned Aerial Vehicles". The benefits for using the flow image based attitude controllers is that it will be able to react quickly to abrupt changes in flow similar to the pressure profile based controller which was outlined in **Section 3.1** with the added benefit of reducing computation times as it will be able to directly respond to changes in the image. The error experienced when generating control commands using the flow image method is expected to be greatly reduced as the flow images will be more data rich than the current discrete sensing location based pressure controllers. The flow images will be able to represent all of the pressure or shear information on the surface of the wing using many sensors, for the upcoming work it will be assumed that the sensor density is such that each sensors area of influence is less than 1 cm^2, so for the wing simulated in **Section 3.2** the number of sensors utilized to realize the flow image will be close to 1200 sensors. It is expected that if SUAV's are able to utilize this many sensors it will be possible to emulate the biological fliers more closely to improve agile flight performance. Another

benefit to increasing the sensor density is that the overall influence of any individual sensor is greatly reduced, thus the controller will become more robust to sensor failures.

4.1.1 Problem Definition

The benefits of the utilization of the flow image based controller can be summarized as follows:

1. The flow image based controller will improve upon existing control paradigms utilized by SUAVs which use inertial sensors to generate control commands and cannot react to abrupt changes in flow around the vehicle.

2. The flow image based controller will improve upon the pressure profile based controller which has been previously presented as it will reduce computation times and complexity in the model associated with generating the invariant mapping function. The flow image based controller also will reduce the need for calibration of the sensors used by the mapping function.

3. The flow image based controller directly uses the error between the current flow image and the desired flow image to generate control commands, given the linear relationships established in **Section 3.1**, it is expected that the desired flow images could be generated quickly online during flight reducing the amount of storage required by the controller.

4. The flow image based controller allows for the sensor density to be increased while reducing computation time, this increase in sensor numbers increases the robustness of the controller to sensor faults and other individual sensor errors.

5. The flow image based controller uses real-time flow information, thus, the controller does not have to rely solely on offline obtained or predicted aerodynamic coefficients and derivatives. These online calculations increase the computational accuracy of aerodynamic forces and moments, increasing the effectiveness of the controller in all flight conditions.

6. The flow image based controller has other applications in which rich flow information can be used to increase vehicle stability, like in hypersonic vehicles or artificial fish.

These benefits show the importance of this research into developing new flow image based control paradigms for use in SUAV applications. Though physical sensors which are capable of being deployed in a way to effectively utilize the flow image based controller do not yet exist, doing this fundamental research into the controller beforehand will allow for quicker adoption once sensor technology is available.

4.2 Attitude Control using Flow Image

In this section, a nonlinear robust controller, driven by the errors between the actual and desired flow field images, is designed for the three-axis attitude motion of a SUAV, which is

governed by

$$\begin{aligned} \dot{\boldsymbol{\theta}} &= T\boldsymbol{\omega} \\ \dot{\boldsymbol{\omega}} &= -J^{-1}\tilde{\boldsymbol{\omega}}J\boldsymbol{\omega} + J^{-1}M\boldsymbol{I}_{wf} + J^{-1}M_{\delta}\boldsymbol{\delta} \end{aligned} \tag{4.2.1}$$

The Euler angles (ϕ, θ, and ψ) are included in $\boldsymbol{\theta}$, and J is the moment of inertia as

$$J = \begin{bmatrix} J_{xx} & J_{xy} & J_{xz} \\ J_{yx} & J_{yy} & J_{yz} \\ J_{zx} & J_{zy} & J_{zz} \end{bmatrix} \tag{4.2.2}$$

For a typical SUAV, J_{xy}, J_{yx}, J_{yz} and J_{zy} are zeros. $\boldsymbol{\delta} = [\delta_a, \delta_e, \delta_r]^T$ is comprised of the deflection angles of the ailerons, elevator, and rudder. $\boldsymbol{\omega} = [p, q, r]^T$ is the angular velocity, and $\tilde{\boldsymbol{\omega}}$ is the skew symmetric matrix of $\boldsymbol{\omega}$.

The external torque in the attitude motion model **Eq. (4.2.1)** comprises the aerodynamic moments experienced by the wing-fuselage and the control surface deflections, respectively. $\boldsymbol{I}_{wf}$ is the flow field image over the wing-fuselage, and $M\boldsymbol{I}_{wf}$ is the aerodynamic moment acting on the SUAV wing-fuselage. M_{δ} the control derivative matrix of the control surfaces and its uncertainty is assumed to be bounded by $M_{\delta}\hat{M}_{\delta}^{-1} = (I + D)$, in which $\hat{M}_{\delta}$ is the nominal value of the control derivative matrix and the symbol I is abused to represent an identity matrix for brevity. In **Eq. (4.2.1)**, T is the relationship between $\dot{\boldsymbol{\theta}}$ and $\boldsymbol{\omega}$ [60] based on the rotation sequence of 3-2-1 from the Earth inertial coordinate to the SUAV body coordinates as

$$T = \begin{bmatrix} 1 & sin(\phi)tan(\theta) & cos(\phi)tan(\theta) \\ 0 & cos(\phi) & -sin(\phi) \\ 0 & sin(\phi)sec(\theta) & cos(\phi)sec(\theta) \end{bmatrix} \tag{4.2.3}$$

It is further assumed that $TJ^{-1}(I+D)JT^{-1}$ is $I+E$, and each of the elements in matrix E is bounded by $0 \leq |E_{i,j}| < G_{i,j} < 1$, $i = j = 1, 2, 3$. The output of the model is the Euler angle $\boldsymbol{y} = \boldsymbol{h} = \boldsymbol{\theta}$. The right hand side of **Eq. (4.2.1)** is rewritten as $\boldsymbol{f} + B\boldsymbol{\delta}$, in which the input matrix $B \in \mathbb{R}^{6\times 3}$ is denoted as

$$B = \begin{bmatrix} 0 \\ \\ J^{-1}M_{\delta} \end{bmatrix} \tag{4.2.4}$$

Lemma 2*: If it is assumed that $|M\boldsymbol{I}_{wf} - \widehat{M\boldsymbol{I}}_{wf}| \leq F$, the difference between the actual and nominal Lie derivatives, $L^2_{\boldsymbol{f}}\boldsymbol{h}$ and $L^2_{\hat{\boldsymbol{f}}}\boldsymbol{h}$, is bounded by $A(\boldsymbol{\theta}, J)F$, in which $A(\boldsymbol{\theta}, J)$ is derived to be*

$$A(\boldsymbol{\theta}, J) = \begin{bmatrix} a_{11} & a_{12} & a_{13} \\ a_{21} & a_{22} & a_{23} \\ a_{31} & a_{32} & a_{33} \end{bmatrix} \tag{4.2.5}$$

where

$$a_{11} = \frac{J_{zz} - J_{xz}cos(\phi)}{J_{xx}J_{zz} - {J_{xz}}^2} \tag{4.2.6}$$

$$a_{12} = \frac{sin(\phi)tan(\theta)(J_{xx}J_{zz} - {J_{xz}}^2)}{J_{yy}(J_{xx}J_{zz} - {J_{xz}}^2)} \tag{4.2.7}$$

$$a_{13} = \frac{J_{xx}cos(\phi) - J_{xz}}{J_{xx}J_{zz} - {J_{xz}}^2} \tag{4.2.8}$$

$$a_{21} = \frac{J_{xz}cos(\phi)}{J_{xx}J_{zz} - {J_{xz}}^2} \tag{4.2.9}$$

$$a_{22} = \frac{cos(\phi)(J_{xx}J_{zz} - {J_{xz}}^2)}{J_{yy}(J_{xx}J_{zz} - {J_{xz}}^2)} \tag{4.2.10}$$

$$a_{23} = \frac{-J_{xx}sin(\phi)}{J_{xx}J_{zz} - {J_{xz}}^2} \tag{4.2.11}$$

$$a_{31} = \frac{-J_{xz}cos(\phi)}{(J_{xx}J_{zz} - {J_{xz}}^2)cos(\theta)} \tag{4.2.12}$$

$$a_{32} = \frac{sin(\phi)(J_{xx}J_{zz} - {J_{xz}}^2)}{cos(\theta)J_{yy}(J_{xx}J_{zz} - {J_{xz}}^2)} \tag{4.2.13}$$

and

$$a_{33} = \frac{cos(\phi)J_{xz}}{(J_{xx}J_{zz} - J_{xz}^2)cos(\theta)} \tag{4.2.14}$$

Here "L" denotes the Lie derivative, $\widehat{M\mathbf{I}}_{wf}$ is the approximately computed aerodynamic moment over the wing-fuselage surface based on the pressure and shear information measured using the finite number of microscale flow sensors and $\hat{\boldsymbol{f}}$ is the nominal value of $\boldsymbol{f}$.

Proof. Based on **Eq. (4.2.1)**

$$\boldsymbol{f} = \begin{bmatrix} T\boldsymbol{\omega} \\ J^{-1}\tilde{\boldsymbol{\omega}}J\boldsymbol{\omega} + J^{-1}M\boldsymbol{I}_{wf} \end{bmatrix} \tag{4.2.15}$$

$$\boldsymbol{y} = \boldsymbol{h} \tag{4.2.16}$$

Similarly to showing that $|M\boldsymbol{I}_{wf} - M\hat{\boldsymbol{I}}_{wf}| \leq F$, in Theorem 1, we can prove that $|L^2_{\boldsymbol{f}}\boldsymbol{h} - L^2_{\hat{\boldsymbol{f}}}\boldsymbol{h}| \leq F_2$, where "L" denotes the Lie derivative. For a typical fixed wing SUAV, $J_{xy} = J_{yz} = 0$ which makes the moment of inertia matrix J

$$J = \begin{bmatrix} J_{xx} & 0 & J_{xz} \\ 0 & J_{yy} & 0 \\ J_{xz} & 0 & J_{zz} \end{bmatrix} \tag{4.2.17}$$

Evaluating $L_{\boldsymbol{f}}\boldsymbol{h}$ it can be shown that

$$L_{\boldsymbol{f}}\boldsymbol{h} = T\boldsymbol{\omega} \tag{4.2.18}$$

The second Lie derivative $L^2_{\boldsymbol{f}}\boldsymbol{h}$ can be evaluated as follows

$$L^2_{\boldsymbol{f}}\boldsymbol{h} = \frac{\partial L_{\boldsymbol{f}}\boldsymbol{h}}{\partial \boldsymbol{x}}\boldsymbol{f} = \frac{\partial T\boldsymbol{\omega}}{\partial \boldsymbol{x}}\boldsymbol{f} \tag{4.2.19}$$

where $\dfrac{\partial T\boldsymbol{\omega}}{\partial \boldsymbol{x}}$ can be shown as

$$\frac{\partial T\boldsymbol{\omega}}{\partial \boldsymbol{x}} = \begin{bmatrix} \dfrac{\partial T\boldsymbol{\omega}}{\partial \phi} & \dfrac{\partial \boldsymbol{\omega}}{\partial \theta} & \dfrac{\partial \boldsymbol{\omega}}{\partial \psi} & \dfrac{\partial T\omega}{\partial p} & \dfrac{\partial \boldsymbol{\omega}}{\partial q} & \dfrac{\partial \boldsymbol{\omega}}{\partial r} \end{bmatrix} \tag{4.2.20}$$

where

$$\frac{\partial \boldsymbol{\omega}}{\partial \phi} = \begin{bmatrix} tan(\theta)(qcos(\phi) - rsin(\phi)), & -rcos(\phi) - qsin(\phi), & \dfrac{-rsin(\phi) + qcos(\phi)}{cos(\theta)} \end{bmatrix}^T \tag{4.2.21}$$

$$\frac{\partial \boldsymbol{\omega}}{\partial \theta} = \left[\frac{rcos(\phi) + qsin(\phi)}{cos^2(\theta)}, \quad 0, \quad \frac{tan(\theta)}{cos(\theta)}(rcos(\phi) + qsin(\phi))\right]^T \tag{4.2.22}$$

$$\frac{\partial \boldsymbol{\omega}}{\partial \psi} = \left[0, \quad 0, \quad 0\right]^T \tag{4.2.23}$$

$$\frac{\partial \boldsymbol{\omega}}{\partial p} = \left[1, \quad 0, \quad 0\right]^T \tag{4.2.24}$$

$$\frac{\partial \boldsymbol{\omega}}{\partial q} = \left[sin(\phi)tan(\theta), \quad cos(\phi), \quad \frac{sin(\phi)}{cos(\theta)}\right]^T \tag{4.2.25}$$

$$\frac{\partial \boldsymbol{\omega}}{\partial r} = \left[cos(\phi)tan(\theta), \quad -sin(\phi), \quad \frac{cos(\phi)}{cos(\theta}\right)]^T \tag{4.2.26}$$

This matrix is multiplied by $\boldsymbol{f}$ it creates a very complex result, however when evaluating $L^2_{\boldsymbol{f}}\boldsymbol{h} - L^2_{\hat{\boldsymbol{f}}}\boldsymbol{h}$ many of the terms cancel leaving a 3×3 matrix which is a function of $\boldsymbol{x}$ which is multiplied by the aerodynamic moment difference $\boldsymbol{m} - \hat{\boldsymbol{m}}$ to find the difference as follows.

$$M\tilde{\boldsymbol{I}}_{p,wf} - L^2_{\hat{\boldsymbol{f}}}\boldsymbol{h} = A(\boldsymbol{\theta}, J)\left\{\boldsymbol{m} - \hat{\boldsymbol{m}}\right\} \tag{4.2.27}$$

Where $A(\boldsymbol{\theta}, J)$ is defined as,

$$A(\boldsymbol{\theta}, J) = \begin{bmatrix} a_{11} & a_{12} & a_{13} \\ a_{21} & a_{22} & a_{23} \\ a_{31} & a_{32} & a_{33} \end{bmatrix} \tag{4.2.28}$$

Since all of the terms in the A matrix are bounded as they depend on constants and measured values, and that $|M\boldsymbol{I} - M\hat{\boldsymbol{I}}|$ is bounded by F. It can be concluded that $|L_{\boldsymbol{f}}^2\boldsymbol{h} - L_{\hat{\boldsymbol{f}}}^2\boldsymbol{h}|$ is also bounded by some value F_2 which is equal to $A(\theta, J)F$. □

Theorem 2: *With the bounded input matrix uncertainty $G_{i,j} < 1\,, i = j = 1, 2, 3$, and the state function uncertainty defined in Lemma 2, the closed-loop, three-axis attitude motion of a SUAV defined in* ***Eq. (4.2.1)*** *is asymptotically stable, driven by the following controller*

$$\boldsymbol{\delta} = \left[TJ^{-1}\hat{M}_{\delta}\right]^{-1}\left[\ddot{\boldsymbol{\theta}}_d - L_{\hat{\boldsymbol{f}}}^2\boldsymbol{h} - \boldsymbol{k}_1 \cdot M\tilde{\boldsymbol{I}}_{wf} - \boldsymbol{k}_2 \cdot M\dot{\tilde{\boldsymbol{I}}}_{wf}\right] \tag{4.2.29}$$

Here "$\cdot$" represents the point-wise multiplication. The control gains $\boldsymbol{k}_i, i = 1, 2$ are selected in the proof. The difference between the actual and desired flow field images on the wing-fuselage of a SUAV is $\tilde{\boldsymbol{I}}_{wf}$.

Proof. The error between the desired and actual Euler angle is $\tilde{\boldsymbol{\theta}} = \boldsymbol{\theta} - \boldsymbol{\theta}_d$. The Lyapunov function is chosen to be $V = 0.5\boldsymbol{s}^{\,T}\boldsymbol{s} \geq 0$, in which $\boldsymbol{s} = \tilde{\boldsymbol{\theta}} + \dot{\tilde{\boldsymbol{\theta}}} + \boldsymbol{\lambda} \cdot M\tilde{\boldsymbol{I}}_{wf}$. Thus the derivative of $\boldsymbol{s}$ is

$$
\begin{aligned}
\dot{\boldsymbol{s}} &= \dot{\tilde{\boldsymbol{\theta}}} + \ddot{\tilde{\boldsymbol{\theta}}} + \boldsymbol{\lambda} \cdot M\dot{\tilde{\boldsymbol{I}}}_{wf} \\
&= \dot{\boldsymbol{\theta}} - \dot{\boldsymbol{\theta}}_d + \ddot{\boldsymbol{\theta}} - \ddot{\boldsymbol{\theta}}_d + \boldsymbol{\lambda} \cdot M\dot{\tilde{\boldsymbol{I}}}_{wf} \\
&= L_{\boldsymbol{f}}^2\ \boldsymbol{h} + (L_{\boldsymbol{B}} L_{\boldsymbol{f}} \boldsymbol{h})\boldsymbol{\delta} - \ddot{\boldsymbol{\theta}}_d + \boldsymbol{\lambda} \cdot M\dot{\tilde{\boldsymbol{I}}}_{wf} + \dot{\boldsymbol{\theta}} - \dot{\boldsymbol{\theta}}_d
\end{aligned}
\tag{4.2.30}
$$

$L_{\boldsymbol{B}} L_{\boldsymbol{f}} \boldsymbol{h}$ can be derived to be

$$
L_{\boldsymbol{B}} L_{\boldsymbol{f}}\ \boldsymbol{h} = TJ^{-1} M_{\delta} \tag{4.2.31}
$$

Substituting the controller in **Eq. (4.2.29)** into **Eq. (4.2.30)**

$$
\begin{aligned}
\dot{\boldsymbol{s}} = L_{\boldsymbol{f}}^2 \boldsymbol{h} + (I + E) \left[\ddot{\boldsymbol{\theta}}_d - L_{\hat{\boldsymbol{f}}}^2 \boldsymbol{h} - \boldsymbol{k}_1 \cdot M\tilde{\boldsymbol{I}}_{wf} - \boldsymbol{k}_2 \cdot M\dot{\tilde{\boldsymbol{I}}}_{wf} \right] \\
- \ddot{\boldsymbol{\theta}}_d + \boldsymbol{\lambda} \cdot M\dot{\tilde{\boldsymbol{I}}}_{wf} + \dot{\boldsymbol{\theta}} - \dot{\boldsymbol{\theta}}_d
\end{aligned}
\tag{4.2.32}
$$

which can be simplified as

$$
\begin{aligned}
\dot{\boldsymbol{s}} = \ & L_{\boldsymbol{f}}^2 \boldsymbol{h} - L_{\hat{\boldsymbol{f}}}^2 \boldsymbol{h} - \boldsymbol{k}_1 \cdot M\tilde{\boldsymbol{I}}_{wf} - \boldsymbol{k}_2 \cdot M\dot{\tilde{\boldsymbol{I}}}_{wf} \\
& + E \left[\ddot{\boldsymbol{\theta}}_d - L_{\hat{\boldsymbol{f}}}^2 \boldsymbol{h} - \boldsymbol{k}_1 \cdot M\tilde{\boldsymbol{I}}_{wf} - \boldsymbol{k}_2 \cdot M\dot{\tilde{\boldsymbol{I}}}_{wf} \right] \\
& + \boldsymbol{\lambda} \cdot M\dot{\tilde{\boldsymbol{I}}}_{wf} + \dot{\boldsymbol{\theta}} - \dot{\boldsymbol{\theta}}_d
\end{aligned}
\tag{4.2.33}
$$

Grouping the terms $-\boldsymbol{k}_1 \cdot M\tilde{\boldsymbol{I}}_{wf} - \boldsymbol{k}_2 \cdot M\dot{\tilde{\boldsymbol{I}}}_{wf}$ as $\boldsymbol{d}_1$, $\dot{\boldsymbol{s}}$ can be rewritten as

$$
\dot{\boldsymbol{s}} = L_{\boldsymbol{f}}^2 \boldsymbol{h} - L_{\hat{\boldsymbol{f}}}^2 \boldsymbol{h} + \boldsymbol{d_1} + \boldsymbol{\lambda} \cdot M\dot{\tilde{\boldsymbol{I}}}_{wf} + E \left[\ddot{\boldsymbol{\theta}}_d - L_{\hat{\boldsymbol{f}}}^2 \boldsymbol{h} + \boldsymbol{d_1} \right] + \dot{\boldsymbol{\theta}} - \dot{\boldsymbol{\theta}}_d \tag{4.2.34}
$$

Therefore, $\dot{V}$ can be written as

$$
\begin{aligned}
\dot{V} &= \boldsymbol{s}^T \dot{\boldsymbol{s}} \\
&= \boldsymbol{s}^T \left\{ L_{\boldsymbol{f}}^2 \boldsymbol{h} - L_{\hat{\boldsymbol{f}}}^2 \boldsymbol{h} + \boldsymbol{d}_1 + \boldsymbol{\lambda} \cdot M\dot{\tilde{\boldsymbol{I}}}_{wf} E \left[\ddot{\boldsymbol{\theta}}_d - L_{\hat{\boldsymbol{f}}}^2 \boldsymbol{h} + \boldsymbol{d}_1 \right] + \dot{\boldsymbol{\theta}} - \dot{\boldsymbol{\theta}}_d \right\}
\end{aligned}
\tag{4.2.35}
$$

Considering the uncertainty bounds and the sign of $\boldsymbol{s}$, **Eq. (4.2.35)** can be derived as

$$\begin{aligned}\dot{V} \leq \boldsymbol{s}^T \Big\{ & sgn(\boldsymbol{s}) \cdot |A(\boldsymbol{\theta}, J)F| + \boldsymbol{\lambda} \cdot M\dot{\tilde{\boldsymbol{I}}}_{wf} + \boldsymbol{d}_1 \\ & + sgn(\boldsymbol{s}) \cdot G|\boldsymbol{d}_1| + sgn(\boldsymbol{s}) \cdot G|\ddot{\boldsymbol{\theta}}_d - L^2_{\hat{\boldsymbol{f}}}\boldsymbol{h}| + \dot{\boldsymbol{\theta}} - \dot{\boldsymbol{\theta}}_d \Big\}\end{aligned} \tag{4.2.36}$$

It is worth noting that

$$sgn(\boldsymbol{s}) = \begin{Bmatrix} sgn(s_1) \\ sgn(s_2) \\ sgn(s_3) \end{Bmatrix} \tag{4.2.37}$$

$\boldsymbol{d}_1$ can be found to make **Eq. (4.2.36)** equal $-\boldsymbol{s}^T(\boldsymbol{\eta} \cdot \boldsymbol{s})$, for $\boldsymbol{\eta} > 0$, then $\dot{V} \leq 0$. In this case,

$$\begin{aligned}\boldsymbol{d}_1 + sgn(\boldsymbol{s}) \cdot G|\boldsymbol{d_1}| = & - sgn(\boldsymbol{s}) \cdot |A(\boldsymbol{\theta}, J)F| + \dot{\boldsymbol{\theta}}_{\boldsymbol{d}} - \dot{\boldsymbol{\theta}} - \boldsymbol{\lambda} \cdot M\dot{\tilde{\boldsymbol{I}}}_{wf} \\ & - sgn(\boldsymbol{s}) \cdot G|\ddot{\boldsymbol{\theta}}_{\boldsymbol{d}} - L^2_{\hat{\boldsymbol{f}}}\ \boldsymbol{h}| - \boldsymbol{\eta} \cdot \boldsymbol{s}\end{aligned} \tag{4.2.38}$$

If the right hand side of **Eq. (4.2.38)** is set to be a new variable, $\boldsymbol{f}_4$, **Eq. (4.2.38)** can be simplified as

$$\boldsymbol{f}_4 = \boldsymbol{d}_1 + sgn(\boldsymbol{s}) \cdot G|\boldsymbol{d_1}| \tag{4.2.39}$$

Case 1: $s_i > 0$ for $i = 1, 2, 3$

Assuming $d_{1,i}$ has the same sign as $f_{4,i}$ for $i = 1, 2, 3$. **Eq. (4.2.39)** can be rewritten as

$$\boldsymbol{f}_4 = \boldsymbol{d}_1 + sgn(\boldsymbol{f}_4) \cdot G\boldsymbol{d_1} \tag{4.2.40}$$

Solving for $\boldsymbol{d}_1$ yields

$$\boldsymbol{d}_1 = [I + sgn(\boldsymbol{f}_4) \cdot G]^{-1} \boldsymbol{f}_4 \tag{4.2.41}$$

Since the magnitude of each entry in $sgn(\boldsymbol{f}_4)\cdot G$ is between 0 and 1, it will result in a solution for $\boldsymbol{d_1}$ with the same sign as $\boldsymbol{f_4}$ based on the Frobenius-Perron theorem [59]. **Case 2:** $s_i < 0$ for $i = 1, 2, 3$

Assuming $d_{1,i}$ has the same sign as $f_{4,i}$ for $i = 1, 2, 3$. Using this, **Eq. (4.2.39)** can then be rewritten as

$$\boldsymbol{f}_4 = \boldsymbol{d}_1 - sgn(\boldsymbol{f}_4) \cdot G\boldsymbol{d_1} \tag{4.2.42}$$

Solving for $\boldsymbol{d}_1$ yields

$$\boldsymbol{d}_1 = [I - sgn(\boldsymbol{f}_4) \cdot G]^{-1} \boldsymbol{f}_4 \tag{4.2.43}$$

Follow the same procedure in Case 1, **Eq. (4.2.43)** will result in a solution for $\boldsymbol{d_1}$ with the same sign as $\boldsymbol{f_4}$. **Case 3:** $s_i > 0$, $s_j < 0$, $i = 1, 2, 3$, $j = 1, 2, 3$, $i \neq j$

In this case, G changed to G^*, in which its i^{th} row will reverse its sign if $s_i < 0$. **Eq. (4.2.39)** can be rewritten as

$$\boldsymbol{f}_4 = \boldsymbol{d}_1 + sgn(\boldsymbol{f}_4) \cdot G^*\boldsymbol{d_1} \tag{4.2.44}$$

Solving for $\boldsymbol{d}_1$ yields

$$\boldsymbol{d}_1 = [I + sgn(\boldsymbol{f}_4) \cdot G^*]^{-1} \boldsymbol{f}_4 \tag{4.2.45}$$

Eq. (4.2.45) will also result in a solution for $\boldsymbol{d}_1$ with the same sign as $\boldsymbol{f}_4$. For all three cases, there are solutions for $\boldsymbol{d}_1$ so that $\dot{V} < 0$. **Case 4:** $s_i = 0$

When s_i is equal to zero, $d_{1,i}$ reduces to

$$d_{1,i} = \left(\dot{\theta} - \boldsymbol{\lambda} \cdot M\dot{\tilde{\boldsymbol{I}}}_{wf} - \ddot{\theta}_d + \dot{\theta}_d\right)_i \tag{4.2.46}$$

Summarizing the above cases, with a proper tuning of $\boldsymbol{\lambda}$ and $\boldsymbol{\eta}$, $\boldsymbol{d}_1$ can be calculated such that $\dot{V} \leq 0$. For the case when $\boldsymbol{s} = 0$, $\dot{V} = 0$, $\ddot{V}$ can be found as

$$\begin{aligned}\ddot{V} &= \boldsymbol{s}^T\ddot{\boldsymbol{s}} + \dot{\boldsymbol{s}}^T\dot{\boldsymbol{s}} = \dot{\boldsymbol{s}}^T\dot{\boldsymbol{s}} \\ &= \left\{L_{\boldsymbol{f}}^2\ \boldsymbol{h} - L_{\hat{\boldsymbol{f}}}^2\ \boldsymbol{h} + \boldsymbol{d}_1 - \dot{\boldsymbol{\theta}}_d + \dot{\boldsymbol{\theta}} + G\left[\ddot{\boldsymbol{\theta}}_d - L_{\hat{\boldsymbol{f}}}^2\ \boldsymbol{h} + \boldsymbol{d}_1\right]\boldsymbol{\lambda}\cdot M\dot{\tilde{\boldsymbol{I}}}_{wf}\right\}^T \\ &\quad \left\{L_{\boldsymbol{f}}^2\ \boldsymbol{h} - L_{\hat{\boldsymbol{f}}}^2\ \boldsymbol{h} + \boldsymbol{d}_1 + G\left[\ddot{\boldsymbol{\theta}}_d - L_{\hat{\boldsymbol{f}}}^2\ \boldsymbol{h} + \boldsymbol{d}_1\right] + \boldsymbol{\lambda}\cdot M\dot{\tilde{\boldsymbol{I}}}_{wf} - \dot{\boldsymbol{\theta}}_d + \dot{\boldsymbol{\theta}}\right\}\end{aligned} \tag{4.2.47}$$

From Lemma 2, we know that $L_{\boldsymbol{f}}^2\ \boldsymbol{h} - L_{\hat{\boldsymbol{f}}}^2\ \boldsymbol{h}$ is bounded by $|A(\boldsymbol{\theta}, J)|F$. The values $\boldsymbol{\lambda}\cdot M\dot{\tilde{\boldsymbol{I}}}_{wf}$ and $\boldsymbol{d_1}$ are measured so they are bounded. The values of $\dot{\boldsymbol{\theta}}_d$ and $\ddot{\boldsymbol{\theta}}_d$ are the desired values and they are bounded. The $L_{\hat{\boldsymbol{f}}}^2\ \boldsymbol{h}$ term is calculated based on the moment of inertia J and trigonometric functions involving measured values so it is bounded. It can be shown that each term in **Eq. (4.2.47)** is bounded, thus $\ddot{V} = \dot{\boldsymbol{s}}^T\dot{\boldsymbol{s}}$ is also bounded. As before, using Barbalat's lemma [59], since $V \geq 0$ is lower bounded, $\dot{V} \leq 0$, and $\ddot{V}$ is bounded, the closed-loop system is asymptotically stable. □

Remark 1: There are four switching cases depending on the sign of s. To avoid the chattering phenomena, two approaches can be used. The first is to apply a low pass filter on the calculated control commands. The second is to use the boundary layer control function to replace the sign function in **Eq. (4.2.39)**. The boundary layer function ζ can be found as

$$\zeta_i = \begin{cases} sgn(s_i/\gamma_i) & , |s_i/\gamma_i| > 1 \\ s_i/\gamma_i & , |s_i/\gamma_i| \leq 1 \end{cases} \tag{4.2.48}$$

where $i = 1, 2, 3$ and γ_i is the boundary layer function parameter.

4.3 Simulation of Flow Image Controller

4.3.1 Flow Image Attitude Controller Simulation Parameters

AVL is used to generate the pressure field image on the surface of a simulated SUAV. The simulated SUAV geometry is similar to that found in [45] with the exception that the sensor number per wing was increased to 100 sensors per wing, i.e. 200 sensors for the total aircraft wing. The sensor distribution consists of 20 sensors spaced equally in the chord-wise direction along 5 cosine spaced rows in the span-wise direction, resulting in 100 sensors per wing. The wing has a span of 0.762 m, chord length of 0.154 m and a dihedral angle of 5°. The SUAV has three control surfaces (elevator, rudder and aileron), and the control derivatives for these control surfaces M_δ is selected to be

$$M_\delta = \begin{bmatrix} 0.6098 & 0 & 0.5035 \\ 0 & 0.0038 & 0 \\ 0.0653 & 0 & 0.0540 \end{bmatrix} Nm/\circ \tag{4.3.1}$$

It is worth noting that AVL does not directly output the upper and lower surface pressures but instead outputs a differential pressure coefficient, ΔC_P, which can be converted to a differential pressure as $\Delta P = 0.5\rho_\infty V_\infty^2 \Delta C_P$, where ρ_∞ is the air density and V_∞ is the free stream velocity. In the attitude simulation, it is assumed that the wind velocity is always facing the same direction and has a magnitude of 10 m/s. The shear force on the surface of the wing is not directly available in the AVL simulation environment. However,

in this study, we assume that the fluid flow around the wing is Newtonian and the shear force on the wing is uniformly distributed. With these assumptions, the shear stress can be calculated as $\tau = 0.5 C_f \rho_\infty {V_\infty}^2$ [57]. The skin friction coefficient, C_f, can be calculated as $C_f = 0.664/\sqrt{Re}$. The Reynolds number, Re, is calculated as $Re = (\rho_\infty V_\infty d)/\mu$, in which μ is the dynamic viscosity and d is the airfoil thickness at the location where the shear stress is being calculated. With the pressure and shear information, the flow image similar to **Figure 3.9** can be generated. The flow image encodes sensor locations and the pressure and shear information. Using this information, a linear interpolation method is used to generate uniformly spaced pressure and shear measurements in the chord-wise direction. Then the same interpolation is conducted in the span-wise direction using the same node spacing to establish a uniform grid of pressure and shear measurements on the entire surface of the wing.

Remark 2: It is computationally expensive to generate pressure and shear stress field images in simulation software, such as AVL. Furthermore, the pressure and shear information generated by the software may not accurately represent the real flow conditions near the SUAV surface. Nevertheless, the simulated flow field is only used to demonstrate the capability of the proposed flow field image based control methodology in this study. In real scenarios, flow field images are directly measured using flow sensors embedded in SUAVs, which can be done in real time and will be accurate. For example,the working frequency of one commercially available pressure sensor is up to 157Hz [61]. We expect in the near future,

when sensor design and manufacturing technologies get significantly improved, we will be able to integrate enough sensors on a SUAV to conduct flight experiments.

4.3.2 Flow Image Controller Simulation Objectives

Two simulation cases are also conducted to validate the proposed three-axis attitude control. In Case A (output tracking), the SUAV is commanded to track a new trimmed flight condition. In Case B (gust wind rejection), the SUAV is stabilized when facing a simulated gust.

4.3.3 Flow Image Controller Simulation Parameters

For both simulations, the uncertainty bounds G and F are assumed to be

$$G = \begin{bmatrix} 2.0 \times 10^{-4} & 0 & 2.0 \times 10^{-4} \\ 0 & 2 \times 10^{-4} & 0 \\ 2.0 \times 10^{-4} & 0 & 2.0 \times 10^{-4} \end{bmatrix}$$

and

$$F = \begin{bmatrix} 5.0 \times 10^{-5}, & 5.0 \times 10^{-5}, & 5.0 \times 10^{-5} \end{bmatrix}^T Nm$$

These uncertainty bounds are roughly 10% of their respective nominal values. The control parameters $\boldsymbol{\lambda}$, $\boldsymbol{\eta}$, and $\boldsymbol{\gamma}$ after tuning are selected to be

$$\boldsymbol{\lambda} = \begin{bmatrix} 10, & 125 & 85 \end{bmatrix}^T$$

$$\boldsymbol{\eta} = \begin{bmatrix} 15.5, & 14.5, & 12.5 \end{bmatrix}^T$$

$$\boldsymbol{\gamma} = \begin{bmatrix} 3, & 1, & 2 \end{bmatrix}^T$$

4.3.4 Flow Image Controller Simulation Results

Simulation Case A-1:

The initial Euler angles are $\boldsymbol{\theta} = [-7^\circ, 12^\circ, -5^\circ]$ and the desired Euler angles are $\boldsymbol{\theta}_d = [0^\circ, 6^\circ, 0^\circ]$. The closed-loop attitude history is shown in **Figure 4.1** and the control deflections are shown in **Figure 4.2** . It can be observed that the rise time is less than 1 second, the steady state errors are within 5%, and the control surface deflections do not exceed a maximum of 60°. Also within the bounded uncertainty, there is no chattering. In **Figure 4.3**, the actual and desired flow images can be seen for different time steps, it can be seen that the actual flow image converges to the desired flow image at the end of the simulation time.

Simulation Case 2A-2:

The initial Euler angles are $\boldsymbol{\theta} = [3^\circ, 5^\circ, 2^\circ]$ and the desired Euler angles are $\boldsymbol{\theta}_d = [-1^\circ, 8^\circ, -3^\circ]$. The controller is shown to be capable of driving the Euler angles to nonzero roll and yaw

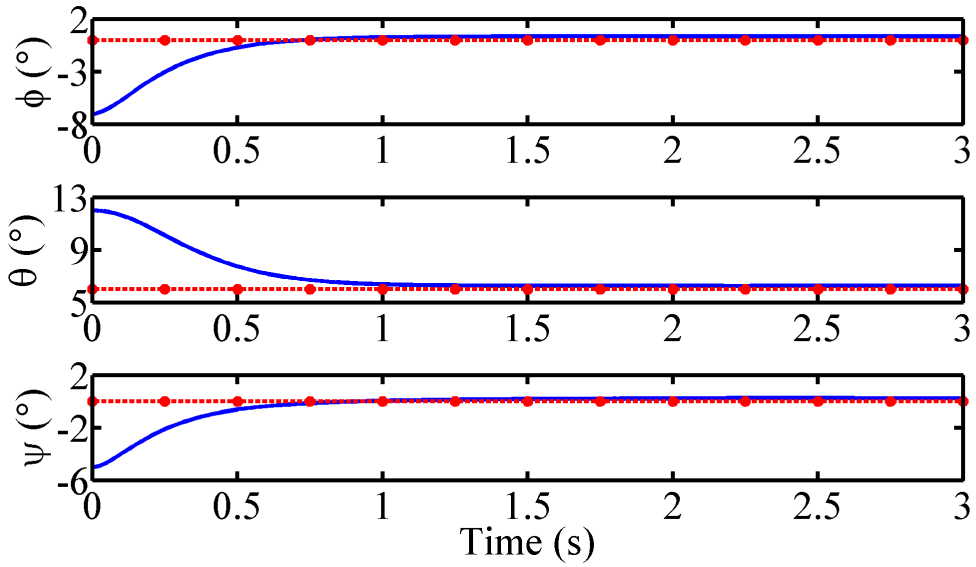

Figure 4.1: Euler Angles for the Tracking Controller to Drive $\boldsymbol{\theta} = [-7°, 12°, -5°]$ to $\boldsymbol{\theta}_d = [0°, 6°, 0°]$, Where the Dotted Lines Represent $\boldsymbol{\theta}_d$

angles. Similar results as Case 2A-1 can be seen here, the settling time is less than 1 second, and the steady state errors are less than 5% in **Figure 4.4**. The control surface deflections are shown in **Figure 4.5**. The flow images for 0 s, 1 s and 3 s are shown in **Figure 4.6**, and demonstrate that the controller is capable of driving the flow image to the desired image with non-zero roll and yaw angles.

Simulation Case 2B:

For this simulation, a gust is simulated at $t = 1.5$ s, after the Euler angles have stabilized from the output tracking controller. This gust is generated similarly to Simulation Case 1B with a gust duration of 1 second. The Euler angle plot for the gust applied at 1.5 seconds can be seen in **Figure 4.7** below. It can be seen that the gust causes a change of 0.12° , 0.25°

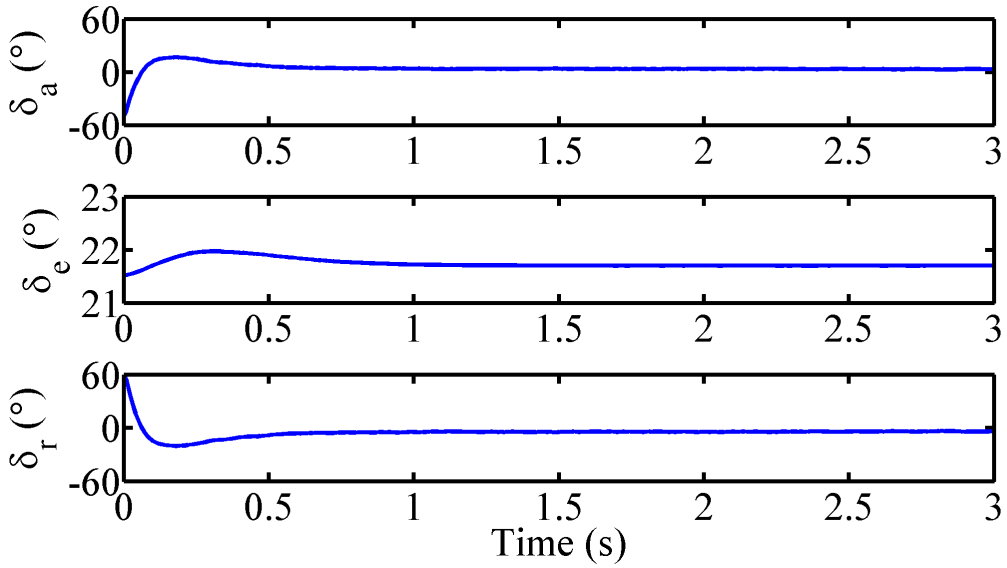

Figure 4.2: Control Surface Deflections for the Tracking Controller to Drive $\boldsymbol{\theta} = [-7°, 12°, -5°]$ to $\boldsymbol{\theta}_d = [0°, 6°, 0°]$

and 0.25° in the roll pitch and yaw directions, respectively. The system is able to resist the gust and maintain a flight pattern close to the converged condition while generating control deflections smaller than the specified maximum of 60°.

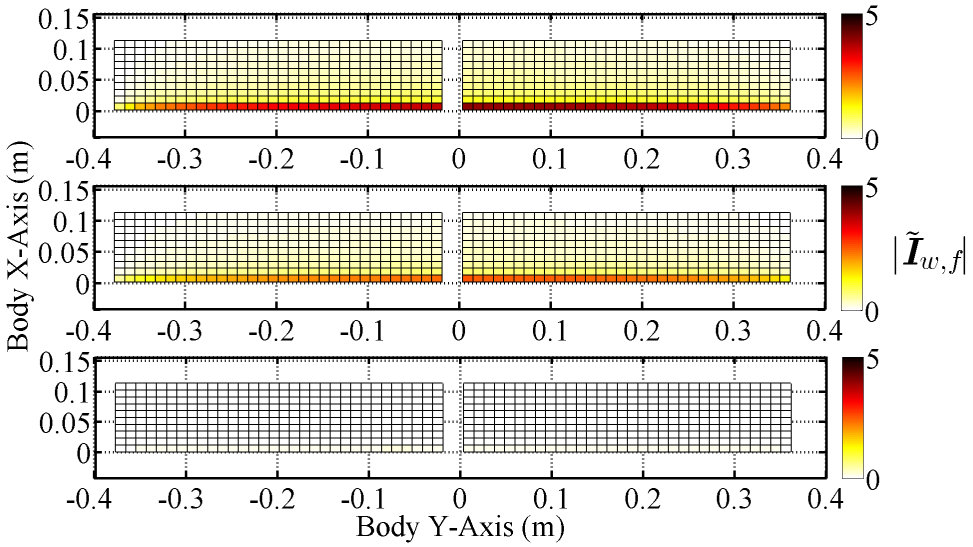

Figure 4.3: Case A-1 Pressure image error magnitude, $|\tilde{\boldsymbol{I}}_{w,f}|$, for $t = 0$ s (top), $t = 0.25$ s (middle), and $t = 1$ s (bottom)

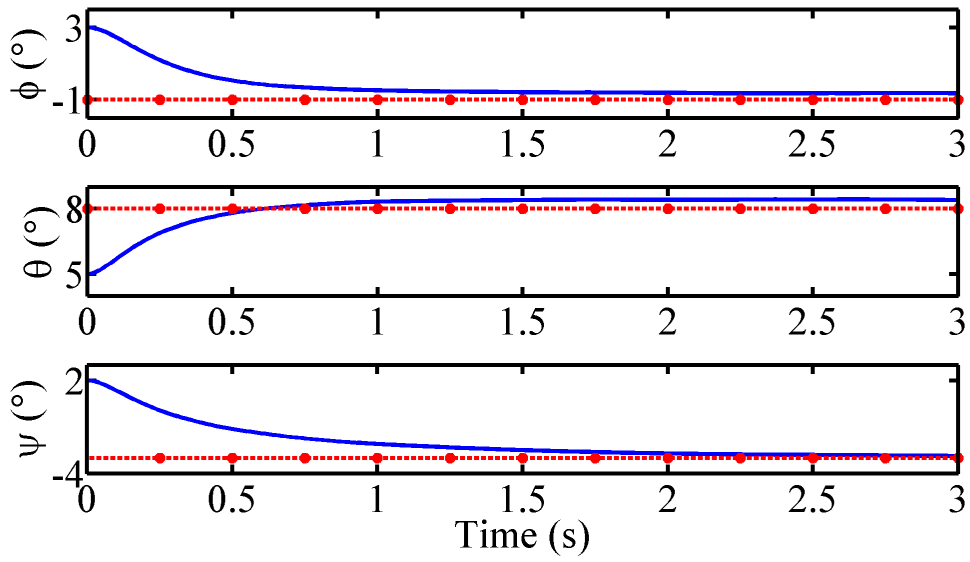

Figure 4.4: Euler angle for output tracking from $\boldsymbol{\theta} = [3°, 5°, 2°]$ to $\boldsymbol{\theta}_d = [-1°, 8°, -3°]$ where dotted lines represent $\boldsymbol{\theta}_d$

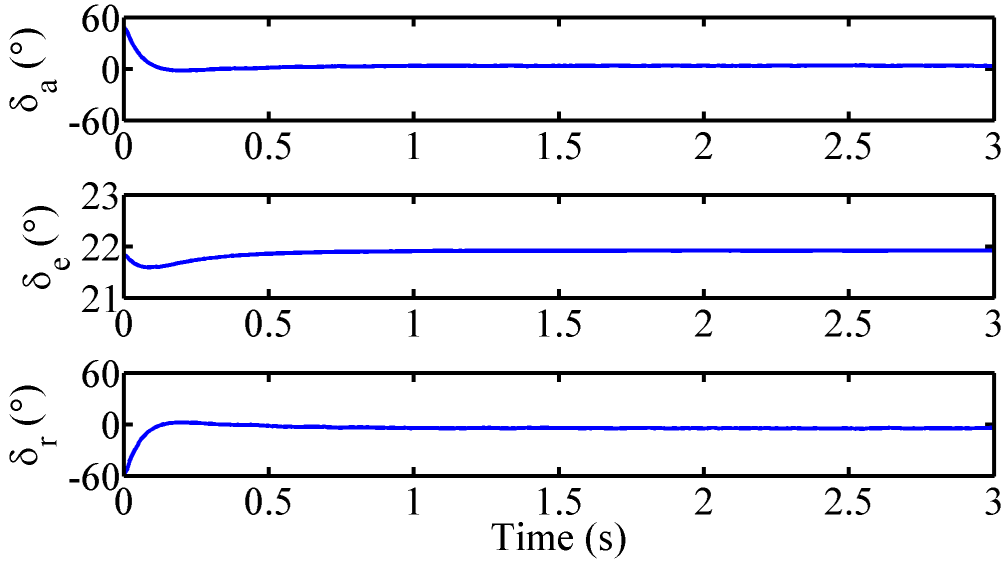

Figure 4.5: Control surface deflections for output tracking from $\boldsymbol{\theta} = [3°, 5°, 2°]$ to $\boldsymbol{\theta}_d = [-1°, 8°, -3°]$

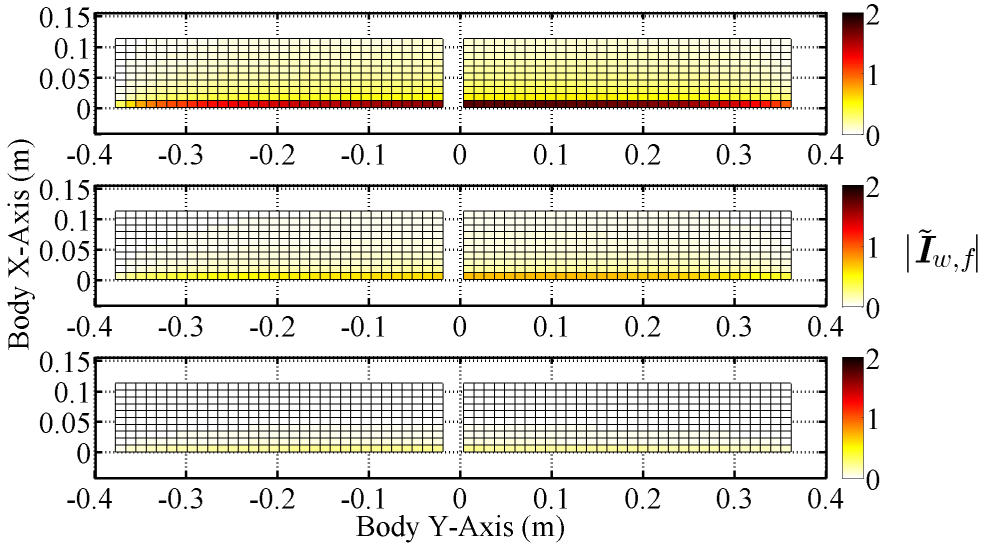

Figure 4.6: Case A-2 Pressure image error magnitude, $|\tilde{\boldsymbol{I}}_{w,f}|$, for $t = 0$ s (top), $t = 0.25$ s (middle), and $t = 1$ s (bottom)

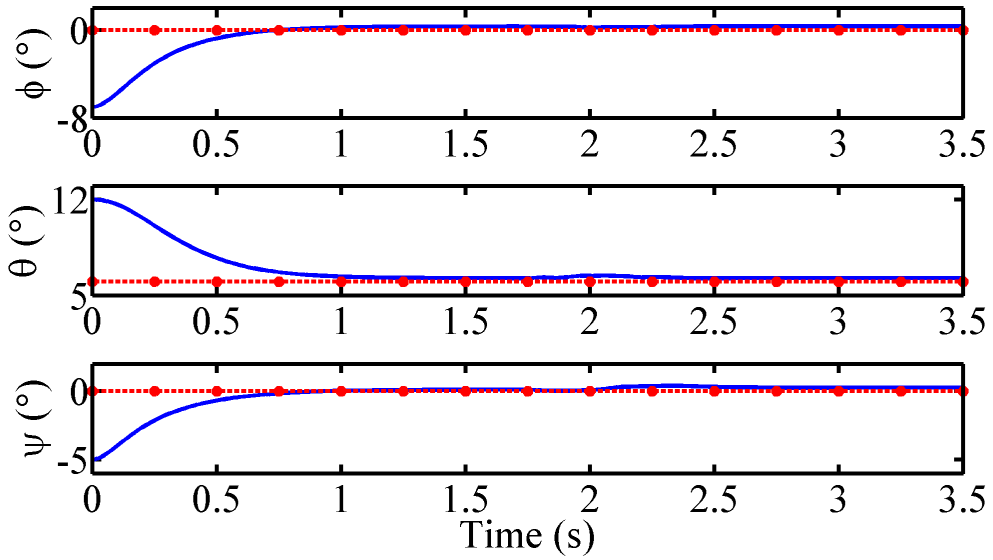

Figure 4.7: Euler Angles in Gust Rejection Simulation

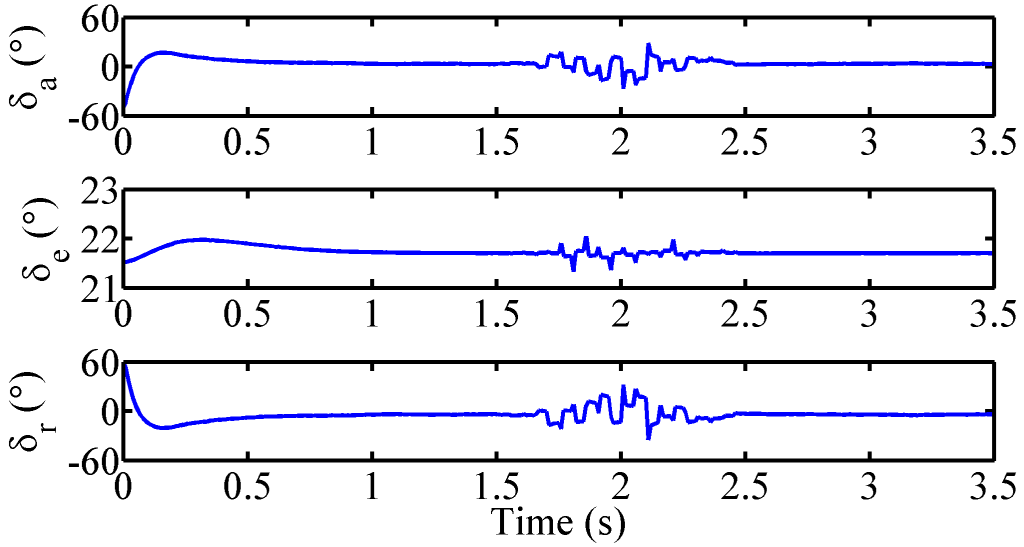

Figure 4.8: Control Surface Deflections in Gust Rejection Simulation

4.4 Flow Image Attitude Controller Discussion

It can be seen from these simulation cases that the controller is effective at accomplishing output tracking goals while being robust to uncertainty and gusts experienced during flight. The tracking controller is capable of reaching the desired Euler angles with no gusts as shown in **Figure 4.1** and **Figure 4.4**, with minimal overshoot and steady state offset. The rise time for each axis is below 1 second which is desirable for implementation in real time aircraft systems. During the tracking maneuver the commanded control deflections shown in **Figure 4.2** and **Figure 4.5** do not exceed the physical limit of the control surfaces of $\pm 60^{\circ}$, while having minimal oscillations due to the inclusion of the boundary layer functions. The pressure image time history shown in **Figure 4.3** and **Figure 4.6** demonstrate that the controller is accomplishing its objective of driving the image error to zero and not just matching the desired aerodynamic moment through a different pressure image.

The same performance can be seen when a gust is introduced during the tracking controller. A long duration gust of 1 seconds is applied and the control command sufficiently reacts to the gust while maintaining steady flight as seen in **Figure 4.7**. The control commands generated during the gust shown in **Figure 4.8** do not exceed the maximum of $\pm 60^{\circ}$ and are able to quickly respond to the gust based on the gust profile.

CHAPTER 5

CONCLUSIONS AND FUTURE WORK

5.1 Conclusions

This dissertation has presented the development of tools and methods to make a pressure image based robust controller for SUAV systems. The foundation of this work is built upon the ability to estimate the aerodynamic forces and moment acting on the SUAVs through the use of the aerodynamic mapping function. Previously the aerodynamic mapping function has depended on the use of many sensors to accurately estimate the aerodynamic moment, however using the methods presented in **Chapter 2**, the aerodynamic mapping function errors can be significantly reduced and make sparse sensor networks available for use. The calibration method was validated using both simulation and wind tunnel tests and showed that the calibration method was capable of working from data acquired on-line while reducing the error for all flight conditions within the linear flight envelope.

A flow field based pitch controller was first developed in **Chapter 3** to validate the use of a "pressure field" with the mapping function to calculate control commands based only on surface pressure measurements. This controller depended on establishing the relationships between the angle of attack, sideslip angle, free stream velocity and the aerodynamic moment

found via the mapping function. The relationships found show a strong linear trend with angle of attack and sideslip angle and the free stream velocity increases the slope of the linear relationship. The established relationships show that a flow field based controller is possible as the moments calculated for given flight conditions should follow the patterns represented. The flow field pattern controller was effective at accomplishing output tracking a disturbance rejection control objectives using only a single strip of sensors along the center of the wing and assuming uniformity in the span-wise direction to generate the flow field over the entire wing. Though this method showed promising accuracy in the output tracking simulations the oscillatory motion in the disturbance rejection simulation is not desired for practical aircraft.

A method utilizing measurements over the entire wing surface are presented in the second half of **Chapter 3** in which a pressure image is created utilizing pressure and shear measurements on the wing which are then interpolated to create a uniform grid of "pixels" that make up the image. The simulations for the pitch only flow image based controller show that the response of the controller still converges very quickly for the output tracking simulation but loses the undesirable chattering experienced in the flow field controller. The flow image based pitch controller also benefits from having a better response to gusts most likely because the gust information is distributed across the entire wing and the controller has more information to estimate the actual aerodynamic forces acting on the wings of the aircraft. The success of this controller leads to the expansion to a full 3D attitude controller developed in **Chapter 4**.

The 3D pressure image based attitude controller presented expands the controller developed for the pitch only motion to successfully control the Euler angles of the SUAV.

5.2 Future Work

Developing the new image operators for the robust flow image based controller which are capable of directly taking the image difference between the current and desired flow images are needed. It is anticipated that the use of established machine learning algorithms or neural networks will be useful in the development of these new operators. There is nothing in the literature that is similar to these types of operators, but it is anticipated that they will require some parameter identification techniques to be used prior to implementation. This parameter identification may be able to be done using traditional optimal estimation techniques, however, if necessary deep learning algorithms may need to be used to identify the parameters.

It is expected that with operators which are capable of utilizing flow images directly the computation speed will increase and will allow for the control commands to react faster to sudden changes in the flow around the wing. As sensor technologies improve to allow for denser skin sensor configurations it will be necessary to utilize these quicker operators for advanced control maneuvers.

LIST OF REFERENCES

[1] T. F. Villa, F. Gonzalez, B. Miljievic, Z. D. Ristovski, and L. Morawska, "An overview of small unmanned aerial vehicles for air quality measurements: Present applications and future prospectives," *Sensors (Basel, Switzerland)*, vol. 16, no. 7, pp. 849–857, 2016.

[2] H. Shen, Y. Xu, and B. Dickinson, "Micro air vehicle's attitude control using real-time pressure and shear information," *Journal of Aircraft*, vol. 51, no. 2, pp. 661–671, 2014.

[3] D. Phillips, C. Ray, B. Hagen, W. Su, J. Baur, and G. Reich, "Detection of flow separation and stagnation points using artificial hair sensors," *Smart Materials and Structures*, vol. 24, no. 11, p. 115026, 2015.

[4] R. Zhu, P. Liu, X. Liu, F. Zhang, and Z. Zhou, "A low-cost flexible hot-film sensor system for flow sensing and its application to aircraft," in *2010 American Control Conference*, (Sorrento, Italy), January 25-29 2009 IEEE 22nd International Conference on Micro Electro Mechanical Systems.

[5] H. Shen, Y. Xu, and C. Remeikas, "Hardware design and validation of pitching control for micro air vehicles using only pressure information," in *2013 American Control Conference*, (Washington, DC), pp. 5568–5573, June 17-19 2013.

[6] H. Shen, Y. Xu, and B. Dickinson, "Fault tolerant attitude control for small unmanned aircraft systems equipped with an airflow sensor array," *Bioinspiration and Biomimetics*, vol. 9, no. 4, p. 046015, 2014.

[7] D. Marshall, R. Barnhart, S. Hottman, E. Shappee, and M. Most, *Introduction to Unmanned Aircraft Systems*. CRC Press, 2012.

[8] C. Galinski and R. Zbikowski, "Some problems of micro air vehicles development," *Bulletin of the Polish Academy of Sciences, Technical Sciences*, vol. 55, no. 1, pp. 91–98, 2007.

[9] D. Otero, N. Gagliardo, D. Dalli, and C. Otero, "Preliminary suav component evaluation for inspecting transportation infrastructure systems," in *2016 Annual IEEE Systems Conference*, (Orlando, FL), pp. 1–4, Apr 18-21 2016.

[10] R. Ehsani, S. Sankaran, J. M. Maja, and J. C. Neto, "Affordable multi-rotor remote sensing platform for applications in precision horticulture," in *11th International Conference Precision Agriculture*, (Indianapolis, IN), July 15-18 2012.

[11] G. Pierce Jones, L. Pearlstine, and H. H.F. Percival, "An assessment of small unmanned aerial vehicles for wildlife research," *Wildlife Society Bulletin (1973-2006)*, vol. 34, no. 3, pp. 750–758, 2006.

[12] P. Iscold, G. Pereira, and L. Torres, "Development of a hand-launched small uav for ground reconnaissance," *IEEE Transactions on Aerospace and Electronic Systems*, vol. 46, pp. 335–348, Jan 2010.

[13] L. Petricca, P. Ohlckers, and C. Grinde, "Micro- and nano-air vehicles: state of the art," *International Journal of Aerospace Engineering*, vol. 2011, p. 17, 2011.

[14] W. Davis, B. Kosicki, D. Boroson, and D. Kostishack, "Micro air vehicles for optical surveillance," *Lincoln Laboratory Journal*, vol. 9, no. 2, pp. 197–214, 1996.

[15] D. Pines and F. Bohorquez, "Challenges facing future micro air vehicle development," *Journal of Aircraft*, vol. 43, no. 2, pp. 290–305, 2006.

[16] I. Golightly and D. Jones, "Visual control of an unmanned aerial vehicle for power line inspection," in *12th International Conference on Advanced Robotics*, (Seattle, WA), July 18-20 2005.

[17] S. Shkarayev, P. Ifju, J. Kellogg, and T. Mueller, *Introduction to the Design of Fixed-wing Micro Air Vehicles Including Three Case Studies*. AIAA, 2007.

[18] R. Zbikowski, "Sensor-rich feedback control: a new paradigm for flight control inspiration by insect agility," *IEEE Information and Measurement Magazine*, vol. 7, no. 3, pp. 19–26, 2004.

[19] A. Mangalam and M. Brenner, "Fly-by-feel sensing and control: Aeroservoelasticity," in *AIAA Atmospheric Flight Mechanics Conference*, (Atlanta, GA), Jun 16-20 2014.

[20] J. Keshavan and J. Humbert, "Mav stability augmentation using weighted outputs from distributed hair sensor arrays," in *2010 American Control Conference*, (Baltimore, MD), pp. 4445–4450, June 30- July 2 2010.

[21] I. Samy, I. Postlethwaite, and D. Gu, "Subsonic tests of a flush air data sensing system applied to a fixed-wing micro air vehicle-samy," *Journal of Intelligent and Robotic Systems*, vol. 54, no. 1-3, pp. 275–295, 2009.

[22] J. Hubbard and D. Pullen, "Pressure sensor system." U.S. Patent, August 2008. 7,415,876.

[23] M. Hays, J. Morton, B. Dickinson, U. Chakravarty, and W. Oates, "Aerodynamic control of micro air vehicle wings using electroactive membranes," *Journal of Intelligent Material Systems and Structures*, vol. 24, no. 7, pp. 862–878, 2013.

[24] A. Mohamed, S. Watkins, R. Clothier, M. Abdulrahim, K. Massey, and R. Sabatini, "Fixed-wing mav attitude stability in atmospheric turbulence - part 2: Investigating biologically-inspired sensors," *Progress in Aerospace Sciences*, vol. 71, pp. 1–13, 2014.

[25] M. Maschmann, G. Ehlert, B. Dickinson, D. Phillips, C. Ray, G. Reich, and J. Baur, "Bioinspired carbon nanotube fuzzy fiber hair sensor for air-flow detection," *Advanced Materials*, vol. 26, no. 20, pp. 3230–3234, 2014.

[26] T. Xu, C. Park, G. N., J. Kang, and J. Hubbard, "Carbon nanocomposite-based contact mode interdigitated center of pressure sensor," in *Proc. SPIE 7646, Nanosensors, Biosensors, and Info-Tech Sensors and Systems 2010*, 2010.

[27] B. B. Mohr and D. L. Fitzpatrick, "Micro air vehicle navigation system," *IEEE Aerospace and Electronic Systems Magazine*, vol. 23, no. 4, pp. 19–24, 2008.

[28] M. Achtelik, M. Achtelik, S. Weiss, and R. Siegwart, "Onboard imu and monocular vision based control for mavs in unknown in- and outdoor environments," in *2011 IEEE International Conference on Robotics and Automation*, (Shanghai, China), pp. 3056–3063, May 9-13 2011.

[29] S. M. Kanowitz, "Design and implementation of a gps-based navigation system for micro air vehicles," Master's thesis, University of Florida, 2002.

[30] T. Webb, R. Prazenica, A. Kurdila, and R. Lind, "Vision-based state estimation for autonomous micro air vehicles," *Journal of Guidance, Control, and Dynamics*, vol. 30, no. 3, pp. 816–826, 2007.

[31] T. Kanade, O. Amidi, and Q. Ke, "Real-time and 3d vision for autonomous small and micro air vehicles," in *2004 43rd IEEE Conference on Decision and Control*, vol. 2, (Atlantis, Paradise Island, Bahamas), pp. 1655–1662, Dec 14-17 2004.

[32] Z. Wang, "Insect flight: from newton's law to neurons," *Annual Review of Condensed Matter Physics*, vol. 7, no. 1, pp. 281–300, 2016.

[33] N. Gans, W. Dixon, R. Lind, and A. Kurdila, "A hardware in the loop simulation platform for vision-based control of unmanned air vehicles," *Mechatronics*, vol. 19, no. 7, pp. 1043 – 1056, 2009.

[34] J. S. Humbert and A. M. Hyslop, "Bioinspired visuomotor convergence," *IEEE Transactions on Robotics*, vol. 26, pp. 121–130, Feb 2010.

[35] R. E. Brown and M. R. Fedde, "Airflow sensors in the avian wing," *Journal of Experimental Biology*, vol. 179, no. 1, pp. 13–30, 1993.

[36] J. Usherwood, T. Hedrick, and A. Biewener, "The aerodynamics of avian take-off from direct pressure measurements in canada geese (branta canadensis)," *Journal of Experimental Biology*, vol. 206, no. 22, pp. 4051–4056, 2003.

[37] J. Usherwood, T. Hedrick, C. McGowan, and A. Biewener, "Dynamic pressure maps for wings and tails of pigeons in slow, flapping flight, and their energetic implications," *Journal of Experimental Biology*, vol. 208, no. 2, pp. 355–369, 2005.

[38] H. Takahashi, Y. Aoyama, K. Ohsawa, H. Tanaka, E. Iwase, K. Matsumoto, and I. Shimoyama, "Differential pressure measurement using a free-flying insect-like ornithopter with an mems sensor," *Bioinspiration and Biomimetics*, vol. 5, no. 3, p. 036005, 2010.

[39] S. Sterbing-D'Angelo, M. Chadha, C. Chiu, B. Falk, W. Xian, J. Barcelo, J. Zook, and C. Moss, "Bat wing sensors support flight control," *Proceedings of the National Academy of Sciences*, vol. 108, no. 27, pp. 11291–11296, 2011.

[40] B. Dickinson, S. McClain, and L. Case, "The dynamic response of quasi-steady hair-like structures in oscillatory boundary layer flows," in *6th AIAA Flow Control Conference*, (New Orleans, LA), Jun 25-28 2012.

[41] S. Callegari, M. Zagnoni, A. Golfarelli, M. Tartagni, A. Talamelli, P. Proli, and A. Rossetti, "Experiments on aircraft flight parameter detection by on-skin sensors," *Sensors and Actuators A: Physical*, vol. 130-131, pp. 155 – 165, 2006.

[42] R. Que and R. Zhu, "Aircraft aerodynamic parameter detection using micro hot-film flow sensor array and bp neural network identification," *Sensors*, vol. 12, no. 8, pp. 10920–10929, 2012.

[43] Y. Guo, Y. Li, Z. Guo, K. Kim, F. Chang, and S. Wang, "Bio-inspired stretchable absolute pressure sensor network," *Sensors*, vol. 16, no. 1, 2016.

[44] H. Shen, Y. Xu, and C. Remeikas, "Pitch control of a micro air vehicle with micropressure sensors," *Journal of Aircraft*, vol. 50, no. 1, pp. 239–248, 2013.

[45] K. Thompson, Y. Xu, A. Mark, and B. Dickinson, "Fixed wing micro aerial vehicle pitching control based on flow field patterns," in *AIAA Guidance, Navigation, and Control Conference*, (Grapevine, TX), Jan 9-13 2017.

[46] S. M. Mangalam, "Real-time extraction of hydrodynamic flow characteristics using surface signatures," *IEEE Journal of Oceanic Engineering*, vol. 29, no. 3, pp. 622–630, 2004.

[47] B. Dickinson, J. Singler, and B. Batten, "The detection of unsteady flow separation with bioinspired hair cell sensors," in *26th AIAA Aerodynamic Measurement Technology and Ground Testing Conference*, (Seattle, WA), Jun 23-26 2008.

[48] K. Thompson, Y. Xu, and B. Dickinson, "Aerodynamic moment model calibration from distributed pressure arrays," *Journal of Aircraft*, vol. 54, no. 2, pp. 716–723, 2016.

[49] K. Thapa Magar, G. Reich, C. Kondash, K. Slinker, P. A.M., J. Baur, and B. Smyers, "Aerodynamic parameters from distributed heterogeneous cnt hair sensors with a feedforward neural network," *Bioinspiration and Biomimetics*, vol. 11, no. 6, p. 066006, 2016.

[50] R. Hoseinnezhad, A. Bab-Hadiashar, and P. Harding, "Calibration of resolver sensors in electromechanical braking systems, a modified recursive weighted least-squares approach," *IEEE Transactions on Industrial Electronics*, vol. 54, no. 2, pp. 1052–1060, 2007.

[51] S. Hwang and D. Williams, "A constrained total least squares approach for sensor position calibration and direction finding," in *IEEE National Radar Conference*, (Atlanta, GA), pp. 155–159, March 29-31 1994.

[52] D. Simon, *Optimal State Estimation - Kalman, H_∞, and Nonlinear Approaches*. Wiley, 2006.

[53] J. Vogel and A. Kelkar, "Aircraft control augmentation and health monitoring using flush air data system feedback," in *26th AIAA Applied Aerodynamics Conference*, (Honolulu, Hawaii), pp. AIAA–2008–7505, August 18-21 2008.

[54] B. Dickinson, J. Singler, and B. Batten, "Mathematical modeling and simulation of biologically inspired hair receptor arrays in laminar unsteady flow separation," *Journal of Fluids and Structures*, vol. 29, pp. 1–17, 2012.

[55] N. Guerreiro and J. Hubbard, "Pressure port placement for lift distribution measurement on a model aircraft with optimized trailing-edge flaps," in *26th AIAA Applied Aerodynamics Conference*, (Honolulu, Hawaii), pp. AIAA–2008–7518, August 18-21 2008.

[56] M. Drela and H. Youngren, *AVL Primer*. Massachusetts Institute of Technology, 2017.

[57] J. Anderson, *Fundamentals of Aerodynamics*. McGraw-Hill Education, 2010.

[58] T. Yechout, *Introduction to Flight Mechanics*. American Institute of Aeronautics and Astronautics, 2003.

[59] J. Slotine and W. Li, *Applied nonlinear control*. Prentice Hall, 1990.

[60] R. Stengel, *Flight Dynamics*. Princeton University Press, 2004.

[61] Bosch Sensortec, *BMP 280 Digital Pressure Sensor*, 1.14 ed., May 2015.